

Titre: Femtosecond Laser Nanoparticle-Mediated Gene Therapy for
Title: Corneal Endothelial Treatment in Animal Models

Auteur: Jennyfer Zapata Farfan
Author:

Date: 2024

Type: Mémoire ou thèse / Dissertation or Thesis

Référence: Zapata Farfan, J. (2024). Femtosecond Laser Nanoparticle-Mediated Gene
Citation: Therapy for Corneal Endothelial Treatment in Animal Models [Thèse de doctorat,
Polytechnique Montréal]. PolyPublie. <https://publications.polymtl.ca/61249/>

 **Document en libre accès dans PolyPublie**
Open Access document in PolyPublie

URL de PolyPublie: <https://publications.polymtl.ca/61249/>
PolyPublie URL:

**Directeurs de
recherche:** Michel Meunier, Isabelle Brunette, & Gabriel Ascanio
Advisors:

Programme: Génie biomédical
Program:

POLYTECHNIQUE MONTRÉAL

affiliée à l'Université de Montréal

**Femtosecond Laser Nanoparticle-Mediated Gene Therapy for Corneal
Endothelial Treatment in Animal Models**

JENNYFER ZAPATA FARFAN

Institut de génie biomédical

Thèse présentée en vue de l'obtention du diplôme de *Philosophiæ Doctor*

Génie biomédical

Novembre 2024

POLYTECHNIQUE MONTRÉAL

affiliée à l'Université de Montréal

Cette thèse intitulée :

**Femtosecond Laser Nanoparticle-Mediated Gene Therapy for Corneal
Endothelial Treatment in Animal Models**

présentée par **Jennyfer ZAPATA FARFAN**

en vue de l'obtention du diplôme de *Philosophiæ Doctor*
a été dûment acceptée par le jury d'examen constitué de :

Frédéric LESAGE, président

Michel MEUNIER, membre et directeur de recherche

Isabelle BRUNETTE, membre et codirectrice de recherche

Gabriel ASCANIO, membre et codirecteur de recherche

Stephan REUTER, membre

Jesus GARDUÑO MEJÍA, membre

Solange LANDREVILLE, membre externe

DEDICATION

*To Silvia, Alberto,
Isra and Jon. . .*

ACKNOWLEDGMENTS

Along this journey, I had the opportunity to work with many incredible people, but none of this would have been possible without the constant support of Michel. I sincerely thank you for every insightful conversation and the immense support you've provided throughout these doctorate years. It has been an incredible experience being part of your lab, and I could not have asked for a better director: *I will survive* can now be changed for *we have survived!*

In this unique case where I have had the privilege of working with more than one supervisor, I would also like to express my gratitude to Gabriel Ascanio, Isabelle Brunette, and Jesús Garduño for their expertise and support. Your contributions and help during the various phases of my professional career have been invaluable. I am deeply grateful for the time you spent with me at UNAM and UdeM preparing either documents or those enriching conferences that have greatly enhanced my studies.

Thank you Gabriel and Michel for your support, it has truly been double the fun.

To Sergiy, for your endless ideas and new projects each day. Thank you for sharing your clever perspective and for lending me your electronics toolkit!!

To Yves Drolet, the best technician, merci pour partager tes idées et tes anecdotes, toujours très très particulières et spéciales. Your technical advice and stories have been a constant source of learning.

To my colleagues from LP²L and friends from Poly and the student associations I belong to, thank you for the countless discussions and exchanges, whether around the optical table or sometimes around a table with some beers. In the end, the result was the same: great memories and shared knowledge that I will always cherish. I can't possibly list all the amazing people I've met and now consider friends and family in this adoptive city, but you know who you are. Love you all!

Cécile, a special thank you for your help and support both in and out of the lab. Being part of our many side projects has been an incredible experience, and like you said, we definitely need days of 48 hours to fit it all in! Leo, from unofficial sources, the best member of Spectra Phys., thanks for those "focused" discussions and your support during this whole time.

To my friends in Montreal and Mexico, with special mention to Cécile, Gus, Alice, Pierric, Julz, Charlie, Diane, Karla, Layi, Élodie, Cristina y Jorge, your support has definitively helped me to go through difficult moments far from hometown. Your presence, messages and phone calls often gave me the strength I needed when times were tough. Los quiero mucho.

Finally, I want to extend my deepest appreciation to my family, Silvia, Isra, Jon, Kary, Yes, Fer, Vale y Andy Especially because being far away is not easy, but with your support, everything impossible becomes achievable in unimaginable ways. Thank you for your patience and the example of strength you give me every day. Especially to you, Mom, thank you for being my best friend, accomplice, and advisor; I will never have enough time in life to thank you and repay you for everything you've done for me. I am very grateful to life for having the blessing of having you with me in this stage. Alberto, the little dot is still way up there, I love you all!

*"All truths are easy to understand once they are discovered;
the point is to discover them."*

-Galileo Galilei

RÉSUMÉ

La motivation de cette recherche réside dans le nombre élevé de personnes affectées par les maladies endothéliales cornéennes. Plus de 2,2 milliards de personnes souffrent de troubles de la vision, et pour au moins 1 milliard d'entre elles, ces troubles auraient pu être évités ou restent non pris en charge. Les maladies endothéliales cornéennes affectent près de 250 millions de personnes dans le monde. Parmi toutes les affections endothéliales, la dystrophie cornéenne endothéliale de Fuchs (FEDC) se distingue comme étant la plus répandue et constitue la principale cause de transplantations cornéennes à l'échelle mondiale.

Pour répondre aux limites associées à la transplantation, notre proposition introduit une approche de thérapie génique utilisant un laser femtoseconde (fs) cliniquement approuvé et des nanoparticules d'or (AuNPs) pour délivrer des gènes dans les cellules endothéliales cornéennes (CECs).

L'hypothèse principale est qu'en utilisant un laser femtoseconde fortement focalisé (actuellement utilisé à des fins ophtalmiques) pour irradier les CECs dont la membrane sera décorée avec des AuNPs (matériau biocompatible), des pores transitoires (régis par la présence des AuNPs) peuvent être ouverts dans la membrane cellulaire avec une grande précision, facilitant ainsi la livraison de molécules exogènes comme l'ARN messenger qui permet de réaliser la thérapie génique.

Dans le cadre de ce travail, des expériences *in vitro* et *ex vivo* ont été réalisées pour atteindre quatre sous-objectifs:

- (i) **établir une preuve de concept en utilisant des cellules oculaires *in vitro* pour une application ultérieure chez les souris;**
- (ii) **développer un protocole plus sécuritaire pour l'injection intracaméculaire chez les modèles murins afin d'améliorer la délivrance des AuNPs dans la chambre antérieure de l'oeil;**
- (iii) **obtenir une transfection significative d'ARNm dans le modèle murin avec une haute viabilité cellulaire *ex vivo*;**
- (iv) **développer une technique adaptable à différentes espèces animales pour garantir une application future sécuritaire pour les cornées humaines.**

Le chapitre 1 offre une vue d'ensemble introductive du sujet, tandis que le chapitre 2 explore en profondeur une revue de la littérature abordant différents sujets pour ce projet

multidisciplinaire, allant d'une brève description de l'anatomie de la cornée aux techniques femtosecondes appliquées en thérapie génique. Le chapitre 3 se concentre sur le test de la technique proposée en utilisant des cellules oculaires *in vitro*, basé sur l'hypothèse énoncée.

Après avoir établi la preuve de concept avec divers fluorophores, des expériences *ex vivo* ont été réalisées. Comme expliqué au chapitre 4 (article 1), un protocole raffiné pour les injections intracamérales a été appliqué efficacement au modèle murin. Cette approche a minimisé les dommages cornéens et maximisé la délivrance des NPs à la couche cornéenne ciblée.

Les injections comprenaient une solution de AuNPs colloïdales fonctionnalisées combinée à des molécules exogènes, qui ne fluorescent que lorsqu'elles sont internalisées par les cellules cibles. L'impact des matériaux et les dimensions des aiguilles, ainsi la géométrie de leurs pointes ont été étudiés. Des microaiguilles commerciales ont été usinées au laser pour améliorer leur pénétration dans la chambre antérieure.

Après avoir affiné avec succès la technique d'injection intracamérale, le protocole développé a été appliqué dans le chapitre 5, qui explore les deuxième et troisième objectifs principaux de ce travail. Ce chapitre détaille l'optoporation et la transfection des CECs *ex vivo* dans des modèles de souris et de lapin (article 2). Un laser femtoseconde a été utilisé pour étudier les paramètres d'irradiation pour l'optoporation et la transfection des CECs. Deux types de modèles animaux ont été choisis pour une étude complémentaire : les yeux de lapin, sélectionnés pour leur similitude de taille avec les yeux humains et la robustesse de leurs cellules, et les yeux de souris.

La principale différence entre les CECs humaines et de lapin est que les CECs de lapin peuvent se répliquer, ce qui les rend idéales pour évaluer rapidement la viabilité des CECs. Après avoir démontré la preuve de concept en utilisant des cornées de lapin, des tests de transfection avec des molécules plus grandes comme l'ARNm ont été réalisés avec succès sur des cornées murines. Les résultats de cette étude conduisent à des injections intracamérales plus sécuritaires, réussies, avec des dommages cornéens et des saignements négligeables.

L'irradiation transcornéenne *ex vivo* utilisant la technique proposée a conduit à une optoporation réussie avec une haute spécificité et une efficacité élevée de 49 ± 7 % (moyenne \pm DS). Ce succès est attribué à la combinaison d'une faible fluence (valeur optimale : 100 mJ/cm^2 à $80 \text{ }\mu\text{m/s}$ comme vitesse de balayage) et à l'utilisation de AuNPs (88 ± 11 NPs/cellule, moyenne \pm DS). La procédure a minimisé les effets secondaires sur la cornée, permettant un traitement hautement localisé avec une viabilité cellulaire dépassant les 80 %.

L'implémentation de cette technique novatrice assistée par laser femtoseconde et NPs ouvre de nouvelles possibilités pour la thérapie génique et médicamenteuse dans le tissu endothélial

cornéen. Cette méthode offre un traitement moins invasif, favorisant une récupération plus rapide après les injections oculaires chez les modèles murins. Les travaux futurs incluront l'utilisation de souris *knock-out* pour créer un modèle de maladie permettant l'internalisation de l'ARNm dans des expériences *in vivo*.

La discussion des résultats des chapitres précédents est présentée dans le chapitre 6. Le chapitre 7 présente également des travaux futurs et les conclusions tirées des recherches menées dans cette thèse, suivi de la bibliographie et des annexes contenant des figures supplémentaires.

ABSTRACT

Worldwide, over 2.2 billion people suffer from near or distance vision impairment, and for at least 1 billion of them, this impairment could have been prevented or remains unaddressed. Within the various causes of vision impairment, corneal endothelial diseases are affecting life quality of close to 250 million people worldwide. The only alternative nowadays, is corneal transplantation, a highly invasive method with undesired side effects such immune response leading to tissue rejection, enfeebling of endothelial cells and transplant failure.

Among all the endothelial ailing, Fuchs endothelial corneal dystrophy (FEDC) is the most common and the number one reason for corneal transplantation worldwide. An extra concern is the shortage of healthy tissue for transplantation. Virus-based therapy and electroporation are under investigation in ophthalmology, nevertheless, high immunogenicity and low specificity are still a concern. In terms of annual costs, the health care system projects a rise in cost of 30 billion dollars by 2032 only in Canada.

In order to minimize some of the drawbacks of current procedures, we propose a gene therapy treatment technique using a clinically approved femtosecond (fs) laser and gold nanoparticles (AuNPs) for the delivery of genes in corneal endothelial cells (CECs). The main contribution that our technique offers is the *in situ* treatment, avoiding transplantation, having a high efficacy and virus-free technique with double specificity, given by the focalized laser and the implementation of functionalized AuNPs situated at the membrane of targeted cells.

The main hypothesis is that by using a tightly focused femtosecond laser (currently used for ophthalmic purposes) to irradiate CECs whose membrane will be decorated with AuNPs (biocompatible material), transient pores (governed by the presence of the AuNPs) can be opened in the cellular membrane with high precision facilitating the delivery of exogenous molecules such as mRNA to perform gene therapy.

Chapter 1 provides a brief introduction to the topic, followed by a detailed literature review in Chapter 2. Based on the presented hypothesis, ocular cells were used in Chapter 3 to test the proposed technique *in vitro*. To establish the proof of concept with different exogenous molecules, *in vitro* experiments were performed followed by *ex vivo* tests to achieve four main objectives of this work:

- (i) **establish a proof of principle using ocular cells *in vitro* for subsequent application in mice;**

- (ii) **develop a safer protocol for intracameral injection in murine models for better AuNPs delivery in the anterior chamber;**
- (iii) **achieve a significant transfection of mRNA in the murine model with high cell viability *ex vivo*;**
- (iv) **provide a customizable technique between different animal species to ensure future safe implementation in human corneas.**

As detailed in Chapter 4 (paper 1) an improved protocol for intracameral injections was successfully implemented in the murine model, minimizing corneal damage and ensuring the maximum number of NPs reaching the desired corneal layer. The injections consisted in a solution of functionalized colloidal AuNPs mixed with exogenous molecules whose fluorescence is only visualized if the molecules are internalized in the targeted cells.

Studies regarding the material and the dimensions of the needles were made, as well as on their tip geometry. Commercial microneedles were laser-machined in order to improve the way the needles were entering in the anterior chamber (AC).

After successfully refining the intracameral injection technique, the developed protocol was employed in Chapter 5, which details the study of the second and third primary objectives of this work. Optoporation and transfection of CECs *ex vivo* in two different species, mouse and rabbit are detailed. A femtosecond laser was employed to study the parameters of irradiation for optoporation and transfection of CECs. Two types of animal models were tested to provide a complementary study.

Rabbit eyes were selected for their similarity in size to human eyes and the robustness of their cells. The primary difference between human and rabbit CECs is that rabbit CECs can replicate, making them suitable for quickly assessing viability. Once the proof of concept of our technique was demonstrated using rabbit corneas, transfection tests were successfully performed on murine corneas with larger molecules such as mRNA.

Ex vivo transcorneal irradiation using the proposed technique resulted in successful optoporation with high specificity and elevated efficacy ($49\% \pm 7$) due to the combination of low fluence scanning (optimal value: 100 mJ/cm^2 at $80 \text{ }\mu\text{m/s}$) and the use of AuNPs (88 ± 11 NPs/cell). Minimized side effects in the cornea are reported, allowing a highly localized treatment with cellular viability higher than 80% .

The implementation of this novel femtosecond laser and nanoparticle-assisted technique paves the way for gene and drug delivery therapy in the corneal endothelial tissue. The technique resulted in less invasive treatment anticipating a fast recovery after ocular injection in murine

models. Future work includes the implementation of knock-out mice for a disease model internalizing mRNA for *in vivo* experiments.

The discussion of the results of previous chapters is presented in Chapter 6 followed by conclusions and future work in Chapter 7. As part of future work, several improvements and suggestions regarding the limitations observed along with the study are discussed.

The bibliography and annexes, which contain supplementary figures are at the end of the thesis.

TABLE OF CONTENTS

DEDICATION	iii
ACKNOWLEDGMENTS	iv
RÉSUMÉ	vi
ABSTRACT	ix
TABLE OF CONTENTS	xii
LIST OF TABLES	xv
LIST OF FIGURES	xvi
LIST OF SYMBOLS AND ACRONYMS	xviii
LIST OF APPENDICES	xx
CHAPTER 1 INTRODUCTION	1
CHAPTER 2 LITERATURE REVIEW	5
2.1 The eye: an optical instrument	5
2.1.1 Image formation	5
2.1.2 The cornea	6
2.1.3 Corneal dystrophies	8
2.1.4 Current treatment techniques in clinics	10
2.2 Alternative treatments under research: Gene therapy	11
2.2.1 Laser-based gene therapy	13
2.2.2 Nanosecond regime	14
2.2.3 Picosecond regime	14
2.2.4 Femtosecond regime	15
2.3 Fs laser nanoparticle-mediated optoporation	16
2.4 Intracameral injections	21
CHAPTER 3 <i>IN VITRO</i> FEMTOSECOND-LASER NANOPARTICLE ASSISTED INTERNALIZATION OF EXOMOLECULES	25

3.1	Introduction	25
3.2	Materials and methods	27
3.2.1	Plasmonic material	27
3.2.2	Cells preparation	28
3.2.3	Exogenous molecules	29
3.2.4	Optical setup	30
3.3	Results	32
3.3.1	Plasmonic material	32
3.3.2	Internalization and cell viability rates <i>in vitro</i>	32
3.4	Conclusion and discussion	37
CHAPTER 4 ARTICLE 1: OPTIMIZATION OF INTRACAMERAL INJECTIONS		
	IN THE MOUSE EYE MODEL	40
4.1	Abstract	40
4.2	Introduction	41
4.3	Materials and Methods	42
4.3.1	Conception of a 3D holder and assembly for the mouse experiments	42
4.3.2	Optical coherent tomography visualization	42
4.3.3	Injection with a sharp needle puncture	42
4.3.4	Injection with a blunt needle through a corneal incision	44
4.3.5	Mouse preparation for <i>ex vivo</i> and <i>in vivo</i> experiments	45
4.3.6	Outcome parameters	45
4.4	Results	46
4.4.1	Stabilization of the mouse, the eye and the syringe	46
4.4.2	Injection with a sharp needle	47
4.4.3	Injection with a blunt needle through a corneal incision	49
4.4.4	Statistical analysis	51
4.5	Discussion	52
CHAPTER 5 FEMTOSECOND LASER GOLD NANOPARTICLE-MEDIATED <i>EX</i>		
	<i>VIVO</i> MRNA DELIVERY WITH HIGH SPECIFICITY IN CORNEAL ENDOTHE-	
	LIAL CELLS	56
5.1	Introduction	56
5.2	Results and discussion	58
5.2.1	AuNP incubation in <i>ex vivo</i> murine eyes	60
5.2.2	Optoporation and cellular transfection in <i>ex vivo</i> murine corneas	62
5.2.3	Lipofectamine assessment in <i>ex vivo</i> murine corneas	63

5.2.4	Optoporation and cellular fluorophore uptake in <i>ex vivo</i> rabbit corneas	64
5.3	Conclusion	65
5.4	Methods	66
5.4.1	Mouse cornea preparation	66
5.4.2	AuNPs	67
5.4.3	Fluorophores and chromophores	67
5.4.4	Optical setup	68
5.4.5	Optoporation, transfection and viability quantification	69
5.4.6	Transfection by lipofectamine	69
5.4.7	Rabbit corneas preparation	69
5.4.8	Imaging	70
CHAPTER 6	GENERAL DISCUSSION	71
CHAPTER 7	CONCLUSION	75
7.1	Summary of Work	75
7.2	Limitations	76
7.3	Future research towards <i>in vivo</i>	77
REFERENCES	79
APPENDICES	97

LIST OF TABLES

Table 3.1	Exogenous molecules for evaluation of fs and AuNPs-assisted uptake in ARPE-19 cells.	30
Table 3.2	Uptake percentage of exogenous molecules in ARPE-19 cells.	37
Table 4.1	Tested conditions for intracameral injection in the murine model.	51
Table 4.2	Logistic and linear regression for sharp needles.	52
Table 4.3	Outcome parameter comparison between sharp and blunt needles.	53
Table 5.1	NP assessment in <i>ex vivo</i> murine corneas.	62

LIST OF FIGURES

Figure 2.1	Structure of the human eye.	6
Figure 2.2	Corneal layers.	8
Figure 2.3	<i>Ex vivo</i> murine CECs staining.	10
Figure 2.4	Transfection mechanisms using pDNA and mRNA.	12
Figure 2.5	Chemical, biological and physical transfection methods.	13
Figure 2.6	Absorption coefficient of human skin in the VIS-IR range and Representation of an oscillating field with absorption cross-section of a metallic NP.	16
Figure 2.7	Effects produced by electromagnetic ultrafast laser interactions in nanostructures and surrounding medium.	18
Figure 2.8	Hemoglobin (Hb) and water have lower values of absorption at the biological spectral window.	19
Figure 2.9	Optoporation and cell transfection steps.	20
Figure 2.10	Ocular dimensions comparison between mouse, rabbit and human. . .	22
Figure 2.11	Different needle parameters reported in the literature.	23
Figure 3.1	Protocol for <i>in vitro</i> optoporation treatment with ARPE-19 cells. . .	29
Figure 3.2	Optical setup for <i>in vitro</i> optoporation and imaging.	31
Figure 3.3	NP assessment for optoporation optimization.	33
Figure 3.4	Fluence assessment for optoporation optimization.	35
Figure 3.5	Optoporation and viability tendencies for <i>in vitro</i> assessment.	36
Figure 4.1	Different configurations of injection and needle profiles.	43
Figure 4.2	Examples of the evaluation of ocular damage caused by intracameral injections.	46
Figure 4.3	3D printed holders for mouse stabilization.	47
Figure 4.4	Injection technique using sharp microneedles.	49
Figure 4.5	Self-sealing corneal incision injection technique.	50
Figure 5.1	Schematic representation of <i>ex vivo</i> transfection assessment.	59
Figure 5.2	AuNP assessment in murine eyes <i>ex vivo</i>	61
Figure 5.3	<i>Ex vivo</i> murine CEC viability and transfection.	63
Figure 5.4	AuNPs in <i>ex vivo</i> rabbit CECs, viability and fluorophore uptake. . . .	65
Figure A.1	Mouse eye globe immobilization.	97
Figure A.2	Montage used for OCT and color camera monitoring of injections. . .	98
Figure A.3	Anterior chamber imaging during injection.	99

Figure B.1	Murine CEC viability 48 hour post-irradiation.	101
Figure B.2	Murine CEC transfection 48 hour post-irradiation.	102
Figure B.3	3D design for rabbit and mouse eye holders.	103
Figure B.4	Rabbit CEC fluorophore uptake 48 hour post-irradiation.	105
Figure B.5	Rabbit CEC fluorophore uptake 48 hour post-irradiation.	106

LIST OF SYMBOLS AND ACRONYMS

AC	Anterior Chamber
ACD	Anterior Chamber Depth
ARPE-19	Retinal Pigment Epithelium cells
ARVO	The Association for Research in Vision and Ophthalmology
AuNPs	Gold Nanoparticles
BSS	Balanced Salt Solution
CD	Corneal Dystrophy
CECs	Corneal Endothelial Cells
CHED	Corneal Hereditary Endothelial Dystrophy
CNPs	Carbon Nanoparticles
CW	Continuous Wave
DAPI	4',6-diamidino-2-phenylindole
DMEM	Dulbecco's Modified Eagle Medium
DNA	Deoxyribonucleic Acid
FBS	Fetal Bovine Serum
FECD	Fuchs Endothelial Corneal Dystrophy
fs	Femtosecond
FWHM	Full Width at Half Maximum
GFP	Green Fluorescent Protein
IC3D	International Committee for the Classification of Corneal Dystrophies
IR	Infrared
mRNA	messenger Ribonucleic Acid
MVL	Minimum Visible Lesions
NA	Numerical Aperture
Nd:YAG	Neodymium-doped Yttrium Aluminium Garnet
NIR	Near-Infrared
NPs	Nanoparticles
ns	nanosecond
OCT	Optical Coherence Tomography
PBS	Phosphate-Buffered Saline
pDNA	plasmid Deoxyribonucleic Acid
PEG	Polyethylene Glycol
PI	Propidium Iodide

ps	picosecond
RA	Regenerative Amplifier
RLM	Reflected Light Microscopy
RNA	Ribonucleic Acid
siRNA	small interfering Ribonucleic Acid
Ti:Sapphire	Titanium-sapphire
UV	Ultraviolet
ZO-1	Zonula Occludens-1

LIST OF APPENDICES

Appendix A	SUPPLEMENTARY MATERIAL FOR OPTIMIZATION OF INTRA-CAMERAL INJECTIONS IN THE MOUSE EYE MODEL	97
Appendix B	SUPPLEMENTARY MATERIAL FOR FEMTOSECOND LASER GOLD NANOPARTICLE-MEDIATED <i>EX VIVO</i> MRNA DELIVERY WITH HIGH SPECIFICITY IN CORNEAL ENDOTHELIAL CELLS . . .	100
Appendix C	ARTICLE 2: DYNAMIC MULTISPECTRAL DETECTION OF BACTERIA WITH NANOPLASMONIC MARKERS	107

CHAPTER 1 INTRODUCTION

Vision loss can be associated with dystrophies and ocular diseases that are genetically inherited or developed by aging [1]. According to a report from the World Health Organization, approximately 2.2 billion people are blind or partially sighted around the world of whom around 800,000 affected people are in Canada [2]. This has an impact not only on the concerned population but also on health-care costs [3]. Globally, the leading causes of vision impairment are refractive errors, but among all the eye diseases, the corneal dystrophies are one of the major causes of blindness, especially the endothelial dystrophies [4].

Early treatment is fundamental for dystrophies that can cause vision loss such as Fuchs (progressive and hereditary disease named in honour of the Austrian ophthalmologist Ernst Fuchs [5]) and CHED (Congenital Hereditary Endothelial Dystrophy). Those dystrophies are asymptomatic in early stages, and conversely, when the disease is too advanced, the only option for the patient is transplantation. Such a surgical procedure has many drawbacks, including not only cell attrition and graft failure or tissue rejection [6], [7], but also the elevated cost of the surgery and the lack of tissues for transplantation [8].

Current research involve virus and electric fields to treat the cornea, nevertheless, viral vectors are a concern in medicine due to high immunogenicity and lack of specificity. On the other side, electric field-based treatments are highly invasive. Detailed information can be found in Chapter 2 (literature review).

This project aims to address this major health problem and offer an alternative treatment minimizing the drawbacks of the current techniques. **The main objective is to develop a non-invasive gene therapy method based on plasmonic nanoparticles (NPs) made of biocompatible material such as gold, combined to laser therapy. The main contribution is based on high selectivity of this technique (negligible side effects) and its translatability to different animal species and humans.**

The proposed wavelength is centered in the biological window where the absorption of the tissue is minimal. By combining the selected wavelength with the gold NPs (AuNPs), we not only overcome the lack of specificity of the currently investigated transfection methods, but also provide a less invasive therapy at the same time than decreasing the power used in the treatment reducing side effects. Experiments were conducted to achieve four sub-objectives of this work: **i) establish a proof of principle using ocular cells *in vitro* for subsequent application in mice;**

- ii) develop a safer protocol for intracameral injection in murine models for better AuNPs delivery in the anterior chamber (specifically corneal endothelial cells - CECs);
- iii) achieve a significant transfection of mRNA in the murine model with high cell viability *ex vivo*;
- iv) provide a customizable technique between different animal species to ensure future safe implementation in human corneas.

Laser therapy using femtosecond lasers has been reported in the literature by different groups, proving that temporary openings can be observed after irradiation in diverse cell membranes. This is achieved through the precise application of tightly focused beams within the near infrared (NIR) biological window (650-1350 nm) [9]. Our contribution involves the integration of plasmonic NPs, aimed at minimizing the required power. This, in turn, mitigates potential treatment side effects in the surrounding areas.

The general idea is to inject functionalized colloidal AuNPs mixed with the desired gene to be internalized in CECs into the anterior chamber to subsequently irradiate with a tightly focused femtosecond laser.

The main hypothesis is that the functionalized AuNPs will specifically bind to the CECs. When irradiated, AuNPs will concentrate the energy from the laser leading to a nanocavitation effect producing transient pores in the cell membrane. Under this principle, a second hypothesis is that by increasing the amount of NPs per cell (below toxicity threshold) the energy needed for optoporation can be lowered. On the same note, the optoporation will allow the internalization of genes (transfection) with high viability after treatment as a ultimate goal of the study.

Following the above mentioned objectives, our technique was first tested *in vitro* using ocular cells (ARPE-19) to verify the feasibility and optimize parameters with the optical system to subsequently move to animal models. Chapter 3 is specifically allocated to detail the findings derived from the research conducted on retinal cells. It is worth mentioning that the selection of this retinal cell line for initial testing was driven by its availability in the laboratory and its convenient manipulation regarding higher adherence to the substrate when compared to CECs.

On the other hand, for *ex vivo* studies, the rationale using two different animal models relays in doing a complementary study. The rabbit eyeball is proportional in size to the human eye, while mice can be used to model the pathology with the phenotypic expression. Several eye diseases are first reproduced in mice since they provide a broad range of parameters for

research with responses that are close to human pathologies [10,11].

As previously stated, our focus lies on the cornea, the sole transparent tissue in the human body. Specifically, our target are the endothelial cells, which form a honeycomb-like monolayer, constituting the innermost layer of the cornea. To optimize the number of NPs reaching the endothelium and enhance the treatment efficacy with the femtosecond laser, intracameral injections were imperative.

This type of injections are a common procedure in humans, not only easy to perform by a clinician but with minimal discomfort for the patient. As anticipated, achieving successful injections with rabbit samples was straightforward using the standard needles commonly used in clinics.

On the other side, due to the anatomy and size of the mouse eye, the injection technique needed to be studied and adapted, dedicating Chapter 4 of this thesis to intracameral injection in murine models (submitted article). We have studied the implication of different needle sizes and tip profiles for intracameral injections in the mouse model. We propose two techniques that can be implemented in the laboratory to improve reproducibility and reduce leakage and damage when performing injections in the AC for the murine model.

Following injection, AuNPs presence in rabbit and mouse corneas was assessed using reflected light microscopy (RLM). The toxicity of the plasmonic material was evaluated using a standard cell viability assay (Calcein-AM) followed by fluorescence microscopy imaging. Subsequently, tissue irradiation was conducted using our proposed optical system, centered around a Ti-sapphire femtosecond laser operating at 800 nm, equipped with an amplification system enabling kHz repetition rates (using 1 kHz) and delivering pulses of 45 fs duration.

Negative controls were implemented to exclude laser-induced damage in the absence of AuNPs. Additional control groups were employed to assess AuNPs toxicity without laser irradiation, as well as cell viability in the absence of both laser and NPs. High optoporation rates with high viability is reported. The combination of a femtosecond laser with plasmonic NPs, resulted in an enhanced effect that facilitates the selectivity of cells for optoporation. Detailed information can be found in Chapter 5 of the thesis based on a submitted article.

As a future work, it is proposed to evaluate the long-term effect of the gene therapy by monitoring the presence of fluorescence on the transfected cells *in vivo*.

As a summary, taking advantage of the plasmonic effect of AuNPs when excited with femtosecond pulses, this thesis presents a successful technique for optoporation and subsequent transfection. Among the advantages of this technique, it is notable that such lasers are already approved for clinical use, such as in laser surgery for correcting refractive problems. In

this case, we propose to extend its use for correcting genetic dystrophies.

The deposited energy is not only within the biological window but also well below the minimal visible laser lesion threshold of the cornea, making side effects on the rest of the corneal layers negligible. Additionally, AuNPs are biocompatible, and our toxicity tests have confirmed that the concentrations used in this work are safe for murine and rabbit CECs. Initially, the technique was tested in ocular cells, demonstrating proof of concept *in vitro*.

Ultimately, the technique aims to overcome drawbacks of the only clinically approved treatment in humans, corneal transplantation. To demonstrate the translatability of the technique to different species and advance to *ex vivo* experiments, rabbit and mouse models were selected. The robustness of rabbit CECs and their replicative ability allowed for a quick viability test post-treatment, with characteristics similar to human anatomy. The technique was subsequently translated to mice, widely used as models in diverse diseases.

For this study, AuNPs needed to be in contact with CECs, delivered most effectively via intracameral injection. An improved protocol minimizing damage such as bleeding, corneal collapse, and cellular death was successfully implemented to subsequently perform the laser treatment. Several 3D models were designed to improve visualization, incubation, and positioning of the diverse stages of the samples. The 3D designs are available in appendices. The results presented in this thesis are solid enough to suggest future *in vivo* tests in murine models.

Anticipated limitations include animal breathing when focusing the laser within the sample, changing the position where the focalized light will interact with the tissue. Thus an autofocus system is suggested. A consideration for treating diseased mice is that treatment must occur before the pathology is visible, in the early stages of the disease when the cornea is still transparent. *In vivo* experiments will provide a follow-up exceeding 48 hours, helping determine the final success rate of the transfection technique before translating it to human samples.

CHAPTER 2 LITERATURE REVIEW

This multidisciplinary project encompasses three main topics: Ophthalmology, Optics, and Nanoplasmonics; a brief literature review of each subject is presented in this section. Key concepts are introduced to provide a comprehensive understanding of the entire thesis.

This literature review begins with an introduction to eye anatomy and its optical properties, followed by an overview of specific corneal diseases targeted for treatment and current approaches in gene transfection. Finally, laser-assisted nanosurgery is discussed, including the proposed nanoplasmonic approach for corneal treatment.

The primary motivation for developing an alternative technique for the treatment of corneal endothelial dystrophies stems from the high incidence of vision impairment in the population, the elevated cost of treatments, and the limitations of current methods. To better understand the impact of this significant health issue, relevant statistics on ocular problems are presented.

2.1 The eye: an optical instrument

The human eye, approximately 24 mm in diameter, functions as an optical system sensitive to wavelengths between 380 and 760 nm. It comprises three main compartments: the anterior chamber (AC; between the cornea and iris), the posterior chamber (between the iris, ciliary body, and lens), and the vitreous chamber (between the lens and retina) [12]. Stable internal pressure, higher than atmospheric pressure, maintains the eye's transparency and shape by regulating aqueous fluid production in the ciliary body [13]. Six extra-ocular muscles enable rotation. The key components include the cornea, pupil, iris, retina, optic nerve, choroid, and vitreous (see Figure 2.1).

2.1.1 Image formation

In the eye, light follows a pathway similar to that of a camera lens. It enters through the cornea, a quasi-spherical structure with an 8 mm curvature radius, then passes through the aqueous humor to reach the crystalline lens located behind the pupil and controlled by the iris. The lens refracts the light, which continues through the vitreous humor until it reaches the retina, an extension of the central nervous system. Here, the image is inverted, and electrical signals containing information are transmitted via the optic nerve to the brain, where they are processed and re-inverted into their original configuration [14].

The pupil regulates the intensity of light reaching the retina. Light passes through the

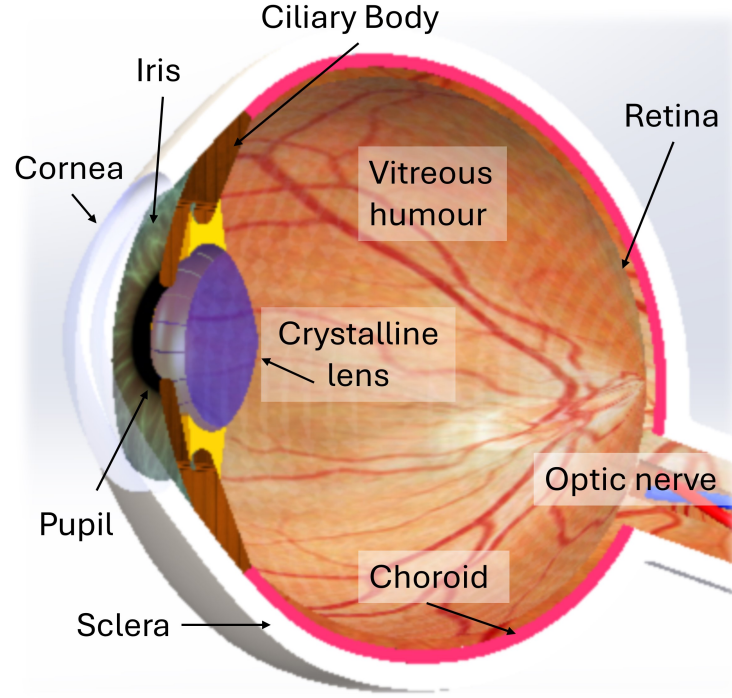


Figure 2.1 Structure of the human eye.

crystalline lens, which is a dynamic structure capable of adjusting its shape with the ciliary muscle to enable accommodation, focusing objects at different distances. The light is finally focused on the retina (the neural portion of the eye), a light-sensitive tissue consisting of pigmented layers and nerve fibers that forms part of the central nervous system [15].

The cornea and lens work together as an optical system for optimal image quality. Nevertheless, if the cornea presents some alterations in shape or transparency, the image can be altered. This type of problems are present in people with refractive problems or corneal dystrophies [16].

2.1.2 The cornea

The cornea is the most anterior surface of the eye, and the only transparent tissue in the human body, comprising a thin layer of 0.595 ± 0.041 mm thick [17] and 11.71 ± 0.42 mm in diameter [18]. It functions as a lens with fixed optical power and consists of five distinct layers (see Figure 2.2A), each performing specific roles in maintaining the eye's pressure and moisture [16].

Refraction occurs at four surfaces: the anterior and posterior interfaces of the cornea and the lens. However, two-thirds of the refractive power of the eye is attributed to the cornea.

Each layer of the cornea has its own refractive index (RI), but conventionally, an RI of 1.37 is used corresponding to the corneal stroma [19].

Starting from the outermost layer of the eye, the first layer is the corneal epithelium, which consists of about six layers of cells. These cells are kept moist by a tear layer, providing a smooth surface that enhances image quality. The epithelium is crucial for the eye's overall refractive power, its cell regeneration occurs through multiplication in the basal layer.

The second layer of about $14\ \mu\text{m}$ in thickness is known as Bowman's layer. It is composed primarily of collagen fibrils and serves to protect the corneal stroma which is the third layer. The stroma, is a transparent middle layer made of collagen fibers and keratocytes. It contains around 200 layers of collagen, each $1.5\text{--}2.5\ \mu\text{m}$ thick, arranged in parallel orientation, and constitutes about 90 % of the corneal thickness [20].

The fourth layer, the Descemet's membrane, is formed of collagen fibrils and its thickness ranges from $5\text{--}20\ \mu\text{m}$, depending on age. The innermost layer is the endothelium, a $5\ \mu\text{m}$ thick monolayer of hexagonal cells (see Figure 2.2B.i). This layer is particularly relevant to the research presented, as endothelial dystrophies mainly affect this cell layer. Dysfunction of endothelial cells can reduce corneal transparency, potentially leading to blindness in severe cases.

The primary function of the endothelium is to regulate nutrient transport between the stroma and the aqueous humor. Unlike epithelial cells, endothelial cells cannot regenerate; instead, they stretch to cover dead cells (see Figure 2.2B.ii). As individuals age or develop diseases, dead cells accumulate, and stretching compensates for this loss [12].

However, this compensation reduces cell density and impairs the fluid transport efficiency. Low pumping efficiency causes the stroma to swell in response to excess fluid, which affects corneal transparency. Figure 2.2B.iii, shows a fluorescent image of a corneal tissue with the formation of a *guttae*, from the Latin *drops* [21]. A strong fluorescence background is present at the *guttae* site as a result of the staining from the collagen produced by stressed CECs.

The average cell density varies by species and age, in adult humans, it typically ranges from 2,500 to 2,700 cells/mm² [22]. In the case of rabbit, reports suggest 2,307 cells/mm² [23] while for mice the numbers range from 2,004 to 2,243 cells/mm² [24, 25].

For optimal vision, the cornea must remain transparent to effectively transmit and refract light onto the retina. Proper functioning of all corneal layers is essential to protect intraocular structures from pathogens and traumas. Nevertheless, patients with corneal dystrophies can experience poor image quality or vision loss in the most severe cases as detailed in the

following section of this thesis.

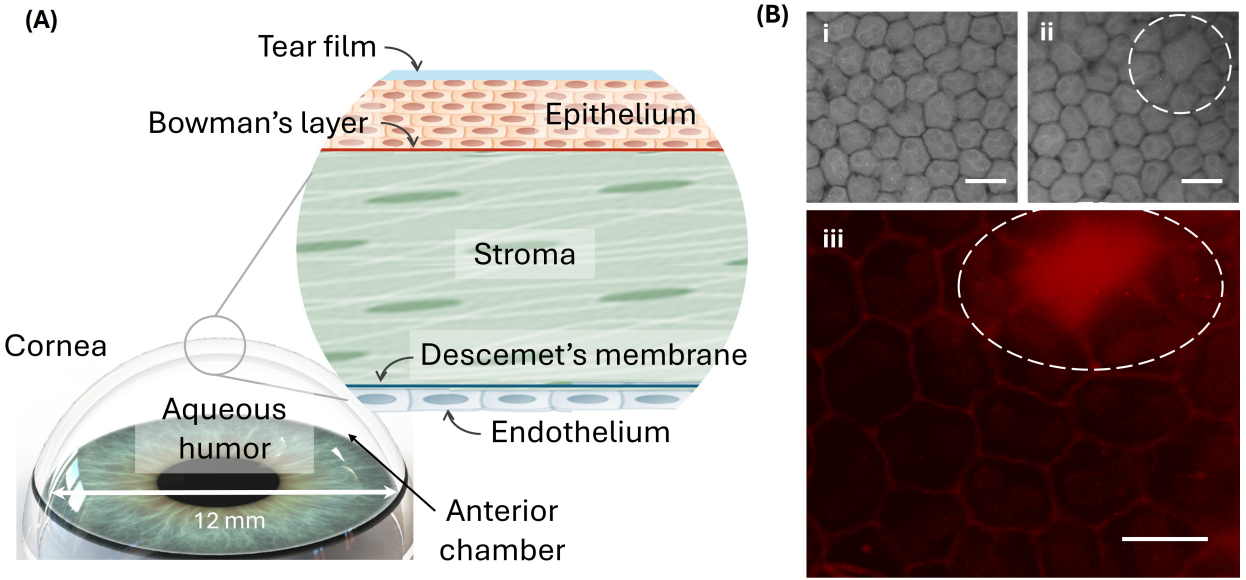


Figure 2.2 Corneal layers: **(A)** Schematic representation of the different layers of the cornea. **(B)** i-Bright field image of healthy murine CECs; ii- stretched cell indicated with a dotted line in the upper right corner; iii- fluorescence image of a murine tissue with missing cell. Scale bar corresponds to 20 μm for all images.

2.1.3 Corneal dystrophies

According to a report by the World Health Organization, approximately 2.2 billion people worldwide are blind or partially sighted, with around 800,000 of these individuals residing in Canada [26,27]. This widespread vision impairment impacts not only the affected population but also contributes significantly to healthcare costs [28]. Globally, the leading causes of vision impairment are refractive errors [29]. Among various eye conditions, corneal diseases, particularly endothelial dystrophies, are major contributors to blindness [30].

Corneal dystrophies (CD) are typically hereditary and progressive diseases that lead to various complications for the patients. Currently, more than 20 different corneal dystrophies have been identified. These are classified based on the affected anatomical site and include epithelial/subepithelial, epithelial-stromal, stromal, and endothelial dystrophies [31,32].

Among the corneal dystrophies that can cause vision impairment, particularly those affecting the posterior part of the cornea, Fuchs Endothelial Corneal Dystrophy (FECD) and Congenital Hereditary Endothelial Dystrophy (CHED) are the most common. These conditions involve progressive dysfunction of the endothelial layer, leading to corneal swelling [33].

In the early stages, symptoms include reduced vision upon waking and blurry images that often improve throughout the day. As the disease progresses, the vision becomes persistently blurred, and hypersensitivity to light may develop. In the later stages, patients may experience pain and corneal opacity, severely impairing vision [34,35].

According to the International Committee for the Classification of Corneal Dystrophies (IC3D), FECD is classified as a category 1 dystrophy, indicating that it is a well-defined condition with mapped and identified genes and known specific mutations. In terms of genetics, the loss of function of a transporter called SLC4A11 is the main consequence for both dystrophies [32]. The pathogenic implication in the CECs dystrophies is related to mutations in several genes such as VSX1 in different diseases such as Posterior Polymorphous Corneal Dystrophy (PPCD1), COL8A2 in PPCD2 and FECD, ZEB1 for PPCD3 and FEDC, among others [36].

As mentioned previously, the endothelium is a monolayer of cells that has a honeycomb-like disposition when viewed from the posterior side. At birth, this monolayer is about 10 μm in thickness becoming 4 μm in adulthood [37,38]. Its density and topography change throughout life, nevertheless, there is no evidence about its multiplication or regeneration in humans. For this reason, it becomes important to have specialized treatments for battling the associated dystrophies.

Several clinical techniques are used to evaluate the health condition of the cornea. Slit-lamp biomicroscopy provides a detailed view of the corneal structure [39], while keratometry and corneal topography offer information regarding its curvature [40]. Pachymetry measures corneal thickness [41], and *in vivo* confocal microscopy provides real-time, detailed images of all corneal layers [42].

In research, reflected light microscopy and fluorescence microscopy are the two most commonly used tools to examine different layers of the cornea. Various chromophores and fluorophores can be used to visualize specific tissue parts. As shown in Figure 2.3A, alizarin red combined with trypan blue is used in bright field imaging to evaluate the endothelium and quantify cell viability. On the other side, fluorophores such as ZO-1 stain membrane junctions (red fluorescence) [43], while DAPI is used to color cell nuclei (blue fluorescence) as seen in Figure 2.3B.

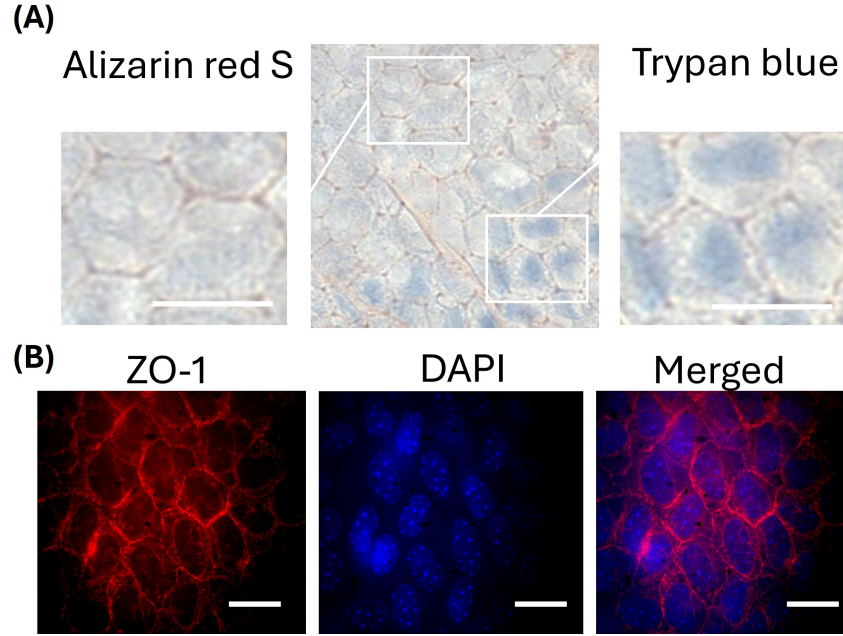


Figure 2.3 *Ex vivo* CECs staining using (A) chromophores for membrane junction (alizarin red S) and dead cell nuclei (trypan blue); and their equivalent (B) fluorophores for membrane (ZO-1) and nuclei (DAPI in blue) - in this case DAPI stains nuclei of live and dead cells. Scale bar corresponds to 20 μm for all images.

2.1.4 Current treatment techniques in clinics

The different treatments for Fuchs dystrophy include eye drops, ointments, and special contact lenses to help reduce corneal swelling in the early stages of the disease. For more severe cases, corneal transplantation is the only alternative [44].

A study conducted in Canada and published in the Canadian Journal of Ophthalmology estimated the cost of corneal transplantation for the Quebec healthcare system to be approximately CAD 3,171 per patient, including medical follow-up for three years post-surgery. This represents a significant expense for the healthcare system [8].

In addition to the elevated cost, complications such as ocular hypertension, graft failure, and, in the worst cases, rejection can occur after transplantation [45, 46]. To address these issues and reduce both costs and risks, alternative treatments are being explored.

Side effects from current treatments highlight the potential of gene therapy, where genetic conditions or diseases can be treated by modifying or replacing a defective gene. Gene therapy offers a solution that addresses the root causes of the disease, aiming for a cure rather than merely suppressing symptoms [47].

2.2 Alternative treatments under research: Gene therapy

Since genes responsible for endothelial dystrophies have been identified [32], gene therapy offers a promising, minimally invasive alternative treatment. This approach typically involves replacing, inactivating, or introducing genes into cells (transfection) to correct the genetic disorders.

Nucleic acid therapeutics have garnered global interest due to their potential to address severe inherited and acquired genetic diseases. Clinical trials have explored gene therapy for various conditions, including cardiovascular and neurodegenerative diseases, as well as different types of cancers [48–50]. The biggest challenge is the effective and selective introduction of plasmid or modified genes into the target cells.

The most common nucleic acids are plasmid DNA (pDNA) or small interfering RNA (siRNA) to either induce or suppress the expression of a specific protein [51]. Another option is the use of messenger RNA (mRNA) considered as a promising alternative to pDNA since it does not need to be inserted into the host genomic DNA (genotoxicity) [52]. Avoiding genotoxicity issues linked to chromosomal insertion of DNA vectors makes this method a suitable alternative for transfecting non-proliferative cells in clinical gene therapy [53,54].

Transfection with DNA occurs when the vector enters the cell and is transported to the nucleus. Once inside the nucleus, the DNA is transcribed by the host cell's machinery into RNA. This RNA is then exported to the cytoplasm, where it can either promote or downregulate the production of a specific protein (see Figure 2.4A) [55].

In the case of mRNA, transfection occurs when the molecule enters the cytoplasm. Once inside, it is translated by the ribosomes of the cell into the desired protein (see Figure 2.4B). The expression of the protein can then be observed, often using fluorophores for visualization. Over time, the mRNA is naturally degraded by cellular enzymes [56].

It has been demonstrated that transfection efficiency decreases as the size of the transferred molecules increases. Moreover, the tertiary structure of these molecules has also an impact [57].

The size of plasmid molecules varies based on the length of the encoded protein. pDNA structures are about 2.5 nm in diameter, nevertheless studies show that some molecules such as GFP pDNA go up to 4 nm [58]. On the other side, mRNA molecules are about 1,000 to 3,000 nucleotides long, with each nucleotide being approximately 0.34 nm in length. The average mRNA molecule length can vary from 340 nm to 1,020 nm. However, the physical conformation is more complex due to the three-dimensional structure and folding of the mRNA. Considering the overall folded size, an mRNA molecule can have a diameter of about

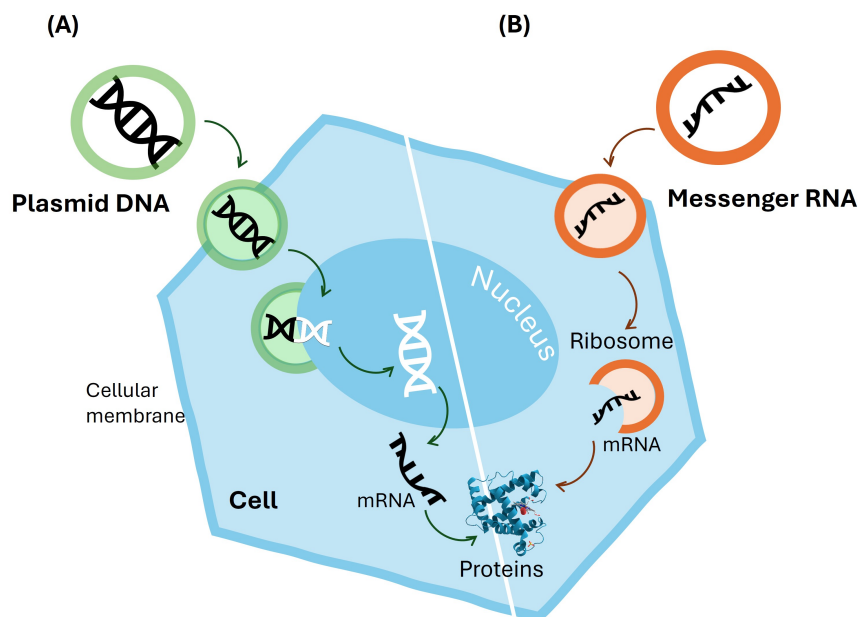


Figure 2.4 Transfection mechanisms using (A) pDNA and (B) mRNA.

10-30 nm, depending on its secondary structure and interactions with other molecules [59,60].

In general, the selection of the most effective transfection method depends on the type of cells, and the introduced nucleic acids [61]. Most of the studies start by using small fluorophores such as propidium iodide (PI) or Calcein free-acid whose molecule size is <1 nm. Other intermediate molecules can be Dextran or oligonucleotides with associated fluorophores whose diameter is about 1.5 nm. Various methods have been studied to improve transfection efficacy. The techniques can be classified by their nature as chemical, biological, and physical approaches as shown in Figure 2.5 [62,63].

Chemical approaches using liposomes [64,65] and biological methods using viral vectors [66], often face drawbacks such as lack of specificity and potential toxicity due to viral mutations. Conversely, among the physical methods, microinjection [67] and electroporation [68,69] result in time-consuming and invasive approaches.

In the case of optical transfection, laser-based techniques, particularly femtosecond lasers, are employed to manipulate cell membranes and facilitate the uptake of various molecules. This method utilizes high numerical aperture objectives to precisely focus laser pulses to open transient pores (optoporation) in cell membranes, thereby enhancing the effect at targeted locations within the tissue [70,71].

The following section aims to summarize the application of various lasers emphasizing the

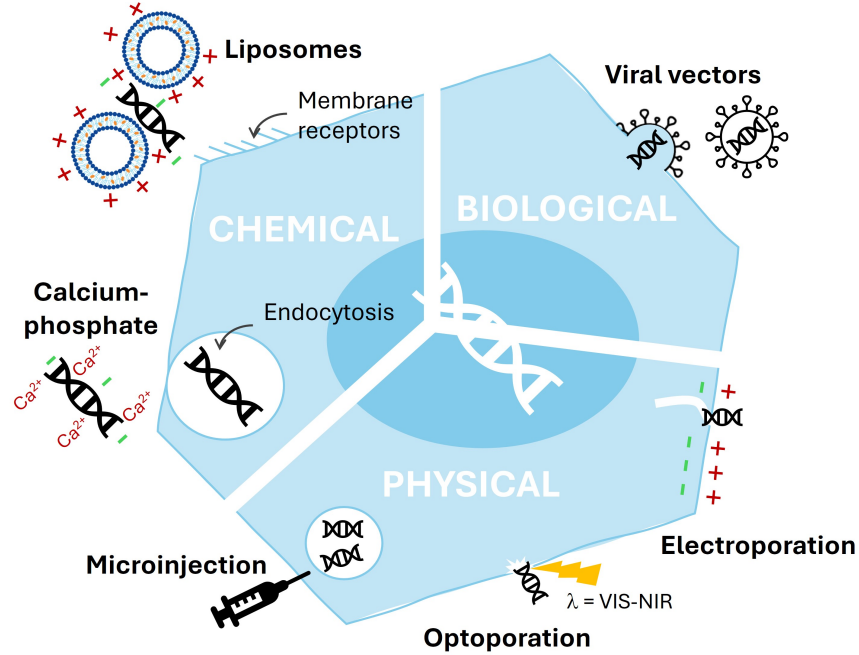


Figure 2.5 Chemical, biological and physical transfection methods.

advantages of their use in gene therapy.

2.2.1 Laser-based gene therapy

Different types of lasers are utilized for corneal reshaping by ablating the tissue to correct refractive errors [72]. Neodymium lasers are employed for treating conditions such as posterior capsule opacification and for certain corneal modifications [73–75]. Argon lasers are applied for photocoagulation in retinal disorders, [76] while Holmium lasers offer precision cutting for various corneal surgeries [77]. Finally, femtosecond lasers, are used to create precise corneal flaps and advanced procedures like corneal cross-linking [78, 79].

It is worth mentioning that to our knowledge, no results have been presented in the literature for *in vivo* transfection in corneal tissue. Nevertheless, *ex vivo* experiments have shown successful optoporation in cortical axons and retinal cells in murine eyes with femtosecond (fs) lasers [80, 81].

For this reason, we can emphasize the importance of having a research line that provides an alternative for corneal treatments. The main parameters to consider are the wavelength, the pulse duration, the energy, and the repetition rate. When working in the near-infrared (NIR) region, the main advantages are the strong confinement that can be achieved with specialized optics, as well as the localized matter-light interaction that is only achieved at the focal

volume. The short pulses have reduced thermal effects and mechanical consequences when compared to longer pulses [82–85]. The interactions can be laser-induced plasma-mediated ablation or laser-induced optical breakdown, offering high precision and manipulation of transparent samples [86–88].

Optoporation has been performed in different wavelength regimes such as continuous laser (CW), nanosecond (ns), picosecond (ps) and femtosecond (fs). A brief description of the mechanism of each regime is given in the following sections.

2.2.2 Nanosecond regime

The pulse duration in this regime is longer than the thermalization time of most metals, for this reason, lasers in this regime are commonly used for micromachining. It has been demonstrated that the pulse duration has an impact on the penetration depth and ablation threshold. If long pulse duration is used, the threshold fluence increases and the effective energy penetration depth decreases [89].

In the case where the pulse duration (τ_L) is larger than the electron-phonon energy-transfer time (τ_i), the electrons and lattice temperatures are at the same thermal equilibrium point ($T_e = T_i = T$). Thermal penetration is larger than optical penetration in this regime, which means that thermal waves can propagate in the target where the energy is absorbed, thus increasing the temperature in a local volume that depends on the diffusion coefficient. This could signify side effects if its application is in biological tissues.

On this note, the effect due to the interaction with prolonged energy exposure is mainly photothermal, turning into cellular vaporization. Lasers operating in this regime are used in different treatments such as cataracts for material removal [90] and refractive surgery [91,92].

2.2.3 Picosecond regime

When the pulse duration is shorter than the electron-phonon energy-transfer time, the lattice and the electrons have different temperatures, until the equilibrium condition is reached after a few tens of picoseconds. In terms of metals, the lattice temperature remains notably lower than the electron temperature, making the lattice contribution negligible during the non-equilibrium time range.

In biological media, the cooling down of the electrons gives an energy exchange that produces a plasma that expands at hypersonic velocity [93]. Subsequently, this plasma creates a cavitation bubble whose life-time is pulse width-dependent [94–96]. The effect of the bubble formation allows the rupture of the cell membrane, using this as a tool to produce a pho-

photodisruption in different tissues [97]. In terms of corneal applications, the main use is for the evaporation of tissue that will lead to the change in the refractive power of the eye [91, 98]. The effect that is expected with this type of lasers is photomechanical or photodisruptive, where the acoustic waves are produced acting with the thermal expansion after the laser-tissue interaction.

2.2.4 Femtosecond regime

The effects that are produced at the focal point of a tightly-focused femtosecond laser are widely used for micromachining of bulk transparent materials. Those effects are due to nonlinear interactions that produce breakdown offering in biological media a precise tool for photodisruptive surgery on single cell and tissue [99, 100].

In this regime, a femtosecond pulse duration is indeed much shorter than the temporal dynamics of the electron temperature. This effect permits a highly localized interaction of the light with the material, reducing the side effects that are usually observed when lasers are used for micromachining or biomedical applications.

Nowadays, the advantage of the limited side effects is used for the disruption of the cellular membrane such as optoporation. The aim of optoporation is the internalization of genetic material (transfection) or drugs that can be delivered locally and will help or contribute to the improvement of the biological system.

The used wavelength is in the NIR, because of the low absorption and the low scattering coefficients that biological tissues present when irradiated in this regime (see Figure 2.6A), thus minimizing the heat transferred by the electromagnetic wave to the cells. Besides, this approach maximizes the penetration depth, opening the possibility to reach sub-layer cells on *in vivo* specimen [101].

As mentioned previously, the use of high numerical aperture (NA) objectives is common due to the lateral confinement and the depth control that can be achieved. Beam shaping has been also studied since 1990 when a laser beam delivery system using axicon beam shaping was implemented in corneal surgery [102]. Since then, it was shown that the uniformity of the cut in the surgery was directly related to the radial symmetry of the beam, having different effects due to photothermal, photodisruptive or photochemical interactions based on the energy exposure and wavelength.

In summary, fs lasers are preferred for their ultra-short pulse duration that allows high peak power. This minimizes side effects due to the negligible heat diffusion to surrounding tissues. Additionally, biological tissues exhibit lower absorption in the NIR range, enabling deeper

penetration [103].

Based on laser-tissue interaction studies, other tools have been tested to increase the efficiency of the treatments, always looking for less invasive methods and producing fewer side effects. Recently, NPs have been applied in different areas offering the possibility of effectively delivering more energy for tissue treatment and cell surgery with limited side effects. The implementation of different materials has been studied from carbon-based particles, polymeric materials and metallic such as gold and silver among others.

The next section is dedicated to the implementation of different nanomaterials to assist optoporation.

2.3 Fs laser nanoparticle-mediated optoporation

It has been proved that NPs enhance the efficacy of laser-based cell surgery by acting as contrast agents, which reduces the energy required for treatment. A localized enhancement of the energy leads to the disruption of cellular membrane when the plasmonic material is in close contact with cells. On this note, the use of carbon NPs [104], nanorods [105], spherical NPs [106–109], nanostars [110,111] and, nanoshells [112,113] have been reported.

In light-matter interactions, the oscillation of the collective conduction electrons can be in phase with the incident field for a certain range of wavelengths thus creating a so-called localized plasmon resonance as shown in Figure 2.6B. This phenomenon can be described by Mie theory, with a mathematical formulation to obtain the absorption and scattering response of a sphere when irradiated with an electromagnetic wave [114]. An example of the response of a AuNP of 100 nm in diameter can be observed in Figure 2.6C.

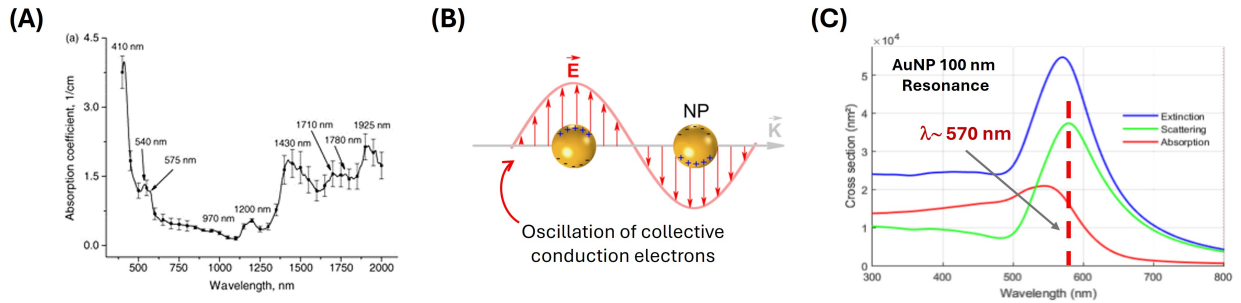


Figure 2.6 (A) Absorption coefficient of human skin in the VIS-IR range, adapted from [96]. (B) Representation of an oscillating field around metallic NPs, adapted from [115]. (C) Representation of the absorption cross-section of a AuNP.

The plasmon peak or plasmonic resonance value depends on size, shape, composition and

local environment or medium of the particle. For aqueous biological environments, water is typically used as an approximation for the medium, as biological media is predominantly composed of water.

Short pulses can locally interact not only with the NP but also the surrounding water and the energy transfer time (τ_T) can be estimated with the equation 2.1, under the condition: $\tau_T \approx \tau_P$ where τ_P is the laser pulse duration.

$$\tau_T = \frac{(\rho C r_0^2)}{(3k_w)} \quad (2.1)$$

ρ is the NP density, C the heat capacity of the NP, r_0 the radius of the NP and k_w the thermal conductivity of the surrounding water [94,116].

If the pulse length is shorter than the electron-phonon equilibrium time, which means using femtosecond lasers, the energy of the laser will only interact with the electrons that are out of equilibrium with the phonon subsystem. That means that the laser will excite the plasmon oscillation which will decay into a non-thermal electron distribution that thermalizes to a Fermi-Dirac distribution in a timescale ≈ 500 fs (see Figure 2.7A). The heat transfer equation can be now rewritten using a hyperbolic two-temperature model (HTTM), which at the same time, can be reduced to the parabolic two-temperature model for femtosecond pulses interacting with nanostructures as can be seen in equations 2.1 and 2.2 (complete information and derivation of the equations can be found in Boulais *et al.* 2013 [94]).

$$C_l(T_e) \frac{(\partial T_e)}{\partial t} = -(k_l \nabla T_l) + G(T_e - T_l) \quad (2.2)$$

Where G is the electron-phonon coupling constant with a value of $2.5 \times 10^{16} \text{ Wm}^{-3} \text{ K}^{-1}$ for gold at room temperature.

When the energy absorbed by the NP (short pulse) is transferred into the surrounding media, the effect can produce a localized phase change of properties that may lead to a transient bubble formation (normal boiling is due to heterogeneities in the liquid), the timescale where the energy is transferred to the water corresponds to the phonon-phonon scattering time that is in hundreds of picoseconds. This phenomenon is called heat-mediated bubble nucleation (see Figure 2.7B).

On the other hand, when using ultrashort pulses, the cavitation takes place thanks to the high intensity of the electric field and the near-field enhancement around the NP. A non-linear absorption occurs directly in the water and plasma is generated. The diffusion takes place and the energy is transferred to the water molecules producing a pressure increase and

subsequently, a bubble is formed. This phenomenon is then called plasma-mediated bubble nucleation and can be visualized in Figure 2.7C. It has been reported that the pulse width has an important influence on the threshold of the bubble formation. Indeed, when it increases, the vapour bubble threshold also increases depending on the NP size, because the thermal confinement is reduced [117,118].

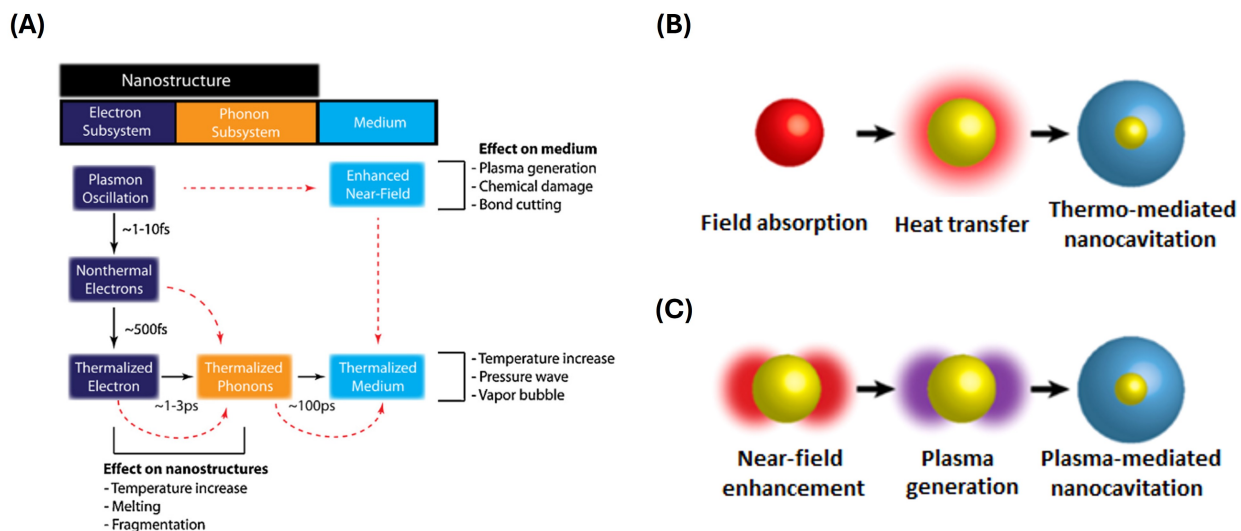


Figure 2.7 (A) Effects produced by electromagnetic ultrafast laser interactions in nanostructures and surrounding medium adapted from: [94]; graphical representation of (B) Heat-mediated bubble nucleation and (C) Plasma-mediated bubble nucleation adapted from [94, 119].

It is important to determine the temperature of the NP since processes such as melting, and fragmentation can take place above certain fluence and irradiation frequency values. When irradiating with femtosecond pulses, the absorbed energy can be high enough to produce morphological and chemical changes in the nanostructures, as a consequence, melting or fragmentation processes can take place resulting in smaller particles that could be toxic for the biological system.

If the laser wavelength is in the regime of resonance of the NPs, the absorption of the energy is high enough to produce an effect of plasma generation that allows the formation of transient pores in the cellular membrane [86, 120]. It has been also proved that off-resonance transfection can be achieved, increasing the applications of the NPs and laser systems [117, 121].

For this work, off-resonance irradiation is considered since it allows for the utilization of lasers within the therapeutical window (see Figure 2.8) while having an enhanced interaction of AuNPs. The cornea and the anterior part of the eye are primarily composed of water.

However, the blood absorption curve was included to emphasize that our technique is safe for its implementation in ophthalmology due to the low absorption in the highly vascularized regions of the eye, such as the retina.

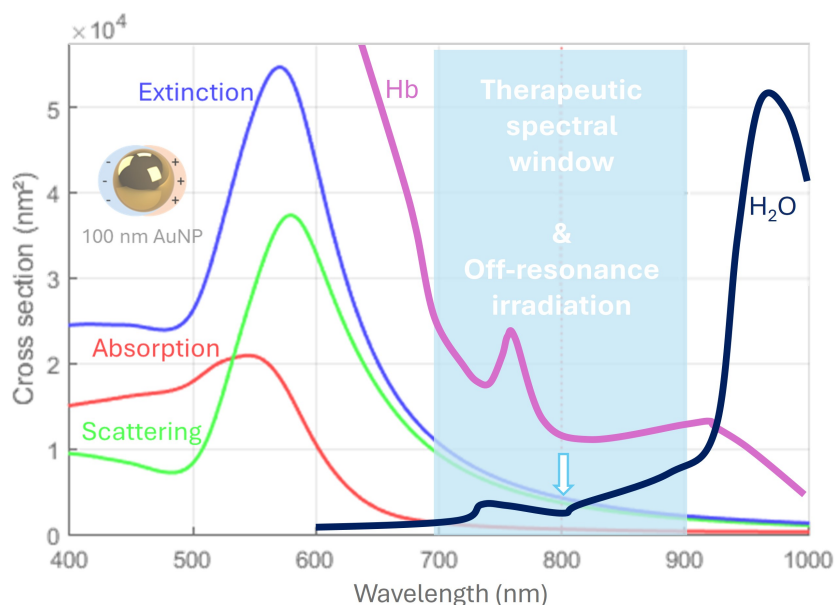


Figure 2.8 Hemoglobin (Hb) and water have lower values of absorption at the biological spectral window. Irradiation performed at 800 nm results in off-resonance phenomena minimizing side effects.

The implication of NPs in different medical treatments became popular due to the possibility of having localized treatment and selectivity with functionalized NPs [122]. The treatments are done *in vitro* and *in vivo*, opening new possibilities for molecule breaking procedures, cell nanosurgery, eye disease correction, DNA degradation, cancer treatment among others.

The permeabilization of the cellular membrane is one of the most important applications of the NP-assisted fs-laser treatment, as cavitation bubbles result in the formation of pores at the cellular level.

The technique starts by selecting the appropriate NPs, which can be functionalized to improve attachment (Figure 2.9A). These NPs are then incubated with the desired material to be internalized by the cells (Figure 2.9B). The next step is irradiation, where various parameters, such as pulse width, laser exposure time, or repetition rate, can be adjusted.

The membrane disruption is attributed to the formation of low-density plasma in the particle-enhanced near-field when the laser interacts with the plasmonic material (Figure 2.9C). The shock wave produced by nanocavitation will transiently disrupt the cellular membrane. Once permeabilization occurs, plasmids, fluorophores, or drugs for a specific treatment will interact

with the cell cytoplasm (see Figure 2.9D).

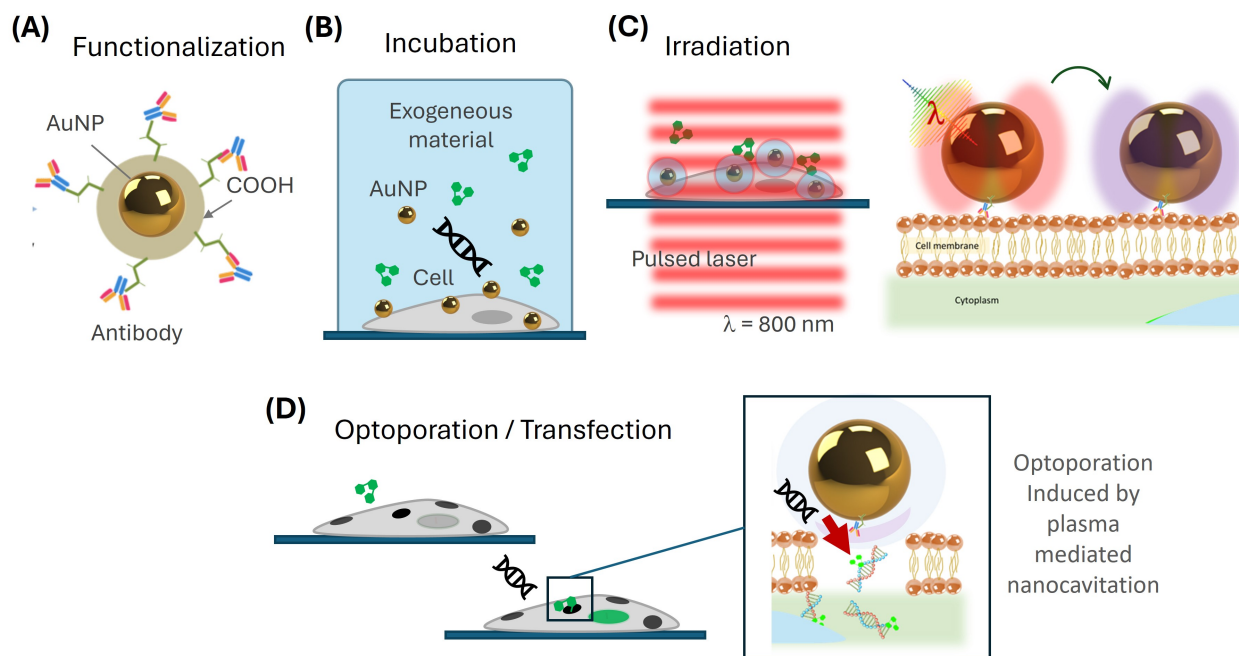


Figure 2.9 Optoporation and cell transfection steps: **(A)** NP functionalization is followed by **(B)** incubation of NPs with the exogenous material in the cell medium. Subsequently, **(C)** laser irradiation is performed to achieve **(D)** optoporation and consequently transfection if genes are delivered inside the cells.

The mechanisms of internalization are still under discussion, some authors are referring to the diffusion of the agents or internalization due to resealing. When the membrane is disrupted, some inner layers are exposed to genes or drugs that can get attached. After the process of resealing, the cell takes itself the exogenous material into the cytoplasm and plasmids can adhere to the membrane and being translocated after a certain time [121]. Different studies have been done in several human and murine tissues, exploring the options of phototherapy in the regime of fs, ns, ps and CW for a wavelength range between UV – IR.

In terms of eye diseases, experiments have shown that it is possible to treat age-related macular degeneration implementing AuNPs to target specifically a layer in the retina; experiments were carried out *in vivo* showing that conjugated AuNPs toward the cell-surface voltage-gated K^+ channel subunit KV1.1 deliver siRNAs [106]. On the other hand, the treatment of retinoblastoma has been carried out by using AuNPs to kill cancerous cells with nanosecond and femtosecond lasers [123, 124].

Ocular neovascularization has been also studied implementing AuNPs, proving that the photoactivation of nanomaterials is a safe tool that can be implemented in cell surgery with a

low toxicity rate for certain concentrations of nanomaterials. [125]

Carbon NPs (CNPs) have been used for corneal treatment in combination with femtosecond lasers to deliver molecules with the aim to modify the characteristics of the CECs and increase their resistance to apoptosis. So far, the delivery of small molecules such as Calcein AM has been proved by Jumelle et al. [126], where human cornea explants were used to prove the optoporation and transfection, reaching a Calcein uptake of 54%.

When doing gene therapy assisted by inorganic material, the delivery path becomes critical to achieve the highest amount of vectors into the desired part of the body. Since eye drops are ineffective when delivering drugs or genes into the innermost part of the cornea or posterior chamber (retina), intravitreal and intracorneal injections are needed to reach different layers in the eye.

Such injections are common in clinics, nevertheless, in research, rodents, particularly mice, stand as the most prevalent mammalian models. Intracameral injections become challenging due to the anatomy and size of the mice, for this reason we have dedicated a chapter to the development of a protocol to achieve safer intracameral injections in rodents and a section summarizing current approaches and limitations.

2.4 Intracameral injections

Intracameral injection is a well-controlled procedure in clinics. The utility goes from surgical procedures such as pupil dilation, to anesthesia and administration of different drugs for the avoidance of inflammation after surgical procedures [127, 128].

Several eye diseases are first modeled in rodents since they provide a broad range of parameters for research [129, 130], including vast information regarding translation to clinical tests.

An example of this is gene therapy [131], where animal models are broadly used. There are some limitations regarding the dimension and anatomy of murine eyes [132, 133]. An illustration of this is the intracameral injection, where not only small volumes are required but also precision in the procedure must be increased since abrupt movements inside the AC might result in damaged tissue [134]. This procedure involves high risks such as iris damage, bleeding, leakage and wounds that can deteriorate the vision quality and as a consequence, affect the trustability and reproducibility of the research.

To better visualize the limitations related to the size and anatomy of the murine eye, a table including ocular metrics of mice and rabbits (the two species used in this thesis) is shown in Figure 2.10. The characteristics of the human eye are also included for reference.

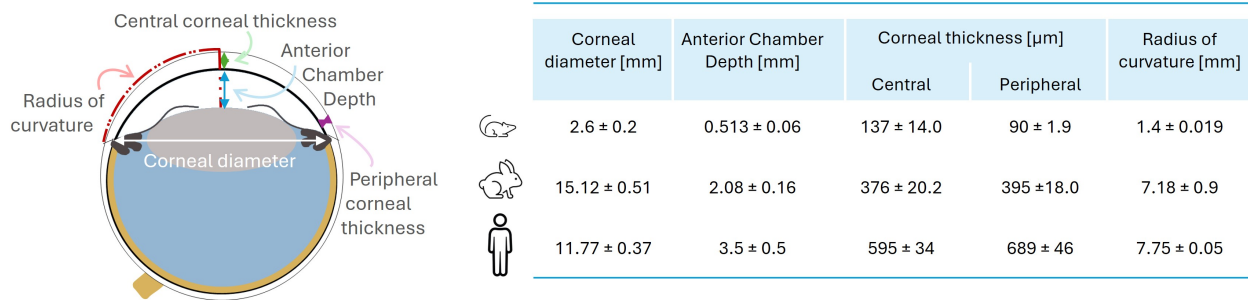


Figure 2.10 Ocular dimensions comparison between mouse [133, 135, 136], rabbit [137–139], and human. [18, 140, 141].

The reproducibility of the technique and the preservation of the different corneal layers is critical for the follow-up experiments, especially in the case of the CECs due to their non-dividing nature. While the anterior chamber depth (ACD) is about $513 \pm 65 \mu\text{m}$, the common needles used in clinics are nearly $260 \mu\text{m}$ in diameter [142] and the clear space for manipulation inside the AC is limited leading to problems related to the wounds produced by the needles. The main problems are leakage post-injection and thus collapsing of the AC, as well as bleeding and permanent damage to the lens or iris. For this reason, it is of utmost importance to implement a safe technique for intracameral injection in the murine model.

Several authors have tried distinct needle tip configurations to safely inject in ocular models as well as for diverse applications [143, 144]. The main studied parameters regarding the needles are their gauge (G), tip profile or number of bevels (needle faces), the bevels angle and the material as seen in Figure 2.11.

Reducing the size of the needle was shown to reduce pain and increase the chances of having a successful surgery [145]. For a successful injection, characterized by low penetration resistance and minimal tissue damage, a higher number of bevels on the needle tip is preferred. However, this design has limitations related to the rigidity of the material after tailoring the tip. According to different manufacturers, the ideal configuration is a pointed tip rather than a flat surface, as seen in single-bevel needles.

A pointy configuration can typically be achieved with a 3-bevel needle, which is commonly used in many studies. Depending on the wall thickness of the final needle, the number of bevels can be increased. Studies suggest that the axial force needed to pierce the cornea is lower when increasing the gauge needle. As an example, the force required to penetrate the central cornea using a 27 G needle is 0.61 N versus 0.29 N for a 31 G needle. The smaller the diameter of the needle, the lower the insertion force [148].

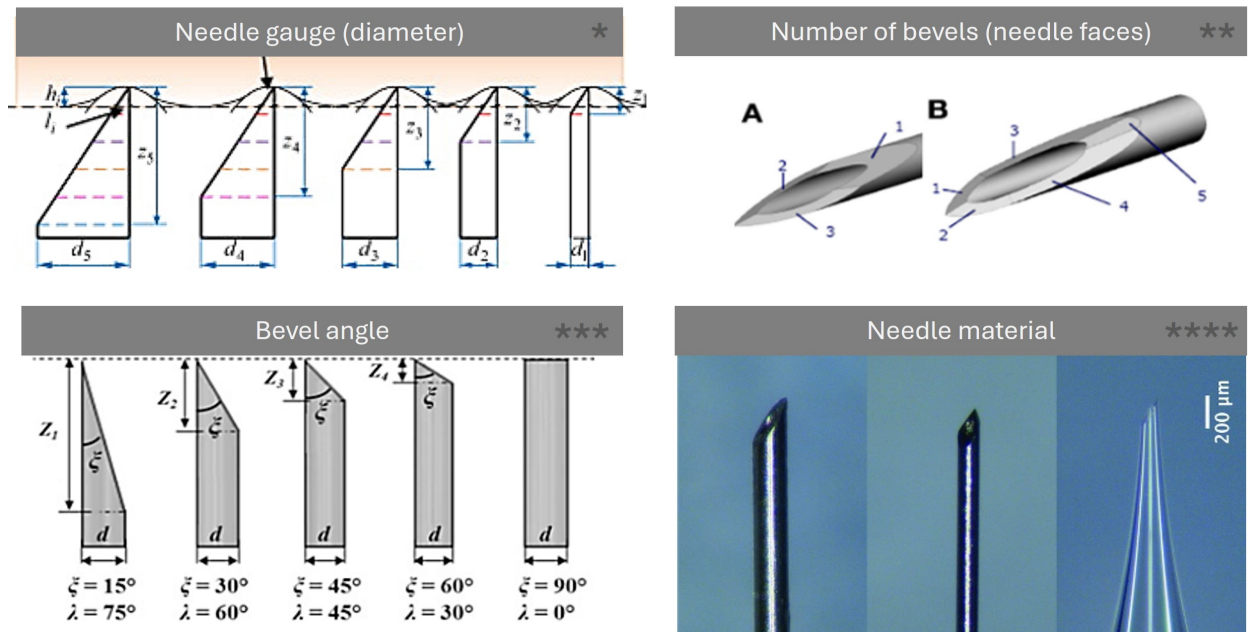


Figure 2.11 Different needle parameters reported in the literature. This image was adapted from different sources, the studies include piercings in diverse materials such as *PVA phantom, [145] **human skin, [146] ***agar gel, [147] and ****murine stromal cells [134].

On the other side, blunt needles are an alternative in some applications [149]. Researchers suggest that the use of blunt needles may reduce the incidence of hemorrhage in diverse tissues including the kidney, renal artery, spinal nerve among others. When compared with sharp needle punctures, results show in some cases that bleeding can be reduced by using blunt needles [150].

The mechanical properties of the corneal tissue do not allow for use of blunt needles. In this case, the piercing must be induced with a sharp tool before introducing the blunt needle (as explained in Chapter 4). For this specific application, the blunt tip of the needle helps prevent unwanted tissue tearing when inserted into the AC.

In some ophthalmic interventions, a paracentesis knife is used to create a self-sealing opening, allowing for the subsequent introduction of blunt needles. Examples of such procedures include fluid drainage for glaucoma [151], vitreoretinal surgeries, cataract surgeries [152], among others.

Furthermore, the utilization of established injection techniques is crucial for obtaining reliable and meaningful results. These techniques provide a solid foundation for advancing research and ensuring that findings can be effectively translated to *in vivo* systems and clinical applications.

In conclusion, this literature review has highlighted the eye as a sophisticated optical instrument and delved into the crucial role of the cornea and covered its associated dystrophies. Current clinical treatments and emerging alternative therapies, such as gene therapy and fs laser NP-mediated optoporation, offer promising advancements. Additionally, the exploration of intracameral injections underscores the ongoing innovations aimed at enhancing ocular health and treatment efficacy.

CHAPTER 3 *IN VITRO* FEMTOSECOND-LASER NANOPARTICLE ASSISTED INTERNALIZATION OF EXOMOLECULES

3.1 Introduction

Gene therapy approaches become more popular for inherited and non-inherited diseases as an alternative to current invasive procedures. Virus-based and mechanical treatments are currently studied using diverse delivery systems and vectors. The general objective of gene therapy is treating disorders by changing the genetic charge of cells. This can be done by internalizing attenuated versions of viruses or camouflaged vehicles into the cells. Nevertheless, possible toxicity due to mutations of the virus vectors is still a concern.

As part of this project, our emphasis lies in researching a virus-free treatment for corneal endothelial dystrophies, aiming to develop a less invasive technique that can readily transition into clinical applications. Laser technology has revolutionized various fields, including ophthalmology, by offering less invasive techniques [153, 154].

On this note, biological tissues, typically exhibit weak absorption of visible light, nevertheless, a tightly-focused laser pulse can induce nonlinear absorption within the tissue. Thinking on the potential implementation of lasers in ophthalmology treatments, the deposited energy on the tissues should not overpass the critical intensity threshold to prevent ablation due to non-linear phenomena.

One of the advantages of using laser beams lies in the fact that procedures are in general less invasive. Through the utilization of highly focused beams, we not only diminish invasiveness but also enhance treatment precision. This is achieved by directing a focused beam onto a specific layer of cells. The implementation of femtosecond lasers has been studied by different groups due to the possibility of creating low-density plasmas in transparent dielectrics. This property resulted advantageous when considering the low side effects in tissue [155]. At a single cell level, the changes in the membrane are pulse duration and repetition rate dependent [86].

On this note, the combination of lasers with diverse inorganic materials have been studied and proved to be efficient for drug delivery. An example of inorganic materials are the plasmonic nanoparticles (NPs), extensively used in different applications of cell surgery. The main motivation of using the plasmonic material relays in decreasing the laser energy and increase the resolution of the pores that can be produced in the membrane of the cell. By taking advantage of the high absorption of the plasmonic material, a local energy enhancement can

be achieved producing a disruption of the tissue. The selected material in this case is gold due to its biocompatibility. It is worth mentioning that the concept of biocompatibility strongly depends on the size and concentration of the particles in contact with the cells [156,157].

In previous studies conducted by our group and other researchers, the significance of spherical gold nanoparticles (AuNPs) size in plasmonic effects has been demonstrated [107,119,158,159]. For this specific investigation, off-resonance effects were targeted using AuNPs with a diameter of 100 nm. The concentration of AuNPs represents another crucial parameter that can be adjusted to optimize treatment efficacy by ensuring the appropriate number of particles per cell, thereby reducing the deposited energy in the cells.

The initial stage involved *in vitro* cell studies to assess optoporation efficiency and refine various physicochemical parameters. These parameters were drawn from literature sources. The optical setup utilized was based on a femtosecond laser with a central wavelength of 800 nm, coupled with a regenerative amplifier enabling a repetition rate of 1 kHz and a pulse width of 45 fs (Tsunami-SpectraPhysics).

Control over parameters such as scanning speed and laser fluence was facilitated by custom LabVIEW software, enabling precise irradiation under various treatment conditions. Parameter optimization was guided by assessments of internalized material efficacy and cell viability where fluorescence and reflected light microscopy were utilized.

The first stage of the treatment consists of the internalization of different small fluorescent molecules (e.g. PI and Calcein free-acid), which are membrane-impermeable dyes and work as an indicator of membrane perforation after irradiation. Subsequently, larger fluorescent molecules were evaluated for internalization such as Oligonucleotides (~ 16 kDa), and GFP plasmid DNA (pDNA - 10 kb). It is worth mentioning that the optimization of laser fluence was done with PI due to the quick fluorescence expression once cellular uptake is achieved. The reported uptake of PI helps determine the threshold fluence to be implemented when using larger molecules, working as a reference for future fine-tuning of the optical parameters and as a proof of the existence of an interaction between the NPs, the laser and the cell membrane.

The cell line utilized for preliminary testing was ARPE-19, a human adherent cell type that forms a stable monolayer and can be propagated for over 30 passages. The decision to use ARPE-19 for preliminary tests was influenced by both its accessibility in the laboratory and its superior adherence compared to corneal endothelial cells (CECs). Unlike many CECs available in the market, ARPE-19 cells exhibit robust adherence, eliminating the need for additional measures such as thin layers of organic components to prevent detachment during washing. The implementation of this cell line facilitated the establishment of the energy

deposition range, as well as the optimal fluorophore and nanoparticle concentrations. While it is well known that biological parameters and biomechanical properties vary across cell types, this ocular cell line proves useful for an initial parameter determination. However, it is essential to fine-tune these parameters when transitioning between different sample types (e.g., from *in vitro* to *ex vivo*) and across various cell or tissue types.

We report an internalization rate between 60-80 % for small fluorophores and <5 % for GFP pDNA (the largest tested molecule). The reported cell viability is 80 %.

3.2 Materials and methods

3.2.1 Plasmonic material

Colloidal AuNPs were purchased from NanoPartz (A11-100-CIT-DIH-1-50, Colorado, USA). Bare, PEGylated and functionalized AuNPs were tested to determine the optimal condition for homogeneous distribution. Subsequently, to obtain better performance at low fluence, the concentration of NPs was increased, testing low and high concentrations within the cell culture. The selected concentrations were 2×10^8 and 2×10^9 NPs/mL. This change in plasmonic material concentration was accompanied with a viability assessment to discard possible toxicity related to the high concentration of NPs.

The incubation of AuNPs with cells was performed during 24 hrs followed by PI (BMS500PI, ThermoFisher Scientific, Quebec, Canada) and Calcein AM (Invitrogen C3099, ThermoFisher Scientific, Quebec, Canada) assessment for cell viability. Fluorescent microscopy was implemented for cell identification and viability while bright-field microscopy was used as a tool to quantify the number of NPs per cell.

Once the toxicity test was performed, bare and functionalized AuNPs were compared to determine the optimal conditions for achieving a homogeneous distribution on the cells. This investigation aimed to identify conditions that prevent particle clustering, as clustered NPs tend to absorb and dissipate energy at higher rates. This elevated energy absorption can potentially lead to irreversible damage, resulting in increased cell death and undermining the precision of the technique.

Functionalization of NPs was performed under EDC-NHS standard protocol [160]. The selected antibody was Anti-CD44 (Hermes-1, MA4400, ThermoFisher Scientific). While CD44 is not the main marker expressed in CECs, it is involved in the regulation of essential cellular processes, including cell-cell and cell-matrix interactions [161].

3.2.2 Cells preparation

ARPE-19 cells (purchased from ATCC CRL-2302, Virginia, US) were cultured in DMEM supplemented with 10 % FBS and 1 % PS as recommended by the supplier. Three days before the laser treatment, cells were transferred to bottom-glass petri dishes (81218-200, Ibidi, Wisconsin, USA) achieving a confluence of 80-90 %.

Plasmonic NPs were incubated at different concentrations, followed by gentle stirring to ensure homogeneous distribution across all cells in the petri dish (Figure 3.1A). After one hour incubation, samples were washed with PBS (J60465.K2, ThermoFisher Scientific, Quebec, Canada) to remove excess non-attached NPs (Figure 3.1B).

The incubation time was determined taking into account the replacement rate of the aqueous humor *in vivo*, thus, considering that non-attached AuNPs will be washed out off of the eye within one hour. This consideration is particularly pertinent as the subsequent phase of this research will be conducted on the corneal tissue. This approach was considered to provide a more accurate assessment of the potential implications of the parameters in *ex vivo* experiments.

After washing the cells with PBS, the medium was replaced with phenol red-free reduced serum medium (Opti-MEM - 31985062, ThermoFisher Scientific, QC, Canada). By removing the phenol red of the culture medium, extra laser absorption is avoided.

Right before irradiation, the different solutions with exogenous molecules were added to the petri dish (see Figure 3.1C). Optimization of the working concentrations of all fluorophores was performed prior to the irradiation experiments within the range suggested by the suppliers. The optimal concentrations are shown in Table 3.1

Laser irradiation ($\lambda = 800$ nm @ 1 kHz) was performed at different fluence values in the presence of AuNPs and exogenous molecules for uptake evaluation and subsequent cell viability quantification (see Figure 3.1D). Due to the enhanced plasmonic effect, the cell membrane can be temporarily perforated. During this period when the pores are open, fluorophores present in the culture medium diffuse into the cell within minutes following the optoporation (Figure 3.1E) [162].

Membrane-impermeable fluorophores become visible after internalization through laser optoporation, either in the nuclei (e.g., PI and DAPI) or in the cytoplasm (e.g., Calcein free acid, Oligo-Cy3, and GFP pDNA) (Figure 3.1F).

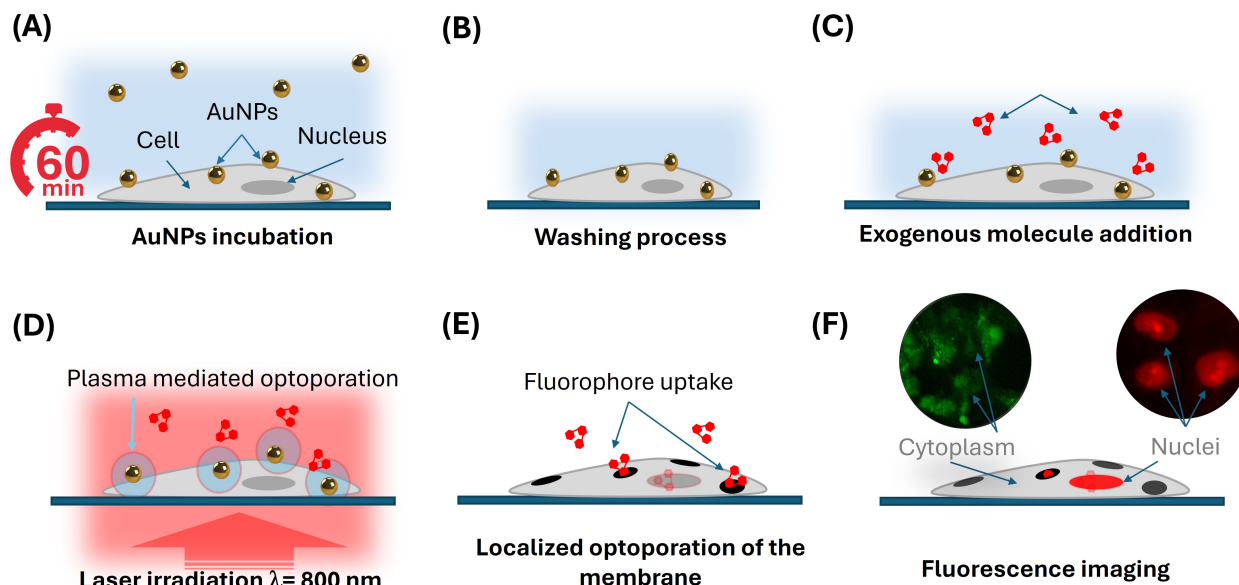


Figure 3.1 Protocol for *in vitro* optoporation treatment with ARPE-19 cells. **(A)** Incubation of AuNPs during 1 hour; **(B)** washing step to remove non-attached NPs; **(C)** membrane impermeable molecules added before irradiation; **(D)** irradiation with femtosecond laser centered at 800 nm for **(E)** localized optoporation and subsequent fluorophore uptake; **(F)** fluorescence expression can be from cytoplasm or nucleus depending on the type of exogenous molecule used.

3.2.3 Exogenous molecules

Diverse molecules were tested in order to determine the ease of internalization considering the molecular weight and as a consequence the size of the material versus the energy used controlling the size of the pore. Permeable membrane fluorophores were also used to identify the location plane of the cells in the petri dish such as DAPI that allows identifying the nucleus of individual cells with an emission wavelength in the blue. Fluorescent small molecules have been used to evaluate the optoporation process and fine-tune optical parameters, while large molecules serve as a tool to look for the threshold of energy that can be deposited in the cells before causing their death.

In the particular case of incubation with GFP pDNA, irradiation was performed in a 96-well plate containing 100 μ L of complete culture medium (Dulbecco's Modified Eagle Medium - DMEM) and 10 μ L of GFP pDNA (10 ng/mL). The optimal fluence was 150 mJ/cm² with a beam spot size estimated to be 100 μ m full width at half maximum (FWHM). It is important to note that visualization of GFP internalization should occur at least 20 hours post-laser irradiation, as this duration allows for the molecule to internalize and interact with

the cellular DNA.

Table 3.1 Exogenous molecules for evaluation of fs and AuNPs-assisted uptake in ARPE-19 cells.

Molecule name	Excitation/ emission wave- length [nm]	Molecular weight	Membrane perme- able (Y/N*)	Identification	Staining
4',6-diamidino-2-phenylindole (DAPI)	359/457	350.2	Y	Cell identification**	Nuclei
Calcein-AM	495/515	994.8	Y	Live cells	Cytoplasm
Calcein free acid	495/515	622.5	N	Optoporation	Cytoplasm
Propidium Iodide (PI)	535/617	668.4	N	Cellular death and optoporation	Nuclei
Cy3 Oligonucleotide	554/568	507.5	N	Optoporation	Cytoplasm
GFP pDNA	488/509	10 kb	N	Optoporation/ Transfection	Cytoplasm

* For the molecules noted as non-permeable, the optoporation needs to be done in order to internalize and visualize a change in fluorescence in the cell.

** At low concentrations, this can serve as an optoporation indicator.

All fluorophores were used following the supplier recommendations to avoid photobleaching, degradation and cell toxicity.

3.2.4 Optical setup

The optical setup, outlined schematically in Figure 3.2, incorporates an Nd:YAG (neodymium-doped yttrium aluminum garnet; Nd:Y₃Al₅O₁₂) pump laser for exciting the Ti:Sapphire laser, which generates femtosecond pulses at a high repetition rate of 76 MHz. These pulses are subsequently directed to a regenerative amplifier (RA), enabling the generation of short pulses (45 fs) at a reduced repetition rate of 1 kHz. The output from the RA is expanded and redirected toward the irradiation stage using metallic mirrors optimized for the central wavelength 800 nm.

The primary objective of the beam expander is to optically clean the beam and ensure

complete filling of the focusing element, resulting in an optimized focal point (highly focalized spot). This optimized focal point enhances resolution and specificity in treatment, minimizing side effects by reducing laser-induced damage to surrounding areas.

Control over the power reaching the sample is achieved using a rotating polarizer and a wave-plate. Power measurement is facilitated by customized software and a wedge mirror positioned after the rotating polarizer, allowing for power measurement via reflection of the main beam. A shutter, placed prior to the microscope's periscope, permits user interruption of irradiation, facilitating designation of specific treatment areas.

The selected fluence range for this study was 50 - 250 mJ/cm². In accordance with the literature, and foreseeing experiments in tissue, the suggested fluence range do not overpass the ablation threshold in cornea.

As focusing element, a 4x 0.1 NA microscope objective (Nikon) was used, estimating a beam spot of 50 μ m at 1/e². A translational stage (Prior Scientific) is used to precisely manipulate the position of the sample in the *x*, *y* and *z* directions. This stage allows for accurate and controlled movement following a serpentine pattern across the sample area (see Figure 3.2).

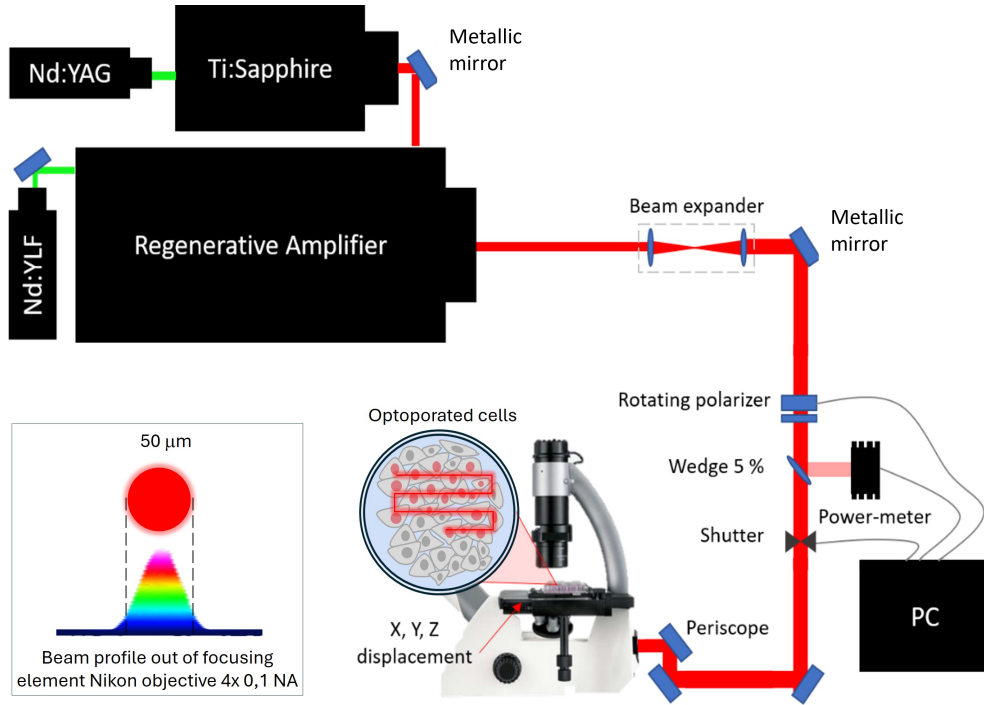


Figure 3.2 Optical setup for *in vitro* optoporation and imaging: the laser beam is directed to an inverted microscope for irradiation of samples *in vitro*.

3.3 Results

3.3.1 Plasmonic material

Reflected light microscopy images, combined with fluorescent images, were used to evaluate the optimal distribution of AuNPs in ARPE-19 cells. As shown in Figure 3.3A, a more homogeneous distribution was observed in samples with functionalized AuNPs. Additionally, the number of attached AuNPs increased compared to those with PEGylated material. Despite the anti-agglomerative properties of PEG on NPs, the aggregation observed with PEGylated NPs could potentially arise from interactions involving long or densely packed PEG chains on the nanoparticle surface. Additionally, local pH changes at the cell membrane and the salinity of the medium where the NPs are injected may contribute to this phenomenon. Further studies exploring the effects of varying PEG chain lengths on NP chemistry could provide valuable insights into these interactions at the cell membrane. It is noteworthy that a higher number of AuNPs results in a lower energy requirement for optoporation. In this study, minimizing energy is crucial to avoid side effects such as cell death.

After determining that antibody-coated AuNPs were the optimal choice, two concentrations of functionalized AuNPs were tested. The main parameters evaluated were distribution and toxicity. Calcein-AM staining was used to quantify cell death. As shown in Figure 3.3B-C, no significant toxicity differences were found between the tested concentrations, making distribution the deciding factor for selecting the concentration.

As mentioned earlier, a higher number of NPs per cell can lead to a lower irradiation value. Therefore, the ideal scenario is to have the maximum amount of plasmonic material for optoporation. Based on these results, the optimal conditions for subsequent steps are using CD44-AuNPs at concentration of 2×10^9 NPs/mL.

It can be observed that the standard deviation associated to the number of NPs per cell is significantly high. This phenomenon can be associated to the protein expression in the cellular membrane. Immunostaining data found in literature, shows a similar non-homogeneous expression behavior of CD44.

3.3.2 Internalization and cell viability rates *in vitro*

As initial step, nucleus identification was performed using DAPI staining (blue fluorescence). The software ImageJ was used for background subtraction to standardize the images prior to nucleus quantification. The 3D Object Counter plugin was then utilized for image analysis [163], determining the number of cells per image.

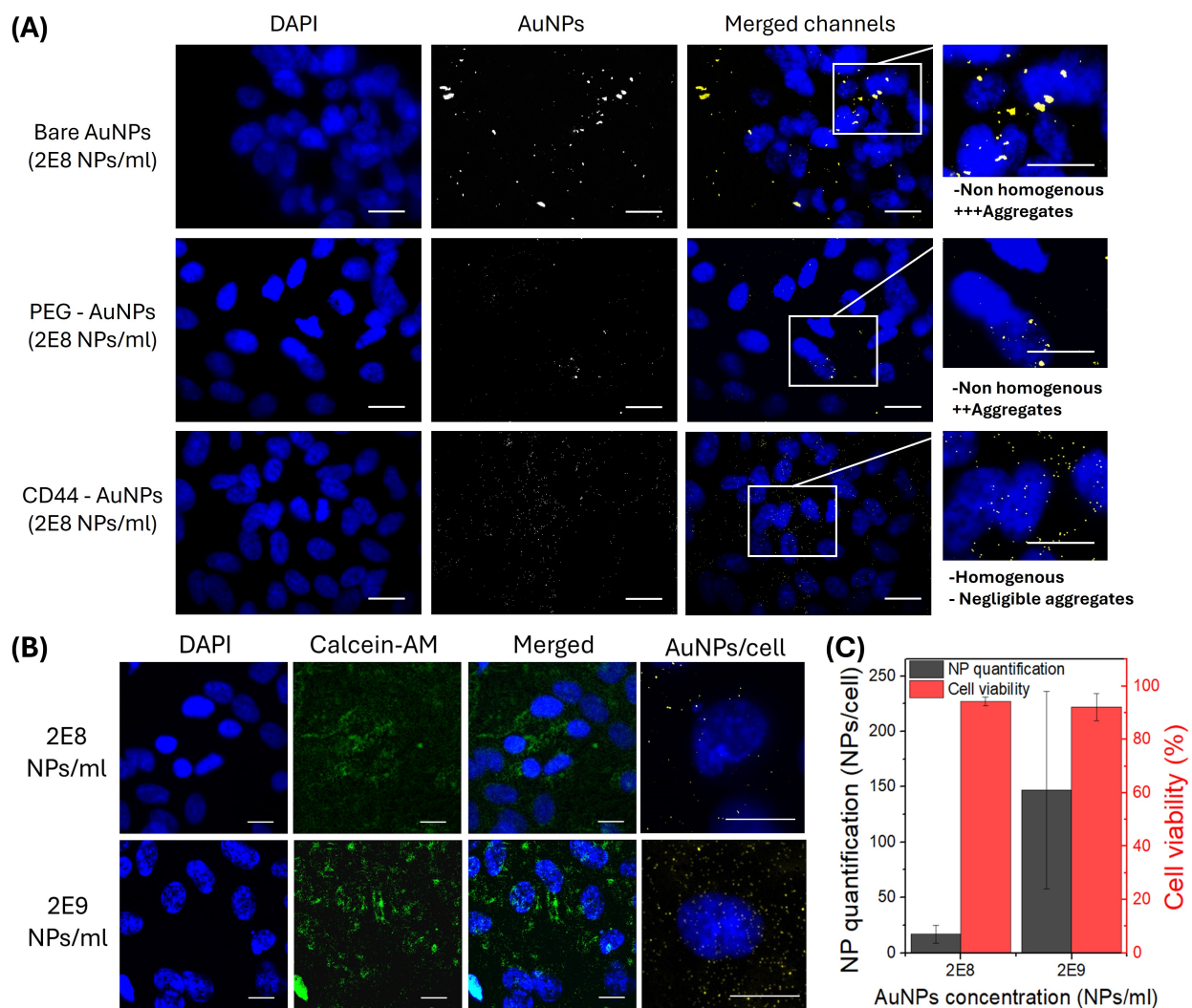


Figure 3.3 NP assessment for optoporation optimization. **(A)** Bare-, PEG- and antibody conjugated-AuNPs assessment for distribution visualization. **(B)** Viability assessment for two different concentrations of AuNPs with its corresponding **(C)** quantification of NPs/cell. The scale bar corresponds to 20 μm for all images.

For optoporation and transfection quantification, fluorescence images from either PI or Cy3-oligonucleotide (red) and from GFP pDNA (green) were captured both before and after irradiation to evaluate the efficacy of the laser treatment.

To calculate the optoporation rate, images were taken one hour post-irradiation. In the case of GFP pDNA, the images were taken 20 hours after the irradiation to allow molecules to bond with cellular DNA. The efficacy was determined by dividing the number of cells expressing fluorescence post-irradiation by the total number of cells indicated by blue fluorescence (DAPI).

For uptake tests performed with either PI and Cy3-oligonucleotide, cell viability was tested using Calcein-AM 24 hours after irradiation. The viability rate was determined by quantifying the number of cells expressing green fluorescence versus the total number of cells (DAPI) inside the irradiated area. The samples were incubated at 37°C within an atmosphere of 5 % CO₂ as suggested by the technical data sheet.

As a quick assessment, PI was used to evaluate the fluence range and determine the optimal value for subsequent uptake assay with Oligo-Cy3, Calcein acid free and GFP pDNA. Results of the study performed at different fluences are illustrated in Figure 3.4. High viability was observed for irradiation performed at 50 and 100 mJ/cm², reporting 95 ±5% and 91 ±3% (mean ±SD) respectively. Subsequently, viability values were lower while increasing the fluence. Cell damage and detachment was observed after irradiation.

As seen in Figure 3.4, for irradiation assay performed at 200 mJ/cm² some cells were damaged at the border of the irradiation area. This might be attributed to mechanical factors. Due to dwell time of the translational stage when changing direction, the irradiation exposure time is slightly higher at the borders of the sample, thus increasing the energy delivered into the sample. Tests performed at 250 mJ/cm² resulted highly lethal for ARPE-19 cells reporting close to 95 % detachment after irradiation.

On the other side, cell viability was also assessed using Calcein-AM. Figure 3.5A illustrates the tendency of optoporation and viability versus fluence. It is observed that the optimal value to achieve high optoporation rate with low cellular death corresponds to 150 mJ/cm². It is worth mentioning that even though, optoporation rate resulted higher at 200 mJ/cm², the viability seems compromised. Thus, to offer a safe treatment with negligible phototoxicity, further tests of exogenous molecule uptake and controls were performed at 150 mJ/cm². Figure 3.5B illustrates the group controls to confirm that PI uptake is entirely due to the combination of AuNPs and laser irradiation.

It is worth noting that PI staining can be used both for visualizing optoporation and iden-

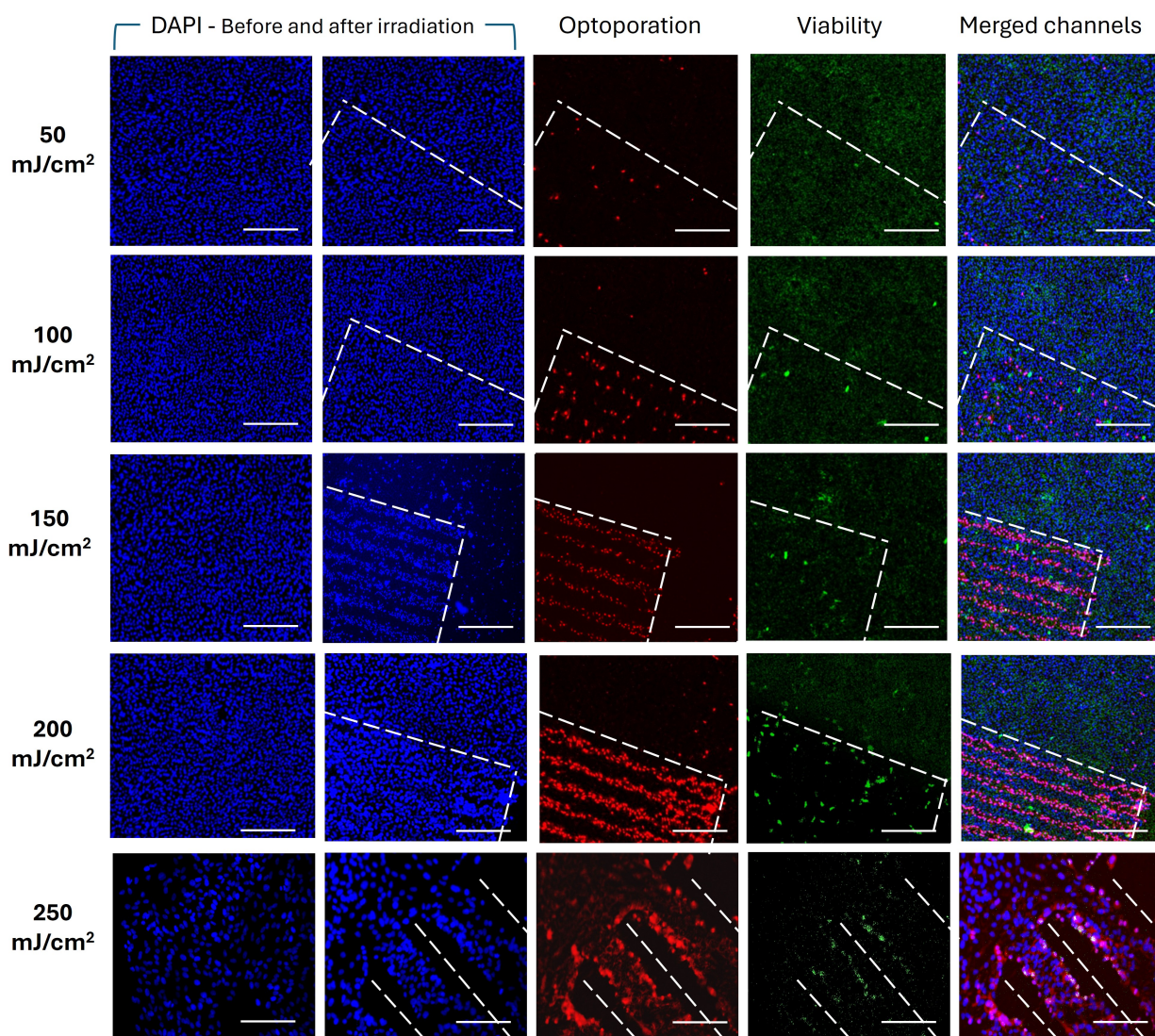


Figure 3.4 Fluence assessment for optoporation optimization. DAPI columns show the cells before and after irradiation (blue). Optoporation assessment shows the fluorescence of PI (red) while viability images correspond to Calcein-AM 24 hours after irradiation (green). Dotted lines depict the irradiation area. The scale bar corresponds to 200 µm for all images.

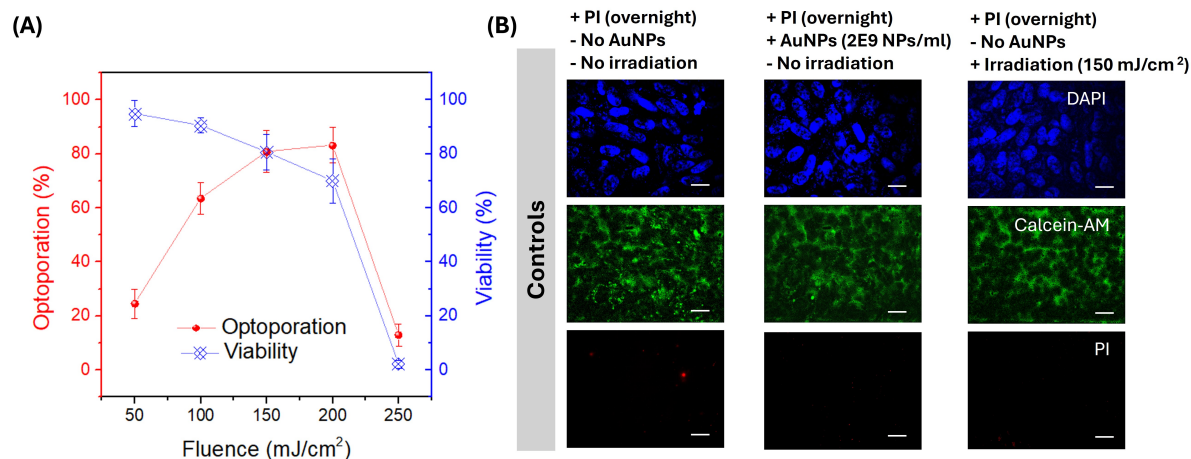


Figure 3.5 Optoporation and viability tendencies for *in vitro* assessment. **(A)** Quantification of the optoporation percentage versus viability for a fluence range of 50 to 250 mJ/cm²; **(B)** control groups showing no toxicity from PI (column 1), no toxicity of AuNPs (column 2), and no phototoxicity associated to the laser (column 3). The scale bar corresponds to 20 μ m for all images.

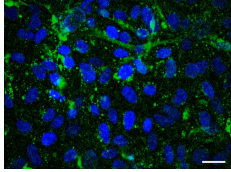
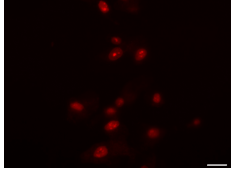
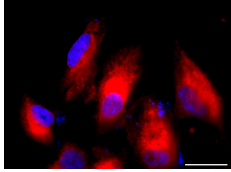
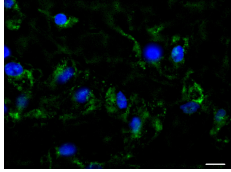
tifying dead cells. Differentiating between these conditions depends on the concentration of PI and the timing of its addition to the samples. For optoporation assessment, PI can be incubated with the cells immediately before laser irradiation at a concentration of 1 μ g/mL, followed by a washing step prior to imaging. For viability assessment, PI should be added well after the laser treatment (a 24 hours period was used for this study) to allow the cells time for membrane recovery; in this case, a concentration of 2 μ g/mL is recommended [164].

The perforated membrane can be recovered by self sealing the pores generated from the irradiation of the NPs with the laser naturally [99,121]. To obtain better performance at low fluence, the concentration of NPs was increased keeping a well-distribution of AuNPs on the cell membrane (higher number of well-distributed NPs per cell). This change in NPs concentration was accompanied by a viability test to discard possible toxicity related to the high concentration of the plasmonic materials in the cell culture.

Based on our study, 60-80 % internalization efficacy was reached with the small molecules, including PI, Oligo and Calcein acid-free. On the other side, when using larger molecules such as GFP pDNA the reported uptake is <5 %.

A summary of the internalization achieved for each tested exogenous molecule can be observed in Table 3.2.

Table 3.2 Uptake percentage of exogenous molecules in ARPE-19 cells using fs and AuNPs-assisted optoporation. The scale bar corresponds to 20 μm for all images.

Molecule name	Approximate size [nm]	Uptake [%] mean \pm SD	Fluorescence imaging
Calcein free-acid	< 1	70 \pm 5	
PI	< 1	81 \pm 8	
Cy3-Oligonucleotide	\sim 1.5	60 \pm 5	
GFP pDNA	\sim 4	4 \pm 1	

3.4 Conclusion and discussion

In this study, we evaluated the distribution and effectiveness of functionalized AuNPs in ARPE-19 cells using a combination of reflected light microscopy and fluorescent imaging. Our findings indicated that functionalized NPs provided a more homogeneous distribution and a higher number of attached NPs compared to PEGylated materials. This higher density of NPs was associated with a reduced energy requirement for optoporation, minimizing potential side effects such as cellular death. The variability in nanoparticle distribution is likely influenced by the heterogeneous expression of membrane proteins such as CD44.

Calcein-AM staining revealed no significant toxicity differences between the tested concentrations, leading us to prioritize nanoparticle distribution in our selection. Although Calcein-AM is membrane-permeable, a slight photobleaching was observed in optoporated cells, consistent with existing literature. Therefore, it is recommended to perform Calcein-AM viability tests at least 12 hours post-optoporation to allow for membrane recovery.

This study highlights the dual functionality of PI staining for both visualizing optoporation

and identifying dead cells. The differentiation between these conditions is achieved by adjusting the concentration of PI and the timing of its addition to the samples. For optoporation assessment, incubating cells with PI at a concentration of 1 $\mu\text{g}/\text{mL}$ immediately before laser irradiation, followed by a washing step, proved effective.

For assessing cell viability, adding PI at a concentration of 2 $\mu\text{g}/\text{mL}$ after a 24-hour recovery period post-laser treatment allowed for accurate identification of dead cells. These findings underscore the importance of protocol optimization in experimental setups to accurately assess cellular responses and ensure the reliability of the results. It is worth mentioning that PI might result toxic in high concentrations for some cells or tissues. For this reason, in subsequent chapters where corneal tissue is used, the implementation of PI is limited to preliminary results.

Results indicate that high cell viability was maintained at low irradiation levels of 50 - 150 mJ/cm^2 , with $95 \pm 5\%$ and $91 \pm 3\%$ viability, respectively. However, as the fluence increased, cell viability decreased, with noticeable cell damage and detachment observed. Especially in the case of irradiation values of 200 and 250 mJ/cm^2 .

It was possible to observe in samples with high fluence that some cells were damaged at the borders of the irradiation area, likely due to increased exposure time from mechanical factors of the translation stage. This irradiation condition was highly lethal, resulting in cell detachment. These findings highlight the importance of carefully optimizing fluence levels to balance effective uptake with minimal cellular damage.

In this study, the optimal combination of parameters for achieving high uptake with negligible cellular death was identified as using a fs laser centered at 800 nm, with a repetition rate of 1 kHz and a pulse duration of approximately 45 fs, to irradiate ARPE-19 cells at 150 mJ/cm^2 , decorated with AuNPs at a concentration of 2×10^9 NPs/mL.

Additionally, for future studies involving tissue, a circular irradiation pattern is recommended to prevent abrupt direction changes at the borders of irradiated areas, which can compromise cell viability.

In our study, we observed that internalizing small molecules, approximately 1 nm in size, was significantly easier, resulting in higher uptake compared to larger molecules around 4 nm. This difference is likely due to the membrane pores, which may not be sufficiently large to accommodate bigger molecules. However, creating larger pores poses a risk of cellular death. Therefore, while small molecules are efficiently internalized, optimization strategies for larger molecules must carefully balance the need for effective uptake with the preservation of cell viability. These optimization strategies for larger molecules are further explored in corneal

tissue in Chapter 5.

In vitro experiments provide valuable insights into the parameters and potential optimizations for improving molecule uptake. These experiments offer a controlled environment to evaluate various factors and make preliminary adjustments. However, it is important to recognize that *in vitro* models, which typically involve cell monolayers, do not fully capture the complexity of *ex vivo* or *in vivo* samples. In actual tissues, numerous additional parameters, ligands, and biological components interact to maintain tissue integrity.

Consequently, while studies presented in this chapter are essential for initial assessments, slight optimizations were necessary to account for the more complex environment encountered in tissue studies. This highlights the importance of complementing *in vitro* findings with *ex vivo* studies to achieve comprehensive and effective optimization of molecular delivery systems.

One of the changes implemented for *ex vivo* experiments is transitioning from the use of pDNA to mRNA. As suggested by the literature, mRNA is considered safer due to reduced risk of mutagenesis. This shift anticipates adjustments in the fluence range to accommodate the larger molecule size of mRNA.

Typically, mRNA molecules are about 1,000 to 3,000 nucleotides long, with each nucleotide being approximately 0.34 nm in length. This results in an average mRNA molecule length ranging from roughly 340 nm to 1,020 nm. However, the actual size in terms of molecular dimensions is more complex due to the three-dimensional structure and folding of the mRNA. When considering the overall folded size, an mRNA molecule can have a diameter of about 10-30 nm, depending on its secondary structure and interactions with other molecules [59,60].

For this reason, the following chapters of this thesis are dedicated to the study of different parameters for *ex vivo* transfection in corneal tissue.

CHAPTER 4 ARTICLE 1: OPTIMIZATION OF INTRACAMERAL INJECTIONS IN THE MOUSE EYE MODEL

This article submitted to the journal Translational Vision Science & Technology (*TVST*) from the Association for Research Vision and Ophthalmology (ARVO) on October 24th 2024, corresponds to the first part of the animal experimentation where two injection techniques were studied to improve the subsequent nanoparticle delivery into the anterior chamber of murine models. Authors: Jennyfer Zapata-Farfan,^{1,2} Alex de Oliveira Coronel Camacho,^{2,3} Marilyse Piché,² Alexandre Abid,³ Michel Meunier,^{1,2} Christos Boutopoulos,^{2,3} Isabelle Brunette.^{2,3}

¹ Engineering Physics Department, Polytechnique Montreal, Montreal, QC, Canada;

² Maisonneuve-Rosemont Hospital Research Center, Montreal, QC, Canada; ³ Department of Ophthalmology, Université de Montréal, Montreal, QC, Canada.

The author of this thesis and first author of the paper, Jennyfer Zapata-Farfan, performed the injections, improved the needle tip by laser micromachining, and developed 3D models to improve the animal stability while performing the injections. Alex Camacho contributed with the preparation of the second injection technique performing initial injections. Marilyse Piché assisted with the animal manipulation, Alexander Abid helped with the preparation of the OCT installation. Michel Meunier, Christos Boutopoulos and Isabelle Brunette participated in the discussions.

4.1 Abstract

Intracameral injections in mice are challenging due to eye dimension and anatomy. We present an optimized setup and two different techniques for anterior chamber injections with improved safety, precision and reproducibility.

A semiautomatic setup with real-time monitoring was developed using an optical coherent tomograph, a color camera, a motorized manipulator, and 3D-printed pieces to safely immobilize the mice. A series of needles (31-36 G), laser-machined tip profiles (30° and 15°), corneal puncture sites, and needle orientations were tested. We developed two injection techniques, with a sharp and a blunt needle through a self-sealing corneal microincision. Eighty eyes of 49 C57BL/6 mice (43 *ex vivo* and 6 *in vivo*) were used to validate results following ethical protocol approval.

The highest performance achieved with sharp needles in terms of efficacy and safety was obtained with custom tri-surface 15° 35 G laser-sharpened needles, injecting at the iridocorneal angle, parallel to the limbus, allowing piercing in 83% of cases with average tissue damage rate of 8%. Injections using a blunt needle through a self-sealing corneal incision yielded successful piercing in 94% of the cases, with average tissue damage of 11%.

We optimized two intracameral injection approaches with increased precision, reproducibility and safety. Along with 3D-printed pieces specially adapted for head and eye support, we offer an optimized approach for researchers performing anterior chamber injections, offering more reliable and consistent results in mouse eye research. Our techniques can be applied to research in anterior chamber gene therapy and drug delivery, providing safe and reproducible results.

4.2 Introduction

Mice are favored models in medical research and vision and ophthalmology studies are no exception. Several eye diseases are modeled in mice due to the broad range of parameters available for research, [129, 130, 165, 166] as well as their accessibility and ease of handling. However, studies requiring intraocular injections for the development of drugs or gene therapies face technical challenges due to the small size of the eye and the large volume occupied by the lens. [132, 167, 168] While injection in the anterior chamber (AC) is a well-controlled procedure in human subjects, [169–171] AC injections in the mouse eye require special additional precision to penetrate the narrowness of the AC (mean maximum depth of $470 \pm 80 \mu\text{m}$) while following the steep curvature of both the anterior surface of the lens and the posterior surface of the cornea. The risk of damaging the iris and lens and causing bleeding, inflammation and scarring are therefore very high. The corneal endothelium must also be protected, as this monolayer of non-dividing cells is of paramount importance in maintaining corneal transparency. Any disorganization of the anatomy of the anterior segment of the eye must be avoided as it irreversibly affects not only visual function, but also the reliability and repeatability of the experiment. Intracameral injections in the mouse model require smooth injection of small and precise volumes. [134] Additionally, the simple needle puncture of the thin mouse cornea (the thickness of the peripheral cornea is in the order of $90 \mu\text{m}$ [133]) results in a high incidence of wound leakage, which significantly complicates control of the volume and concentration of injected solutions and increases the risk for collapsing the AC. For all these reasons, it is of utmost importance to implement a safe and efficient methodology for successful intracameral injection in the murine model.

In this work, experiments were performed in order to determine the optimal conditions for

intracameral injections in the mouse model, using the best combination of a series of needle parameters and injection locations and orientations. Injections were assisted by simultaneous optical coherent tomography (OCT) and color camera monitoring. A 3D motorized manipulator and 3D-printed custom-designed pieces were used to ensure stability of the mouse. Two injection techniques were developed, one with sharp needles and one with blunt needles, both of which could easily be implemented in the laboratory to improve the safety, quality and repeatability of AC injections in the murine model.

4.3 Materials and Methods

All experiments were approved by local animal protection committees in accordance with the ARVO Statement for the Use of Animals in Ophthalmic and Vision Research and guidelines of the Canadian Council on Animal Care.

4.3.1 Conception of a 3D holder and assembly for the mouse experiments

The essential step before starting the experiments was to develop a set-up that would stabilize the mouse safely and effectively during the injections. The animal's lack of tone during general anesthesia, the high mobility of the globe at the slightest pressure, and the repetitive movements generated by the animal's breathing necessitated the development of a 3D-printed plate custom-designed to hold the mouse and optimize positioning of the head, as well as a 3D-printed custom-designed eye holder to stabilize the globe, facilitate access to the cornea and improve visualization of the AC during injection.

4.3.2 Optical coherent tomography visualization

As a monitoring technique, we used an OCT (OQ LabScope 2.0, Lumedica, NC, USA) with a central wavelength of 840 nm and an A-scan line rate of 13 kHz. Real-time images were used to align the needle with the AC and improve the injection by centring the needle tip away from the lens, iris, and corneal endothelium.

4.3.3 Injection with a sharp needle puncture

Needle orientation. Commercially available 31 G sharp needles (320440, Becton, Dickinson and Company, NJ, USA), which are the thinnest needles commonly used in the eye clinic, were first used to test two different angles of injection, i.e., perpendicular (Figure 4.1A) or parallel (Figure 4.1B) to the corneal surface at the level of the peripheral cornea. Recorded

videos of simultaneous OCT and color camera monitoring were used to analyze the impact of needle orientation. Outcome parameters included changes in AC depth (to assess volume retention or AC collapse), lens capsule perforation, iris damage, and bleeding.

Needle size. As a second step, 33 to 36 G needles (NanoFil needles, WPI, FL, USA) were tested with the best orientation obtained from the previous step. The above-mentioned outcome parameters, AC depth, lens capsule perforation, iris damage and bleeding were used to determine the best needle diameter to be used in subsequent steps.

Needle tip main bevel angle. Needle tips with a narrower main bevel angle were then tested in order to compare the commercial specifications against the 15° proposed herein (Figure 4.1C). To our knowledge, the smallest commercially available angle for the main bevel of the 35 G is 30°. In order to reduce the number of wasted needles and to try a narrower bevel angle, the needles were laser-machined and resharpener after each use. The micromachining was made in our laboratory with a femtosecond laser centred at 800 nm, with a repetition rate of 1 kHz (Hurricane, Spectra-Physics, CA, USA).

Needle tip secondary bevels. Subsequently, modifications in the number of bevels (1 and 3) have been made to commercial needles that resulted from the best previous set of experiments, as can be seen in Figures 4.1D and E. The needles were laser-machined to change the main angle and the number of bevels. The best tip geometry for the sharp needle was determined based on the outcome parameters previously described.

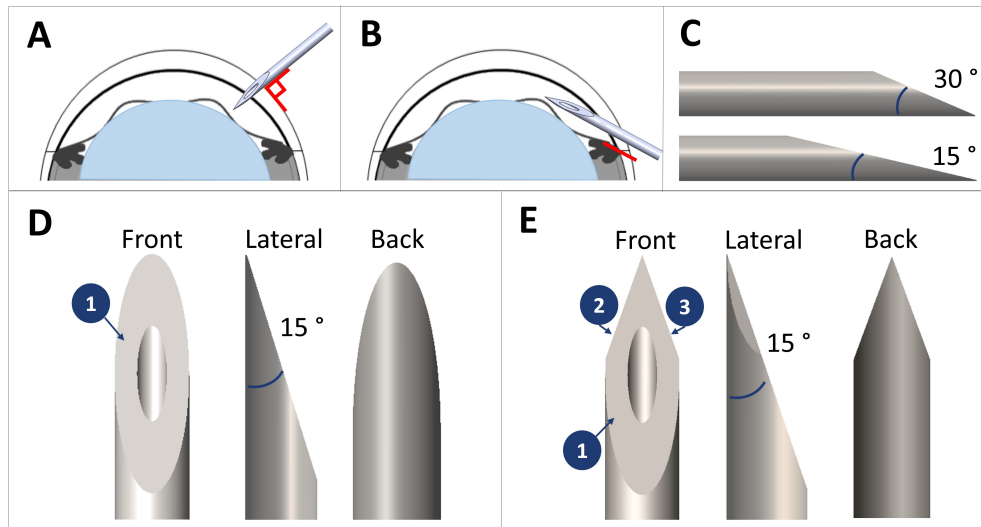


Figure 4.1 Different configurations of injection and needle profiles. (A) Perpendicular and (B) parallel injections with respect to the corneal surface. (C) Two different angles for the main bevel of the needles. Comparison of the needle tip geometry with (D) one and (E) three bevels.

Motorized micromanipulator and setup. Needles mounted on 10 μL syringes (SGE010RNS, NanoFil syringe, WPI, FL, USA) were installed on a 4-axis motorized micromanipulator (QUAD, Shutter Instrument Company Novato, CA, USA) to increase stability and repeatability of the injections and avoid the imprecision and variability of manual manipulations. A 4 mm diameter hole was punched (33-34, biopsy punch, Miltex Instruments, Integra Life-Sciences, NJ, USA) in an adhesive transparent film dressing (1624W, Tegaderm, 3M, MN, USA) that was then applied to the periocular region to gently protrude the ocular globe of the mouse and improve access to the anterior chamber (detailed information can be found in Figure A.1 of Appendix A). The speed of the needle was limited to a maximum of 3 mm/s. For visualization purposes, 0.5 μL of OCT contrast agent (LB3-1ML, Latex beads, polystyrene 0.3 μm ; Sigma Aldrich, MO, USA) was injected into each eye. Figure A.2 of Appendix A shows the setup used for injections using the sharp needles.

4.3.4 Injection with a blunt needle through a corneal incision

For the second injection technique, a corneal incision was made prior to the injection and a blunt needle was used. McPherson forceps (TMF511, Titan Medical Inc, Toronto, ON, Canada) were used to gently stabilize the eye at the level of the equator while initiating a one-plane corneal incision, oblique with respect to corneal surface, using a 1 mm dual bevel paracentesis knife (8065921540, ClearCut, Alcon Laboratories Inc. Forth Worth, Texas, USA). In this case, the McPherson forceps were preferred over the eye holder, because penetrating the AC with a knife requires a rapid although controlled release of the intraocular pressure to avoid wound leakage, and this was more easily achieved with the forceps than with the eye holder. The blade was barely entered in the AC, aiming at a <1 mm wide incision on the inner side of the cornea. This oblique incision profile resulted in a clean and flat corneal wound, typically self-sealing due to the apposition of the posterior flap to the anterior flap, which was maintained by the intraocular pressure. The paracentesis knife was stained with a surgical marker (250GPR, Cardinal Health Regular-Tip Skin Marker w/6", OH, USA) before the incision to ease the localization of the wound at the time of injection.

A blunt microneedle mounted on the injection syringe was then applied perpendicular to the corneal incision surface and the smooth outflow generated during the injection was enough to reopen the stromal tunnel and inject through the corneal incision. The gauge of the blunt microneedle was selected from the studies described above (35 G). The injections were carried out under a stereo microscope, introducing a volume of 0.5 - 1 μL of balanced salt solution (BSS) (65079550, Alcon, Mississauga, ON, Canada) stained with fluorescein (G1197, Fluorescein sodium ophthalmic strips USP, FluoStrips) for better visualization of

the AC expansion during the injection. After injection, the excess fluid was gently wiped from the corneal surface using a surgical sponge (40410, cellulose eye spear, Beaver-Visitec International, Inc., MA, USA) and the wound watertightness was checked using a blue filter. For this injection technique, no OCT monitoring was needed to drive the procedure, as making the corneal incision was easier under direct visualization and because there was no need to penetrate the AC with the blunt needle tip. Nevertheless, images of the AC before and after the injection were taken to measure the AC depth and confirm the integrity of the ocular structures after the procedure.

4.3.5 Mouse preparation for *ex vivo* and *in vivo* experiments

A total of 80 eyes from 49 C57BL/6 adult mice were used for this study, 43 mice for the initial *ex vivo* experiments and 6 for the *in vivo* validation. *Ex vivo* experiments were performed within minutes following lethal intraperitoneal injection of pentobarbital sodium (40 mg/kg). *In vivo* experiments were performed under general anesthesia following intraperitoneal injections of ketamine (60 mg/kg) and medetomidine (1 mg/kg), and a heating pad was used to maintain mice temperature at 37°C during anesthesia. An ophthalmic gel (Refresh Optive, Allergan Inc. DUB, Ireland) was applied on all eyes to avoid ocular dryness. Right before injection, the lashes and whiskers of the animal were trimmed to clear the injection site and the eye was gently washed out with BSS to optimize visibility.

4.3.6 Outcome parameters

A series of qualitative and quantitative parameters were selected in order to develop a successful, safer and more reproducible procedure for intracameral injection. The simultaneous live OCT and color camera monitoring (Figure 4.2A) allowed to assess the corneal surface damage induced by the needle (Figure 4.2B), as well as the capacity of the needle to enter the AC, from which was calculated the percentage of piercing (number of pierced corneas / total number of attempts; one attempt per eye). Damage to the iris (Figure 4.2C) and/or lens capsule (Figure 4.2D), bleeding appearing as a turbid fluid filling the AC (Figure 4.2E), and wound leakage (Figure 4.2F) were the four complications used to calculate the complication rate (number of complications observed per eye per studied group). OCT measurements of the AC depth before and after the injection were used to document the stability of the procedure. The tissue damage was also estimated by counting the number of partially or totally collapsed AC. In order to compare the damage created by large vs. small gauge needles, the eyes of representative euthanized animals were enucleated using fine curved forceps (UZ-07387-12, Cole-Parmer, IL, USA) to gently protrude the globe and sever the optic

nerve. Corneas were dissected (E3386 Vannas scissors, Storz Instruments, Bausch + Lomb, NY, USA), stained with 10% trypan blue for 2 minutes, gently rinsed x2 with BSS, and fixed in PFA 4% for 10 minutes. Trypan blue is a selective stain that penetrates only dead cells. Light microscopy of the corneal endothelial surface was then performed on flat mounts prepared by making four peripheral radial cuts in each cornea (30° stab micro-blade, 7530, Ambler surgical, PA, USA).

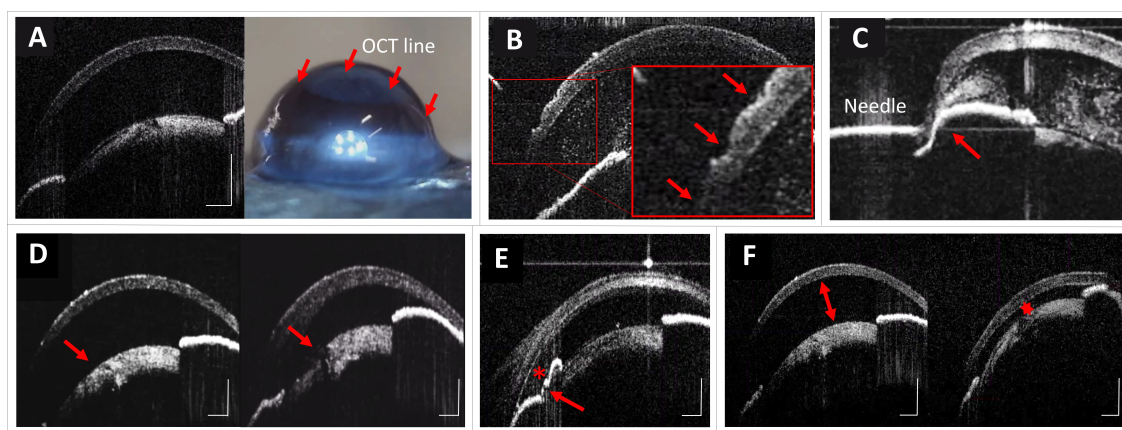


Figure 4.2 Examples of the evaluation of ocular damage caused by intracameral injections. (A) Simultaneous monitoring of a mouse eye with OCT (left) and color camera (right; arrows show the line of the OCT that generated the image on the left). (B) Corneal surface damage produced by an unsharpened needle tip (arrows). (C) Corneal deformation and iris damage during failed injection. The arrow shows the iris being pushed by the needle. (D) Visualization of a damaged lens, comparison before (left, the arrow shows no damage) and after injection (right, the arrow shows the rupture of the lens). (E) The arrow shows a damaged iris, while the asterisk shows the bleeding in the AC, visualized as a turbid shadow around the damaged iris. (F) AC depth comparison before (left; double-headed arrow) and after (right; star) injection showing corneal collapse due to wound leakage. The scale bar corresponds to 500 μm for all images.

4.4 Results

4.4.1 Stabilization of the mouse, the eye and the syringe

The 3D-printed plate custom-designed to hold the mouse during manipulations has significantly facilitated the positioning of the mouse head, improving access to the cornea and visualization of the AC under the OCT during injection (Figure 4.3A). The 3D-printed custom-designed eye holder also added stability during piercing of the cornea (Figure 4.3B). CAD files can be obtained upon request, for their reproduction and implementation in similar

procedures in the mouse model, otherwise, the design can be rescaled for different animal species.

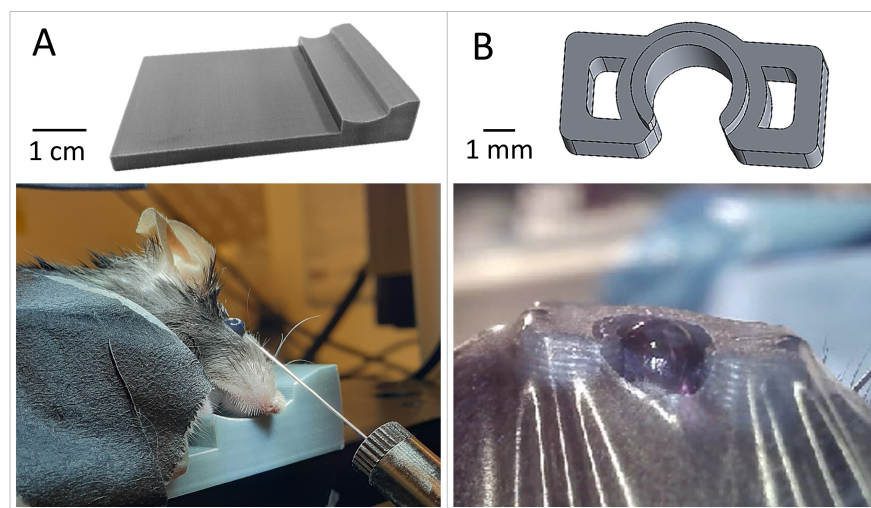


Figure 4.3 3D printed models for (A) optimized positioning of the mouse head under the OCT and (B) stabilization of the eye during the injection.

4.4.2 Injection with a sharp needle

Table 4.1 shows the results obtained for the different study parameters, starting with testing two injection angles with respect to the limbus. Better results were obtained when inserting the needle parallel to the limbus, with an approximative 1 mm long intracorneal trajectory prior to entering the AC, the open side of the bevel towards the AC and without pushing the needle further inside the AC (Figure 4.4A). This approach yielded a 67% successful piercing rate against 33% when using the perpendicular orientation (Figure 4.4B), with more severe tissue damage, whether piercing was successful or not, and significantly more wound leakage, all of which disqualified the perpendicular approach. This configuration was also inconvenient because of the co-alignment of the OCT and the needle, which prevented adequate visualization.

Once the best configuration of injection angle was determined, subsequent experiments were performed with a parallel orientation. Performance of all needle gauges (31 G, 33 G, 34 G, 35 G, 36 G) was then tested for AC injections of 0.5 μL of OCT contrast agent, based on the outcome parameters previously described. The 36 G needle was rapidly discarded since clogging was observed with the viscous OCT contrast agent. As a consequence of the blockage, higher pressure was applied to the syringe plunger, resulting in eye damage due to the high-pressure jet when declogging. Another disadvantage of this thin needle was its

fragility, with easy tip damage and a tendency to bend under pressure (a minimum rigidity is needed to pierce the cornea). Injections were easier and caused less damage with the 35 G needles. The 35 G needles were the only ones that did not rupture the lens capsule contrary to the 31 G, 33 G, 34 G. Figure 4.4C illustrates examples of the corneal endothelial wounds left by the needles with the largest (31 G; 256 μm puncture site) and smallest (35 G; 160 μm) diameters.

Figure A.3 of Appendix A) shows how OCT imaging of the AC depth before and after removing the needle allowed to measure AC collapse caused by wound leakage. As illustrated in Figure 4.4D, taking into account the piercing percentage and the complication rate while controlling for the needle orientation, number of bevels and main bevel angle (parallel piercing using 30° with 3 bevels in all cases), the 35 G needle yielded the highest performance. They showed a lower incidence of complications and these complications were also less severe, making it the preferred option for the subsequent stages of the study.

It was also decided to keep the length of the needles at 5 mm. A slight deflection was repeatedly observed before penetration of the AC with longer needles, reducing guidance and precision, thus increasing the risk of damage to the ocular structures.

The first approach for laser-reshaping was to reduce the main bevel angle of the commercial needles from 30° to 15° in order to flatten the tip and achieve a profile closer to that of a surgical knife, that would facilitate penetration of the corneal tissue. We report an 86% successful piercing rate for injections performed with our modified 15° needle tips, versus 57% for injections done with the 30° needles, with an average damage rate of 50% and 68%, respectively.

Subsequently, we compared the injections done with a single bevel needle versus a tri-surface configuration (main bevel angle of 15° and two lateral lancets). The single bevel needle did not enter the tissue as easily, resulting in globe distortion while pushing on the needle (Figure 4.4E). Once piercing was initiated, however, rapid re-expansion of the compressed globe proved to be at high risk for traumatizing structures of the anterior segment of the eye. On the other hand, the tri-surface blade-like configuration allowed easier piercing, with significantly less globe distortion, if any, and less tissue damage (Figure 4.4F). [172–175] The piercing percentage using our custom-made needles increased to 83% compared to 17% when using a single bevel tip, and the complication rate decreased down to 8% compared to 21%. Data analysis led to the conclusion that the best sharp needle to be used in the mouse model is the modified tri-surfaced 35 G x 5 mm. However, despite minimal damage to the cornea, lens and iris, some leakage was still present after the interventions. For this reason, a second technique of injection was studied, as explained below.

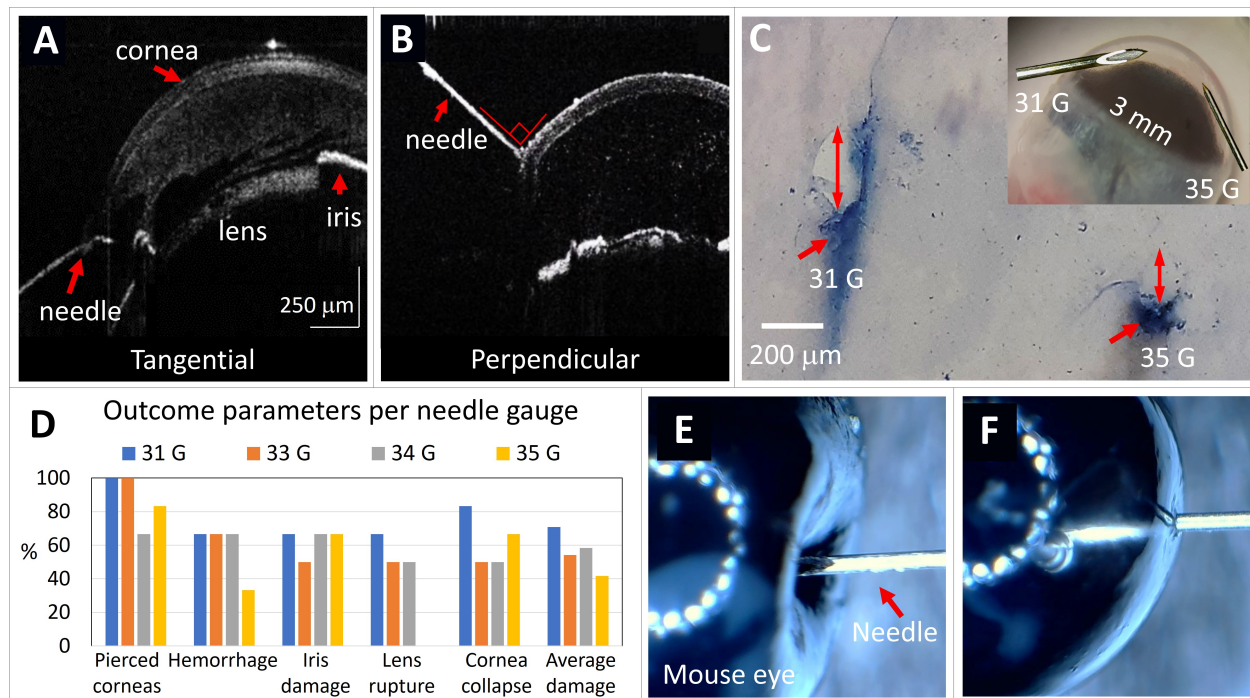


Figure 4.4 Needle orientation and needle size. OCT imaging of (A) parallel and (B) perpendicular injections with respect to the limbus. (C) Histology assessment of the posterior corneal surface after piercing using 31 G and 35 G needles. The double-headed arrows indicate the maximum diameter of the puncture sites ($256\ \mu\text{m}$ and $160\ \mu\text{m}$, respectively). Trypan blue staining (arrow) highlights the extent of endothelial cell damage along the needle trajectory. (D) Performance based on needle gauge. Percentages of pierced corneas, outcome parameters and average damage are shown for each gauge ($N = 6$ eyes in each group; all needle tips with a 30° main bevel and 3 bevels). (E) Corneal distortion produced by the injection with a single bevel needle. (F) Successful injection with a laser-machined tri-surface needle.

4.4.3 Injection with a blunt needle through a corneal incision

For this second technique, a paracentesis knife was used to create a full-thickness, self-sealing, and sutureless corneal incision, through which the blunt needle was inserted without entering the AC. BSS tinted with fluorescein was injected and subsequent imaging with a blue filter confirmed the staining of the AC and the absence of wound leakage after the procedure. The needle gauge was selected based on the best results from the previous studies, and in this case, no sharp needles were needed since the incision involved the full corneal thickness. Figure 4.5A illustrates the progression of the injection.

OCT images were taken after injections in order to compare the wounds made with the conventional sharp needle versus the paracentesis knife, using a 35 G needle in both cases.

In the representative example illustrated in Figure 4.5B, the sharp needle induced corneal stromal edema, a gap in the external half of the wound, a thickening of the iris, and a shallow AC. The knife and blunt needle, on the other hand, left a clean oblique wound, with tightly apposed anterior and posterior flaps, and the normal anatomy of the anterior segment was preserved (Figure 4.5C).

Figure 4.5D shows an overall increase in ACD loss as a function of needle diameter, meaning that wound leakage was maximum with larger needles. Figure 4.5D also shows that the smallest gauge (35 G) needles performed even better with a blunt tip through a self-sealing incision made with a paracentesis knife than when piercing the cornea with a sharp tip, achieving a successful piercing rate of 94%. The OCT images taken before and after injection with a blunt needle showed a mean increase of 14% (9% to 23%) in ACD in 9 of 14 eyes, confirming the watertightness of these wounds.

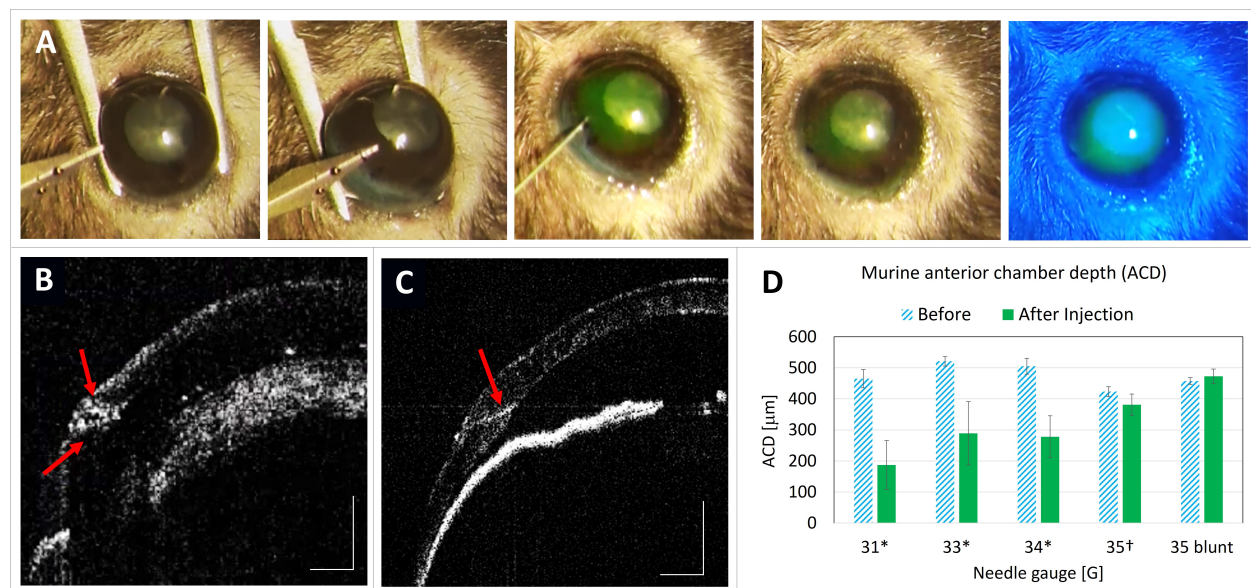


Figure 4.5 Self-sealing corneal incision injection technique. (A) Successive steps including imaging with the blue filter to confirm the absence of leakage. (B) OCT imaging showing significant tissue damage following a sharp needle injection. (C) Self-sealing corneal incision technique resulting in a clean wound with nicely apposed edges (arrow). (D) AC depth before and after injection with different needle gauges. Mean values \pm standard error of the mean are reported. * Sharp needles with a 30° main bevel and 3 bevels; † Sharp needles with a 15° main bevel and 3 bevels. Scale bar: 500 μm .

Table 4.1 Tested conditions for intracameral injection in the murine model.

Injection technique	Conditions	n (eyes)	Successful piercing rate	Average damage	Highest successful piercing rate and lowest damage	
Sharp needle puncture	Needle orientation with respect to the limbus (31 G +30° + 3B*)	Parallel	6	67%	63%	<i>Parallel to limbus</i>
		Perpendicular	6	33%	63%	
	Needle gauge (G) (30°+ 3B)	31	6	100%	71%	<i>35 G</i>
		33	6	100%	54%	
		34	6	67%	58%	
		35	6	83%	42%	
		36	2	-	Discarded due to needle clog- ging	
		Needle tip main bevel angle (35 G +3B)	30°	7	57%	68%
	15°		7	86%	50%	
	Needle tip bevels (35 G +15°)	1	6	17%	21%	<i>3 bevels</i>
		3	6	83%	8%	
Blunt needle through a corneal incision	Using a 1 mm paracentesis knife (35 G)	16	94%	11%	<i>Performance better than sharp needle</i>	

* (G) refers to the needle gauge; (°) main bevel angle; and (B) number of tip bevels

4.4.4 Statistical analysis

Success being based on an easy piercing in the absence of hemorrhage, capsule rupture, leakage and AC collapse, the sum of these indicators was used to define a score from 0 to 5, where a complete success corresponds to a score of 5/5. Using all the data generated in this study (N = 80 eyes used for 80 experiments), a logistic regression on the complete success and a linear regression on the numerical score from 0 to 5 were calculated for sharp needles gauge, main bevel angle and the number of bevels, and the main bevel angle was found to be an important factor in both cases. The logistic regression estimated that a 30° main bevel

angle (compared with 15°) increased the risk of tissue damage by a factor of 13.7, and the linear regression estimated that a 30° angle decreased the success score (0-5) by one unit on average (Table 4.2).

Table 4.2 Logistic and linear regression for sharp needles.

	Logistic regression (Success)		Linear regression (Score 0-5)	
	OR	p-value	β	p-value
Intercept	0.00	1.00	3.3840	0.47
Gauge	0.89	0.77	0.0381	0.76
Main bevel angle	0.84	0.03	-0.0774	0.0173
Number of bevels	8501.79	0.99	-0.0577	0.86

The overall performance of the 35 G blunt needles ($n = 16$) was also compared to that of 35 G sharp needles ($n = 32$, including 30° , 15° , 1 bevel, and 3 bevels). Blunt needles were found to be superior to sharp needles for all outcome parameters, with statistically significant differences for iris damage, wound leak and AC collapse and marginally significant differences for piercing, level of difficulty, and hemorrhage (Table 4.3).

4.5 Discussion

We developed and optimized two techniques for safe and efficient intracameral injections in the murine model, one with a sharp needle and one with a blunt needle through a self-sealing corneal microincision. The best results for sharp needles were obtained with injections at the iridocorneal angle, parallel to the limbus, using a 5-mm long 35 G microneedle, with a tri-surface tip configuration consisting of a main bevel angle of 15° and two lateral lancets, all of which resulted in an easy piercing, with minimal tissue damage. The second injection technique, which involved a self-sealing corneal microincision in which the blunt needle was inserted, resulted in even less tissue damage, higher wound watertightness and less AC collapse. This paper was meant to serve as a guide for optimizing the repeatability and safety of intracameral injections while preserving as much as possible the integrity of the anterior segment structures of the mouse eye. Several studies have explored different needle tip configurations and injection techniques. In the field of dermal injections, clinical research has primarily focused on diabetic patients, with the main objective being to reduce pain caused by insulin needles [146, 176, 177]. Studies have shown that reducing the size

Table 4.3 Outcome parameter comparison between sharp and blunt needles.

Outcome parameter	Level	Blunt	Sharp	Statistics	p-value
Piercing	0	1 (6.2%)	11 (34.4%)	$\chi^2(1) = 3.13$	0.08
	1	15 (93.8%)	21 (65.6%)		
Level of difficulty	Difficult	5 (31.2 %)	21 (65.6 %)	$\chi^2(1) = 3.79$	0.052
	Easy	11 (68.8 %)	11 (34.4 %)		
Hemorrhage	0	14 (87.5 %)	18 (56.2 %)	$\chi^2(1) = 3.39$	0.07
	1	2 (12.5 %)	14 (43.8 %)		
Iris damage	0	14 (87.5 %)	16 (50.0 %)	$\chi^2(1) = 4.9$	0.027
	1	2 (12.5 %)	16 (50.0 %)		
Lens capsule rupture	0	13 (81.2 %)	22 (68.8 %)	$\chi^2(1) = 0.33$	0.57
	1	3 (18.8 %)	10 (31.2 %)		
Wound leak	0	13 (81.2 %)	15 (46.9 %)	$\chi^2(1) = 7.21$	0.027
	1	3 (18.8 %)	7 (21.9 %)		
	2	0 (0.0 %)	10 (31.2 %)		
Cornea collapse	0	13 (81.2 %)	15 (46.9 %)	$\chi^2(1) = 8.97$	0.011
	1	1 (6.2 %)	7 (21.9 %)		
	2	0 (0.0 %)	10 (31.2 %)		

and modifying the tip geometry of the needle decreases pain and increases the likelihood of successful piercings in humans [146,178]. In our case, pain was not a factor since all *in vivo* experiments were conducted under general anesthesia. Computational simulations have been developed to facilitate injection in diverse applications [179,180]. Materials of different densities simulating tissues have also been used to analyze how needle gauges impact insertion dynamics [147,176,181]. The primary variables studied include needle gauge and tip profile, such as the number and angle of bevels [145,174,182].

In the field of eye research, subconjunctival, retrobulbar, intracorneal, intracameral, intravitreal, and subretinal injections have been used in different species, however only rarely with the goal of understanding and optimizing the dynamics of the injection itself. In the murine eye, routes of administration have been studied for glaucoma [165,183], virus-based gene therapy [184,185], and ocular drug implants [186], nevertheless, there remains a gap in the

literature for a method that allows high precision, safe, and reproducible intracameral injections in mice.

In our hands, location and orientation of the needle were additional important parameters. Inserting the sharp needle parallel to the limbus, with an approximative 1 mm long intracorneal trajectory prior to reaching the AC and using the smallest diameter needle strong enough to resist deformation, resulted in the creation of a clean and narrow intracorneal needle path. Clearing the aperture of the needle main bevel towards the AC while remaining in the AC angle is all that was necessary and sufficient to allow smooth injection into the AC. Once the needle is positioned in this way, it is important to remain stable, without moving backwards to avoid needle extrusion and/or retrograde leakage during injection, and without pushing the needle forward any further, which could result in lens, iris, endothelium and angle damage, and even through-and-through perforation. Care should also be taken to avoid any lateral movement that would tear the wound. Following injection, the needle is retrieved, leaving behind a collapsed stromal tunnel. Although it was not necessary during our experiments, this stromal wound can also be hydrated while retrieving the needle, to increase watertightness. Contrary to the peripheral approach parallel to the limbus, the perpendicular approach requires penetration of the sharp needle tip deeper in the AC in order to free the aperture of the needle, which significantly increases the risk for corneal, iris and lens damage.

Although the central AC is usually deeper than in the periphery, central injections were not tested in this study, as they would induce central corneal edema and reduce visibility of the intraocular structures, to the detriment of the study validity. Some authors and manufacturers also propose the use of 5 bevels, with two extra bevels on the posterior part of the needle. It must be remembered however that increasing the number of bevels weakens the needle tip, and broken needle tips may increase the risk for tissue damage both during piercing and when withdrawing the needle from the eye. In agreement with the literature [187,188], the needle tips in our study were only used once.

The two techniques described herein offer major advantages, however both require a minimum of training. Injection with a sharp needle through a peripheral corneal tunnel-shaped wound parallel to the limbus is probably the safest technique in most hands, because when correctly performed, the needle aperture opens on the AC without penetrating further into the eye. However, this technique requires control of the needle stability. On the other hand, while the injection with a blunt needle through a self-sealing corneal microincision offers the best piercing rate and the lowest risk of wound leakage, the corneal incision with the paracentesis knife could increase the risk for intraocular tissue damage in inexperienced hands.

Stability being a key parameter for the precision of the intracameral injection in the mouse eye, the motorized micromanipulator, our 3D-printed plate designed to optimize positioning of the mouse head, access to the cornea and OCT visualization of the AC during injection, our 3D eye holder designed to stabilize the globe during piercing of the cornea, as well as real-time OCT guidance and color camera monitoring while injecting, altogether have increased significantly the success of the injections.

Overall, the setup described above was highly effective and it is relatively simple to reproduce. Furthermore, the two AC injection techniques developed and optimized using either sharp or blunt needles have allowed improved precision, reproducibility and safety in the murine model.

In summary, we propose an optimized semi-automated setup and two techniques for safer injections in the mouse AC, with improved precision and reproducibility. We foresee that implementation of any of these upgrades could be of significant help in research laboratories performing intracameral injections in the murine model.¹

On this note, the injection technique with a blunt needle through a self-sealing corneal microincision was used in the following stage of the project to perform the study of optoporation and transfection in the murine and rabbit cornea, as described in Chapter 5.

¹For this specific chapter, submitted as an article, the authors thank Mohand Ouamar Bellil and Fatiha Azouz for their assistance and the personnel from the animal facility at the Maisonneuve Rosemont Hospital Research Center as well as Charles-Édouard Giguère for its assistance with the statistical analysis. This work was supported by the Collaborative Health Research Program (CHRP CPG 1588262), The Canadian Institutes of Health Research (CHIR 387865), the Nanomedicines Innovation Network (NMIN 22019-T2-04), and the Réseau de Recherche en Santé de la Vision du Québec.

CHAPTER 5 FEMTOSECOND LASER GOLD NANOPARTICLE-MEDIATED *EX VIVO* MRNA DELIVERY WITH HIGH SPECIFICITY IN CORNEAL ENDOTHELIAL CELLS

5.1 Introduction

According to the World Health Organization (WHO), at least 2.2 billion people worldwide have vision impairment [2]. Corneal endothelial diseases are one of the most common problems, affecting around 246 million people globally. [189] The cornea is the only transparent tissue in the human body, which is crucial for light transmission to the retina. Its transparency depends on all cells functioning properly, especially the endothelial layer, which is a monolayer form of non-replicative corneal endothelial cells (CECs) that act as a barrier and pump. When a CEC dies, it creates an excrescences of collagen produced by stressed CECs called a *guttae*, prompting adjacent CECs to stretch and fill the gap, which reduces cell density. [190] In patients with endothelial dystrophies (genetic and possible progressive disease of the corneal endothelium), cell density can drop below the critical threshold of 400-500 cells/mm² ($\sim 20\%$ of corneal cells [191]), leading to functional decompensation, water accumulation, tissue swelling, and vision impairment due to corneal opacification [192]. Corneal transplantation is the only option for patients with advanced dystrophies. However, it is highly invasive, costly, and limited by a shortage of donor corneas. Some of the risks associated to this procedure are tissue rejection and graft failure. Another approach under investigation is gene therapy, which involves identifying the responsible gene(s) causing the dystrophy to deliver the appropriate genetic material. [193] Developing a safe and efficient method for gene transfer (transfection) into target cells is thus crucial. Various methods, including biological, [66] chemical, [64, 65] and physical approaches, [67–69] have been studied to improve transfection efficacy. [194–196] Some drawbacks of current techniques include lack of specificity, potential toxicity, and issues related to time consumption and invasiveness.

To overcome present limitations, lasers have been implemented as a sub-cellular microsurgery tool. [99, 197] By focusing light on individual cells, transient submicrometer holes can be created in cell membranes (optoporation), facilitating transfection or drug delivery. [198, 199] Several lasers are already widely used in ophthalmology in corneal surgeries for tissue ablation. [72–79] Particularly, femtosecond (fs) lasers in the near-infrared (NIR) range are well-suited for cell surgery with the possibility of avoiding ablation. Their ultra-short pulse duration allows for high peak power and minimal heat diffusion to surrounding tissues. Moreover, biological tissues have lower absorption in the NIR range, allowing for deeper laser penetra-

tion and reduced side effects. [103] External agents like nanoparticles (NPs) can enhance the efficacy of laser-based cell surgery by acting as enhancer agents, thereby reducing the energy required for treatment. [200] Organic [104] and inorganic materials, such as carbon or plasmonic NPs, have been studied. Among plasmonic materials, [105–113] gold nanoparticles (AuNPs) have been extensively used in various biological systems. [201, 202] Their chemical stability [203, 204] and possibility for functionalization help target specific cells, [205] enhancing specificity, and reducing side effects. [106, 109, 206]

If the NP resonance frequency is aligned with the femtosecond (fs) laser wavelength, the energy absorption is significantly increased, resulting in a pronounced thermal effect. However, a major concern is the potential toxicity arising from material fragmentation caused by the intense laser-matter interaction. [207, 208] Conversely, off-resonance optoporation can be achieved implementing laser systems centered in the NIR range. [158, 209] In this case, plasma formation occurs around the irradiated nanoparticle, leading to bubble formation (nanocavitation) and subsequent bubble collapse. This process generates a shock wave that induces the formation of a transient pore in the cellular membrane. [83, 120, 210] Research into gene therapy targeting the cornea remains relatively unexplored. In this work, we propose combining AuNPs with a fs laser to develop a novel therapeutic technique for treating CECs.

The objective of this study is to provide a less-invasive, translatable and safer alternative for transfection of CECs, potentially eliminating the need for corneal transplantation in the future. The primary goal was to achieve significant mRNA transfection in murine CECs while maintaining high cell viability. Additionally, optoporation was performed in rabbit corneas to demonstrate the translatability of this technique across different animal species. Complementary characteristics of both, mouse and rabbit, help to bridge the gap towards applications in human corneas. Mice are widely recognized as excellent models for corneal diseases, [11, 211] while rabbit corneas are closer to human anatomy. [212] *Ex vivo* experiments are presented to provide a controlled environment, enabling precise and stable laser targeting and thereby enhancing the reliability of the results, which is essential for early-stage research.

The findings presented here offer insights that can potentially guide future *in vivo* experiments. The high selectivity of this optoporation and transfection technique relies on using a focused fs laser in combination with AuNPs attached to CECs. Results demonstrate negligible side effects and low toxicity, with high internalization rates maintaining cell viability well above the critical threshold for CEC density. This study paves the way for gene therapy as a safer alternative to corneal transplantation.

5.2 Results and discussion

Ex vivo experiments, which refers to assessments conducted on biological tissues outside of their living organism, were performed using both mouse and rabbit eyes to provide a comprehensive study. Mice were used for a detailed investigation, including nanoparticle toxicity and optoporation for mRNA transfection. Transfection efficacy was compared with results obtained from standard lipofectamine assessments. This extensive analysis allows for a thorough understanding of the effects and mechanisms involved in laser treatment in CECs. Subsequently, rabbit corneas were utilized to evaluate fluorophore uptake. These findings are valuable for translating results to both mouse models of endothelial diseases and human corneas from eye banks, demonstrating the applicability and potential impact of the research and translatability of the presented technique among different species.

In the first stage, mouse and rabbit eyes were enucleated immediately after euthanasia, in alignment with international ethical guidelines from the Association for Research in Vision and Ophthalmology (ARVO). The eyes were maintained in saline solution in custom-made 3D holders. Additionally, ophthalmic gel was applied to the cornea to ensure hydration (Figure 5.1A).

Subsequently, a mixture of functionalized AuNPs and the corresponding exogenous molecule was injected into the anterior chamber (Figure 5.1B). Various concentrations of AuNPs were tested to optimize optoporation. Functionalization was done following an standard EDC-NHS protocol [160] using anti-CD44 antibody aiming to improve the selective attachment of NPs to CECs. The eyes were then placed in a prone position (with the cornea facing downwards) for a one-hour incubation period before laser irradiation. This position privileged the contact of AuNPs with the endothelial cells (Figure 5.1C). An optical system was engineered utilizing a fs laser to irradiate mouse and rabbit corneas *ex vivo*. The eyes were positioned on a translational stage to irradiate in spiral fashion (Figure 5.1D), implementing a microscope objective to focalize the energy specifically in CECs. Various energy densities were tested to optimize optoporation and molecule internalization.

Following laser irradiation, the eyes were kept at 37 °C for 48 hours in the holders designed to maintain the natural curvature of the corneas. This second incubation period allowed passive internalization of the exogenous molecules into the cells (Figure 5.1E). Corneal dissection was then performed to flat-mount the tissue for visualization (Figure 5.1F). Imaging and quantification of the efficacy were achieved through fluorescence imaging (Figure 5.1G). The efficacy was determined by comparing the total number of irradiated cells to the number of cells expressing fluorescence. In the case of mouse samples, the internalized molecule was

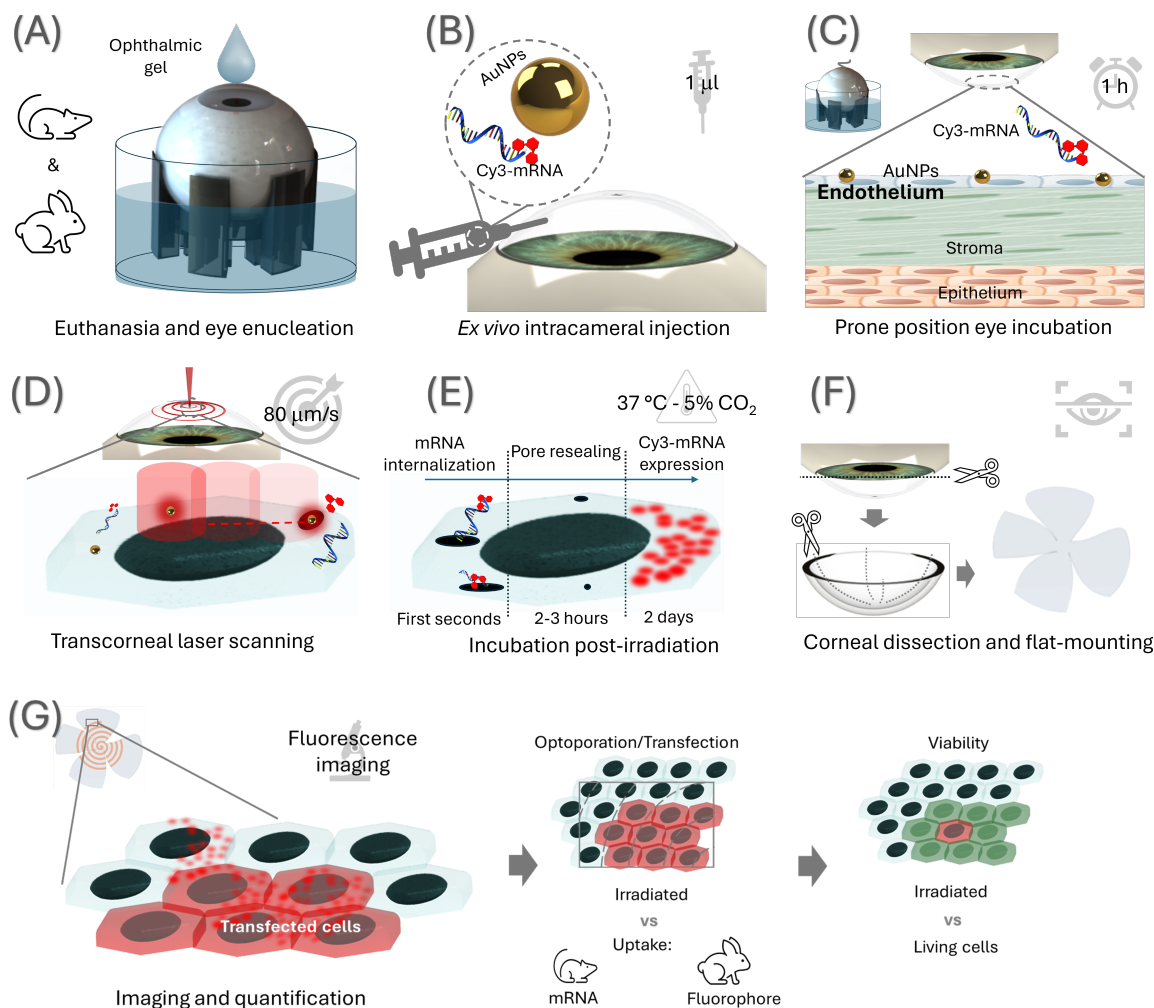


Figure 5.1 Schematic representation of *ex vivo* transfection assessment. Steps include the (A) Euthanasia and eye enucleation for both, mice and rabbits. Followed by (B) intracameral injection of a mix of mRNA (for mice) or PI (for rabbits) with AuNPs. (C) One-hour incubation in prone position at 37 °C allowed to ensure the maximum number of NPs in CECs. The samples are subsequently positioned in a translational stage programmed with spiral movements for (D) laser irradiation at 80 $\mu\text{m/s}$. (E) Optoporation happens in a nanosecond timescale allowing gene/fluorophore internalization, while the pore resealing is produced in the following hours. Fluorescence can be then detected 48 hours post-irradiation. (F) Flat mounting of the sample is necessary for (G) imaging to quantify the technique efficacy and cell viability.

Cy3 EGFP-mRNA, which is approximately 10 nm in size [59,60]. For the rabbit samples, the small fluorophore propidium iodide (PI), of approximately 1 nm in size, was selected. Calcein-AM staining was performed to quantify cell viability.

5.2.1 AuNP incubation in *ex vivo* murine eyes

First, concentration and toxicity assessments for AuNPs were performed in murine eyes *ex vivo*. Mice were euthanized following ethical protocols to subsequently perform intracameral injections *ex vivo*. After one-hour incubation, murine corneas were dissected and flat-mounted for NP quantification using bright-field imaging. The rationale behind the incubation time was based on the average duration required for complete replacement of the aqueous humor for *in vivo* conditions in the anterior chamber [213].

The optimal number of NPs was determined by considering two main factors: i) negligible toxicity, and ii) homogeneous distribution (low agglomeration). We report successful AuNPs attachment to CECs as illustrated in Figure 5.2A. Artificial coloring was applied to the images for visualization purposes using the software ImageJ. In these images, the cell junctions are highlighted in red, while NPs appear in yellow. Quantification (n=3 for each concentration) reveals the presence of 9 ± 4 , 88 ± 11 and 171 ± 14 NPs/cell for 2×10^8 , 2×10^9 and 2×10^{10} NPs/mL respectively. All values are expressed as mean \pm SD.

It is well established that particles interact with the energy from the laser, resulting in a plasmonic effect off-resonance in this case ($\lambda = 800$ nm). Consequently, a cluster or aggregate of AuNPs could induce a more pronounced localized effect, possibly creating a large pore in the cell membrane. If this pore exceeds the cell's self-sealing capacity, cell viability can significantly decrease. With a higher presence of clusters the technique becomes less controlled. On this note, the presence of clusters of NPs was also verified to select the optimal concentration for subsequent laser irradiation. The number of clusters per cell was 18 ± 1 , 4 ± 1 , and 17 ± 3 corresponding to the different concentrations of AuNPs/cell above mentioned (lower to higher).

Bright-field images were taken to confirm the transparency of the cornea 48 hours post-injection, as can be observed in Figure 5.2B. It was possible to observe the presence of AuNPs aggregates for a concentration of 2×10^{10} NPs/mL conversely to the two lower concentrations injected. In order to consider the presented technique as a potential tool for use *in vivo*, the transparency of the cornea must be ensured at every step of the study. Based on the high viability, low clustering formation and preservation of the cornea transparency, the selected concentration of NPs used for subsequent experiments was 2×10^9 NPs/mL.

Viability assessments were conducted 48 hours post-injection, coinciding with the expected time frame for evaluating gene internalization. As can be seen in Table 5.1, cell viability was found $95 \pm 3\%$ and $94 \pm 2\%$ for the two lowest concentrations (n=3 for each concentration). Nevertheless, in the case of 2×10^{10} NPs/mL, the viability decreased to $37 \pm 20\%$. The toxicity

resulted negligible for lower concentrations of particles such as 2×10^8 and 2×10^9 AuNPs/mL. On the other side, the ideal scenario for optoporation tests, is a homogeneous distribution of particles in the tissue. Using a concentration of 2×10^9 AuNPs/mL, the quantified number of NPs per cell is 88 ± 11 . This corresponds to an approximate density of 3 NPs per $10 \mu\text{m}^2$, assuming an average corneal endothelial cell area of $300 \mu\text{m}^2$ and a mean cell diameter of $20 \mu\text{m}$. The percentage of cell membrane surface covered by NPs is estimated to be less than 1%, suggesting a negligible impact on light transmission. As shown in Figure 5.2B, the transparency of the cornea was visually determined after the injection of three different concentrations in murine eyes. The images were taken with a white light source that allowed analysis of transparency change after injections. No apparent change in transparency was detected, and scattering effects and absorption from the NPs resulted in negligible for the visible range given the low density of NPs on the CECs, except for the highest concentration of 2×10^{10} AuNPs/mL which was excluded due to reduced cell viability. Further analysis of the transparency of the cornea is proposed as a follow-up study to determine the long-term effect of the plasmonic material in the tissue.

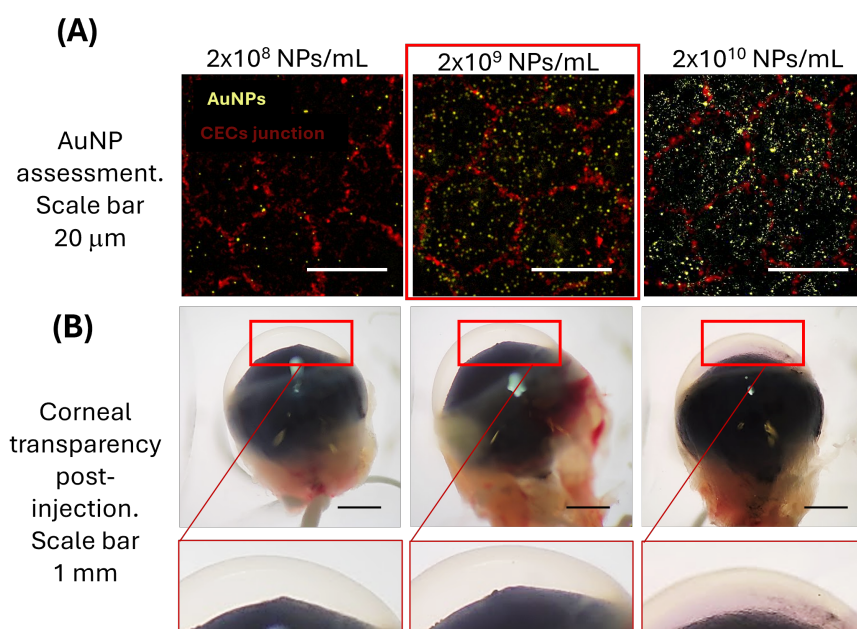


Figure 5.2 AuNP assessment in murine eyes *ex vivo*. (A) CEC images showing AuNP attachment after 1 hour incubation; (B) corneal transparency 48 h after injection of AuNPs.

Table 5.1 NP assessment in *ex vivo* murine corneas.

NPs concentration ^a [NPs/mL]	NPs/cell ^b	CEC viability ^c [%]	Clusters/cell [%]
2x10 ⁸	9 ± 4	95 ± 3	18 ± 1
2x10 ⁹	88 ± 11	94 ± 2	4 ± 1
2x10 ¹⁰	171 ± 14	37 ± 20	17 ± 3

^a Concentration of injected AuNPs; ^b Quantification made one hour after injection; ^c CEC viability was assessed 48 h after injection.

5.2.2 Optoporation and cellular transfection in *ex vivo* murine corneas

Different conditions were evaluated for optoporation and transfection efficacy. The initial phase of the study involved the assessment of laser fluence ranging from 50 to 250 mJ/cm² (with 50 mJ/cm² intervals and n=3 for each fluence value) to determine the cell viability post-irradiation in the presence of AuNPs (2x10⁹ NPs/mL). Fluorescent images of the irradiated sections of murine CECs were taken to evaluate cell death 48 hours after laser treatment. Figure 5.3A.I shows an example of the viability assessment performed with Calcein-AM following irradiation at 100 mJ/cm².

The highest viability was obtained when irradiated at 50 mJ/cm², achieving 93 ± 3% comparable to control samples resulting in 95 ± 2 %. Conversely, the transfection rate was not significant at this fluence compared to higher fluence values. As illustrated in Figure 5.3B, the viability decreases drastically for fluence values ≥ 150 mJ/cm². At 200 mJ/cm², the highest fluence value used in this study, bubbles and subsequent endothelial cell detachment were observed post-irradiation (the dashed white line indicates the laser path). On the other side, the highest transfection percentage was found to be 66 ± 18% achieved at a fluence of 150 mJ/cm².

Due to the non-replicative nature of CECs, the optimal irradiation fluence is determined by the highest optoporation rate without compromising cell viability. It is important to note that the minimum percentage of live cells required post-treatment is 20 %, based on the critical density necessary for proper corneal function. Additionally, the energy used in this study is well below the minimal visible laser lesion (MVL) threshold for the cornea, which has been reported as 400 mJ/cm². [214–217]

The optimal condition for laser and AuNP-assisted transfection in murine corneas was found to be 100 mJ/cm² (Figure 5.3A.II). Fluorescence images of viability and transfection for each evaluated fluence are available in Figure B.2 of Appendix B. Control samples confirm that Cy3 EGFP-mRNA transfection in CECs is only possible when using a combination of

AuNPs and laser irradiation at the referred concentration and fluence (Figure 5.3C). Notably, the internalization of Cy3 EGFP-mRNA was observed exclusively in the irradiated corneal endothelial layer, with no significant uptake detected in stromal or epithelial cells.

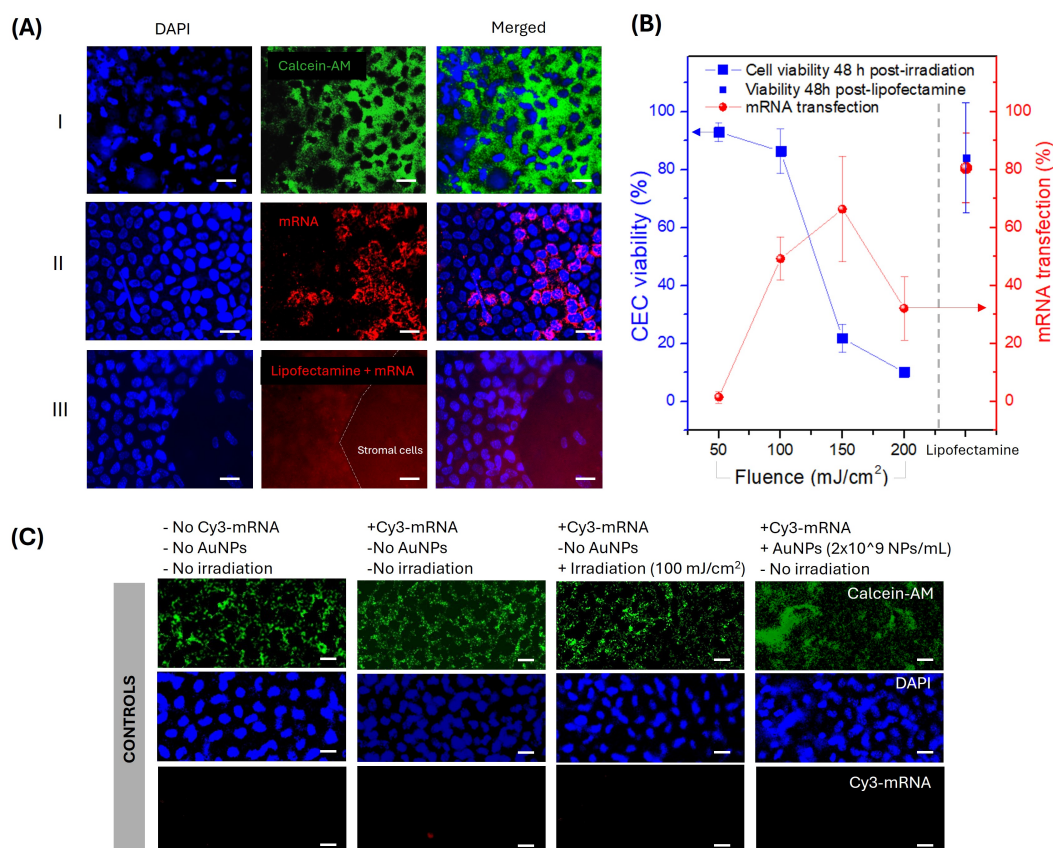


Figure 5.3 *Ex vivo* murine CEC viability and transfection; (A) I - Viability assessment using Calcein-AM, II - mRNA transfection using Cy3 EGFP-mRNA, III – Lipofectamine assessment with Cy3 EGFP-mRNA. Scale bar corresponds to 20 μ m. (B) Cell viability and transfection vs fluence compared with lipofectamine assessment.

5.2.3 Lipofectamine assessment in *ex vivo* murine corneas

In order to compare the transfection efficacy of the presented technique with a standard method, lipofectamine was used to evaluate the transfection of Cy3 EGFP-mRNA in CECs *ex vivo*. Intracameral injections of a mix of lipofectamine and Cy3 EGFP-mRNA were performed under the same incubation conditions used for plasmonic particles and laser irradiation. The results show $81 \pm 9\%$ (for $n=3$) internalization with cell viability of $84 \pm 15\%$ (for $n=3$). Figure 5.3A.III shows fluorescent images of CECs after 48 h incubation with the lipofectamine mix. Its corresponding graph is shown in Figure 5.3B. Even though the transfection rate is

higher for lipofectamine when compared to our laser-assisted method, a clear advantage is the selectivity achieved with the combination of the focalized laser and AuNPs. For the lipofectamine assessment, fluorescence from Cy3 was observed in all layers of the cornea, as shown in Figure 5.3A.III. Red fluorescence was present not only in CECs but also in the stromal cells.

5.2.4 Optoporation and cellular fluorophore uptake in *ex vivo* rabbit corneas

Using the same concentration of AuNPs as with murine samples (2×10^9 NPs/mL), viability tests using Calcein-AM were performed on *ex vivo* rabbit corneas after 48-hour incubation. Cell viability is reported after 48 hours as $74 \pm 10\%$ (Figure 5.4A). Even though the same concentration of AuNPs/mL used for murine samples was implemented (2×10^9 NPs/mL), the number of NPs found on CECs after one hour incubation, was lower compared to mice corneas, resulting 48 ± 6 NPs/cell.

Subsequently, irradiation tests were conducted on rabbit corneas using the same fluence range (50-200 mJ/cm²). However, due to the lower number of AuNPs observed in CECs after 1 hour of incubation, no uptake was observed when irradiating at 50 mJ/cm². For this reason, the fluence range was slightly increased to 100-250 mJ/cm². The percentage of fluorophore uptake increased with fluence, reaching a maximum at 200 mJ/cm². Cell viability remains consistent with control samples up to this fluence value. However, when irradiating at 250 mJ/cm², CECs sustain significant damage, resulting in a drastic decrease in viability. For detail information on uptake at different fluences, refer to the Figure B.5 of Appendix B.

Similar to the murine samples, the optimal irradiation condition balances high cellular uptake with maintaining high cell viability. In this case, we report an optimal viability of $76 \pm 9\%$ and fluorophore internalization of $95 \pm 3\%$ when irradiating at 200 mJ/cm² (Figure 5.4B). As shown in Figure 5.4C, the presented technique demonstrates high selectivity, as evidenced by the correlation between the laser path (indicated by a dashed white line) and the internalized PI (red fluorescence), maintaining high cell viability (Calcein-AM staining).

Control samples are presented in Figure 5.4D demonstrating that fluorescence from PI staining corresponds specifically to laser treatment with AuNPs. Tests confirmed negligible toxicity and phototoxicity when samples were incubated with AuNPs and irradiated without the presence of plasmonic material, respectively. The implementation of small fluorophores such as PI (<1 nm in size) permitted a rapid uptake assessment with the proposed optoporation technique.

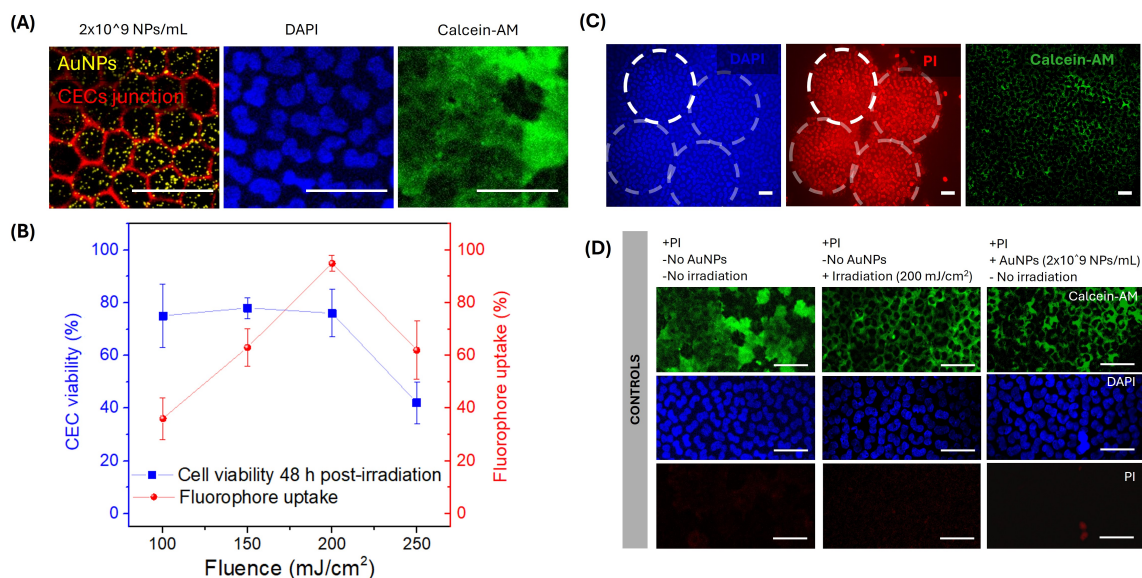


Figure 5.4 AuNPs in *ex vivo* rabbit CECs, viability and fluorophore uptake. **(A)** AuNPs quantification using alizarin red for cell junctions, DAPI (blue) and Calcein-AM (green) were implemented for cell viability. **(B)** Fluorophore uptake at 200 mJ/cm² with 2E9 AuNPs/mL using PI (red) with its corresponding DAPI and Calcein-AM assessment; dotted line represents the laser path (pitch size: 20 μ m). **(C)** A 48-hour assessment for viability and fluorophore uptake percentage per fluence value. **(D)** Control samples illustrating the negligible effect of PI toxicity (1 μ g/mL), irradiation without AuNPs, and NP incubation without irradiation. Scale bar corresponds to 50 μ m in all figures.

5.3 Conclusion

This study demonstrates an alternative treatment for CECs in both *ex vivo* murine and rabbit models with high specificity. The controlled environment that *ex vivo* experiments provide allowed for the isolation of different variables to accurately assess the effects of our technique on CECs. On this note, results of low toxicity and negligible *ex vivo* side effects of this transcorneal approach pave the way for further *in vivo* implementation.

We report a highly selective optoporation and transfection method using a fs laser combined with biocompatible functionalized AuNPs. The critical threshold of CEC density is known to be 20% of the cells in the tissue. Our results show that viability under optimized irradiation conditions exceeds 70% in rabbits and 80% in mice, ensuring a safe treatment for subsequent *in vivo* applications.

For the internalization of large molecules, such as mRNA, our solutions containing Cy3 EGFP-mRNA achieved a 49% internalization rate in treated areas. While standard techniques like lipofectamine report higher internalization rates, their lack of specific delivery is a

significant limitation. Lipofectamine uptake occurs in all cell types in the anterior chamber, whereas our technique specifically targets only the cells decorated with functionalized AuNPs that undergo laser irradiation. This high specificity can be advantageous in drug delivery therapy, enhancing internalization and reducing side effects.

Rabbit CECs demonstrated to be more resistant to optoporation compared to mouse CECs, necessitating slight modifications to the irradiation conditions to optimize cellular uptake across different animal models. This complementary study showcases the flexibility of our technique, enabling its translation across various species. *Ex vivo* experiments on rabbit corneas further demonstrate the translatability of the technique to other mammals with anatomies similar to humans and its potential for future applications to treat endothelial diseases to avoid corneal transplantation.

5.4 Methods

This *ex vivo* study was conducted under ethical protocols approved by the local ethical committee in accordance with the guidelines of the Canadian Council on Animal Care (CCAC) and the ARVO.

5.4.1 Mouse cornea preparation

Twenty C57BL/6 mice were used for experiments *ex vivo*. Intraperitoneal injections were performed to administer pentobarbital sodium at a dosage of 40 mg/kg. After euthanasia, ophthalmic gel (Refresh Optive, Allergan Inc. Dublin, Ireland) was applied to all corneas to prevent ocular dryness as shown previously in Figure 5.1A. Following eye enucleation detailed in Appendix B, the samples were transferred to a custom-made 3D holder designed and adapted to maintain the curvature radius of murine corneas during incubation. Additionally, a second holder was created to keep the eye in an optimal position during injection, and irradiation fitting within a 2.5 cm standard Petri dish aiming to keep the eye moisturized with a balanced saline solution (BSS purchased from Alcon, 0065080094 Ontario, Canada).

Intracameral injections detailed in Chapter 4 were performed delivering 1 μ L of a mix including Cy3 EGFP mRNA (1 μ g/mL) purchased from Cedarlane (R1008-.1, Ontario, Canada) and colloidal AuNPs (2×10^8 - 2×10^{10} NPs/mL) to each eye to subsequently incubate the globes in the prone position. This configuration privileged the contact between AuNPs and CECs during incubation.

The eyes were maintained in BSS to prevent desiccation. In this case, no supplements were added to the culture media to avoid interference with mRNA molecules. After one hour of

incubation, the eyes were repositioned with the corneas facing upwards for laser treatment. Subsequently, the eyes were transferred to Opti-MEM purchased from ThermoFisher Scientific (31985070) and kept at 37 °C and 5% CO₂ forty-eight hours post-treatment in prone position, allowing the Cy3 EGFP-mRNA to be internalized. The corneas were dissected (as detailed in the Appendix B) and gently transferred to a microscope slide to perform flat-mounting and staining for cell quantification.

5.4.2 AuNPs

AuNPs of 100 nm in diameter (50 µg/mL), purchased from Nanopartz (A11-100-CIT, Colorado, USA) were implemented for all the experiments. Functionalization of AuNPs was done following standard EDC-NHS protocol. [160] The aim of the functionalization was to increase the specific attachment of the plasmonic material to CECs. The implemented antibody was anti-CD44 (Hermes-1, MA4400, ThermoFisher Scientific).

Three different concentrations of AuNPs were tested to determine the optimal amount of plasmonic material for optoporation and transfection studies: i) 2×10^8 , ii) 2×10^9 , and iii) 2×10^{10} NPs/mL. Toxicity tests were performed incubating the 3 different concentrations of AuNPs with CECs for 48 hours.

5.4.3 Fluorophores and chromophores

All fluorophores used for cell quantification were diluted in phosphate buffered saline (PBS) purchased from SigmaAldrich, Canada following recommended protocols from the manufacturers. The nucleus of all cells was identified with blue fluorescence using standard DAPI staining at 2 µg/mL (62247, ThermoFisher Scientific).

Cy3 EGFP-mRNA (1 µg/mL) was used in combination with DAPI to identify the endothelial layer and quantify transfection efficacy. The red and blue fluorescence from Cy3 and DAPI staining correspondingly were compared within the irradiation area to obtain the percentage of uptake 48 h after irradiation. CEC viability tests were done with standard staining, using the green fluorophore Calcein-AM 2 µg/mL (C3099, ThermoFisher Scientific).

In the case of rabbit corneas, PI at 1 µg/mL (P1304MP, ThermoFisher Scientific) was used as a quick assessment for rabbit CECs uptake minutes after laser-AuNP interaction identified as red fluorescence [218]. Alizarin red S with pH 4.2 at 0.2% (K1186, ApexBio, Texas, USA) was used to visualize cell junctions [219].

5.4.4 Optical setup

The optical setup utilizes an Nd:YAG (neodymium-doped yttrium aluminum garnet; Nd:Y3Al5O12) pump laser to excite the Ti:Sapphire laser delivering fs pulses at a high repetition rate (76 MHz).

These pulses are then directed into a regenerative amplifier (RA) to produce short pulses (45 fs) at a reduced repetition rate of 1 kHz. The output from the RA undergoes expansion and redirection using metallic mirrors optimized for 800 nm, before being focused onto the target stage (A3200 Aerotech) where samples were placed using the customized holders designed for the eyes. The irradiation was performed in spiral fashion for all samples at 80 $\mu\text{m/s}$ with a pitch size of 20 μm .

A 5x microscope objective (M Plan Apo; Mitutoyo, Japan) was used to focalize the beam on CECs. The measured beam spot was 20 μm at $1/e^2$. The focalized beam enhances resolution and specificity by minimizing collateral damage to surrounding areas during laser treatment. A rotating polarizer combined with a waveplate was implemented to regulate the power delivered to the sample. In terms of the Rayleigh Range (Z_R) of the implemented objective, the calculation can be made following equation 5.1, considering $W_0 = 10 \mu\text{m}$, refractive index (n) of 1.37 (corresponding to the corneal stroma) and $\lambda = 800 \text{ nm}$. The result of the calculation is 538 μm . The central corneal thickness in mouse and rabbit is 137 ± 14 and $376 \pm 20 \mu\text{m}$ respectively, which allows optoporation even if the system is focalized slightly out of the endothelial layers. On the same note, since the fluence is low enough to avoid optoporation without the presence of the NPs, the surrounding cells to the treatment and the tissue on the laser path that does not contain NPs are free of optoporation. This adds to our technique a high specificity product of the combination of plasmonic NPs and the fs laser.

$$Z_R = \frac{\pi W_0^2 n}{\lambda} \quad (5.1)$$

Additionally, the potential damage of the rest of the tissues in the optical path, such as crystalline lens and retina is negligible thanks to the focalization of the beam at the corneal level. The transmitted light arriving at the crystalline is considered an extended source, thus minimizing the risk of ablation since no focalization is done at the retinal level. To facilitate the focusing for laser irradiation of CECs, a CMOS camera is integrated into the system to provide simultaneous visualization of the sample.

5.4.5 Optoporation, transfection and viability quantification

Cell counting was carried out from DAPI images (blue fluorescence from cell nuclei) identifying the number of cells/mm² using the software ImageJ. Background subtraction was used as a first stage to homogenize the images prior quantification. Subsequently, the 3D object counter plugin [163] was used for image analysis. The procedure for optoporation and transfection quantification was based on the detection of red fluorescence from either Cy3 EGFP-mRNA (mouse samples) or PI (rabbit tissue). Images of red fluorescence before and after irradiation were taken to compare the efficacy of the laser treatment. To calculate optoporation rate, images were taken 1 hour after irradiation. The efficacy was calculated dividing the number of cells expressing red fluorescence (identified post-irradiation) by the total number of cells given by blue fluorescence (DAPI). In the case of transfection calculation, images were taken 48 hours after irradiation. The first step after DAPI counting, was to establish a baseline fluorescence by taking images with the Cy3 filter of different areas where no irradiation was performed. This baseline fluorescence was subtracted from the images taken at the irradiation areas. Subsequently, the number of cells where red fluorescence (Cy3 EGFP-mRNA) was expressed was divided by the number of nuclei (DAPI).

Viability assessments were performed 48 hours after following two techniques: i) for mouse corneas Calcein-AM standard staining was performed (5 μ g/mL); ii) for rabbit samples, alizarin red S and trypan blue were used considering as dead cells those whose nucleus appears blue on bright field microscopy.

5.4.6 Transfection by lipofectamine

Transfection tests using Lipofectamine MessengerMAX mRNA Transfection Reagent (LM-RNA001, ThermoFisher Scientific) were performed to compare with the proposed technique. Standard transfection protocol proposed by the manufacturer was followed for murine corneas. Fluorescence imaging was performed 48 hours after incubation of Cy3 EGFP-mRNA mixed with lipofectamine.

5.4.7 Rabbit corneas preparation

Ex vivo experiments were performed in 10 wild-type rabbits. Eye enucleation was conducted as detailed in Appendix B. Right after enucleation, the eyes were kept in BSS to avoid desiccation.

A mix of AuNPs (2x10⁹ NPs/mL) and two different fluorophores: i) DAPI (2 μ g/mL) and PI (1 μ g/mL) was injected. The rabbit eyes were then transferred into 3D-printed holders

(3D model available in Appendix B) specially designed to keep the natural curvature of the eyes during incubation time. The holders were engineered to fit into a 24-well plate. The hollow structure of the 3D printed holders allows the culture medium to reach the tissue, ensuring that the sample remains adequately moisturized during the incubation and irradiation. The eyes were incubated for one hour in prone position to enhance the probability of NP attachment to CECs as in the case of murine samples. Complete culture medium Opti-MEM purchased from ThermoFisher Scientific (31985070) supplemented with 10% fetal bovine serum (FBS) and 5% penicillin - streptomycin was used for incubation. Samples were kept at 37°C and 5% CO₂ before and after laser irradiation.

5.4.8 Imaging

Fluorescence and bright-field imaging were performed using an inverted microscope (Eclipse Ti2, Nikon, Tokyo, Japan). The different types of images were treated and merged using the software ImageJ.

Reflected light microscopy (RLM) was used to quantify the number of NPs in the tissue, while fluorescence and bright-field images allowed the identification of CECs. DAPI images were obtained using a Nikon blue filter cube with excitation 375/28 nm / emission 460/50 nm. For PI and Cy3 images, the red filter implemented was optimized for excitation 554/23 nm / emission 609/54 nm. Alizarin red S and trypan blue images were taken with bright-field imaging using standard white light source. Three Nikon objectives were used to acquire images: i) 4X, plan Fluor (0.14 NA), ii) 20X (0.45 NA) plan Fluor and iii) 60X oil immersion objective (0.5-1.15 NA).

This Chapter represents the proof of optoporation and transfection in murine tissues implementing one of the injection technique developed in Chapter 4. ¹

¹For this specific thesis Chapter, the authors thank Marilyse Piché, Fatiha Azouz, and Mohand Ouamar Bellil for their technical assistance. Special thanks are extended to the personnel from the animal facility at the Maisonneuve-Rosemont Hospital for their support. We also acknowledge from Polytechnique Montréal, Yves Drolet for his technical assistance, Leonidas Agiotis and Cécile Darvot for their constructive feedback, as well as Isabelle Largillière and Scott G. Harroun for comments on the manuscript. This study was generously supported by grants from the Nanomedicine Innovation Network (NMIN) and the Réseau de Recherche en Santé de la Vision (RRSV).

CHAPTER 6 GENERAL DISCUSSION

As detailed in the literature review, the currently approved treatment for advanced endothelial diseases is corneal transplantation, a highly invasive intervention with elevated costs for both patients and health systems. Although some alternative research techniques exist, certain gaps hinder their application.

By addressing these gaps and aiming to minimize the drawbacks of current techniques, the main objective of this thesis was successfully achieved. This involved the use of clinically approved procedures, such as intraocular injections and laser treatment in ocular interventions for correcting refractive problems. With the presented results, we propose extending this use to correct genetic dystrophies.

In vitro experiments

The proof of principle was established using ocular cells *in vitro*. This step was crucial for refining variables related to biological, optical, and mechanical aspects.

From a biological perspective, variability in NP distribution was observed. As seen in the literature and confirmed by immunostaining assays, NP distribution is likely influenced by the heterogeneous expression of membrane proteins. The number of attached NPs can vary depending on the cell phase and species due to differences in membrane protein expression. *In vitro* tests provided a good approximation of the fluence range that can be used; however, the monolayer nature of the culture does not allow for the prediction of some manipulation implications, such as tissue fragility. Manipulation of tissue was a critical stage of the project; minimal folding of the tissue produced wrinkles that translated into dead cells during viability assessments.

From an optical perspective, the fluence was adjusted to achieve a high optoporation rate while maintaining high cell viability.

From a mechanical perspective, high fluence samples showed some cell damage at the borders of the irradiation area, likely due to increased exposure time from mechanical factors of the translation stage. During irradiation, a serpentine scanning pattern was programmed in the translational stage (controlled with LabView). The dwell time associated with the mechanical characteristics of the stage resulted in laser overexposure at the borders of the irradiated area, particularly at direction change points, leading to cell detachment. This observation highlighted a potential problem for subsequent *ex vivo* experiments. Therefore, a circular

irradiation pattern was preferred for the following animal model experiments.

Ex vivo experiments

Mice are one of the most common animal models used in research, so the techniques implemented in this study were adapted to their eye anatomy to overcome limitations related to size and structure. Since NPs must be in contact with endothelial cells, efficient delivery is essential. The optimal method for delivering NPs is by injecting them into the anterior chamber. The anterior chamber depth is approximately 500 μm , while the corneal thickness is around 160 μm .

Conventional needles used for intraocular injections are about 250 μm in diameter, making them highly invasive and risky for use in mice eyes. Therefore, two injection protocols were developed and adapted for intracameral interventions in murine models. The initial approach involved using a sharp needle. After analyzing various parameters, we determined that the optimal needle for the murine model is a modified tri-surfaced needle, 135 μm in diameter and 5 mm in length.

To minimize the number of wasted needles and experiment with a narrower bevel angle, the needles were laser-machined for resharpening after each use. The goal of laser reshaping was to reduce the primary bevel angle from 30° (commercial needles) to 15°, flattening the tip to achieve a profile more similar to a surgical knife, thereby facilitating the penetration of corneal tissue. The second approach involved the use of blunt needles.

A paracentesis knife was used to create a full-thickness, self-sealing, and sutureless corneal incision, followed by injection with a needle of the same diameter and length (135 μm and 5 mm respectively). Our results show reduced bleeding, negligible corneal collapse, and high cell viability post-injection.

Intraocular injections were a crucial initial step for successful optoporation, as they enabled precise localization of AuNPs in contact with the endothelial cells. Optoporation and subsequent transfection were studied in animal models *ex vivo*. The rationale behind conducting *ex vivo* experiments lies in the ability to maintain a controlled environment, which is essential for early-stage research.

In the case of *in vivo* samples, the breathing and heart beating of the animals are two important aspects that increase the complexity of the visualization and irradiation.

The purpose of this study was to demonstrate the proof-of-principle of this new technique without having to address the compensation for the movements of the animal since sophisticated and often cumbersome adjustments to the setup would be required. This added com-

plexity can introduce variability and potential inaccuracies in targeting the cells of interest. Conducting the experiments *ex vivo* thus eliminates these movement-induced complications, allowing for precise and stable laser targeting, thereby enhancing the reliability of the results. Further development would require implementation of adaptive optics or self-focusing systems.

This research enabled the isolation and study of various variables, including: i) specificity (targeted delivery of molecules exclusively to endothelial cells), ii) uptake (percentage of molecule internalization), iii) toxicity (negligible at the recommended concentrations of molecules and AuNPs), and iv) phototoxicity (minimal within the suggested fluence range). From an ethical standpoint, due to the lack of data on tissue response after NP incubation and laser irradiation, it was necessary to evaluate corneal integrity before proceeding with *in vivo* assessments. Additionally, the direct evaluation of corneal transparency within 48 hours post-irradiation is more straightforward in an *ex vivo* setting.

Our results were compared with standard methods, such as lipofectamine (known for its toxicity in *in vivo* environments). Although lipofectamine achieved a higher internalization rate, the specificity of our technique is invaluable, translating to fewer side effects. Unlike lipofectamine, our method transfects only the cells in direct contact with both the NPs and laser irradiation, ensuring no other cell layers are affected.

This study addresses several major issues associated with other techniques like electroporation and virus-based approaches, namely i) toxicity and ii) lack of specificity.

Additionally, the only clinically accepted method currently is corneal transplantation, which carries the risks of invasiveness and possible graft rejection. While our method involves intraocular injection, the invasiveness is significantly reduced, and cell integrity is preserved, as demonstrated by our injection protocols. Moreover, our approach eliminates the need for tissue transplantation, completely removing the risk of graft failure.

Translatability

To demonstrate the translatability of the optoporation technique across different species, we conducted complementary studies using mice and rabbits. Mice were chosen due to their genetic similarities with humans, making them an appropriate model to evaluate and compare responses of the organism to specific stimuli or treatments. This model is cost-effective and provides accurate disease modeling for a variety of ocular diseases, including endothelial dystrophies.

Conversely, rabbits are preferred in ophthalmology due to their anatomical and physiological

similarities to human eyes. The robustness and replicative ability of CECs allowed for quick viability assessments post-treatment. From a practical point of view, the larger size of rabbit corneas facilitates easier handling and data collection compared to the smaller mouse eyes. Additionally, the corneal thickness of rabbit eyes is comparable to corneal thickness in humans, making this an important parameter in considering the suitability of our transfection technique for human application in the future.

In summary, with this interdisciplinary research we have successfully demonstrated the validity of our hypothesis and achieved the established objectives. We hypothesized that using a tightly focused femtosecond laser to irradiate CECs decorated with biocompatible functionalized AuNPs would create transient pores in the endothelial cellular membrane with high precision, thereby facilitating the delivery of exogenous molecules only in the targeted cells.

The proof of principle established *in vitro* provided critical insights that informed subsequent steps in animal models. This led to the development of a safer protocol for intracameral injection in murine models, which enhanced AuNP attachment to CECs. As a result, we achieved significant mRNA transfection in these models while maintaining high cell viability in *ex vivo* studies.

Moreover, femtosecond (fs) lasers, primarily used for ablation in corneal surgery, and intraocular injections, whether administered as a single dose or on a monthly basis, are both well-established and clinically approved practices. The proposed approach complies with regulations designed to ensure that laser treatments remain within safe energy exposure levels, thus preventing damage to the corneal tissue and surrounding ocular structures. According to the literature, the ablation threshold for fs lasers in corneal tissue is 400 mJ/cm². Based on the findings of this thesis, it is suggested to implement 100 mJ/cm² for murine models and 150 mJ/cm² for rabbit corneal tissue for 800 nm wavelength at 1kHz repetition rate and 45 fs pulse width.

Furthermore, our research confirmed the translatability of the optoporation and transfection technique across different species, setting the stage for future experiments using human corneal tissue from eye banks or specific disease animal models. This interconnected approach not only validated our hypothesis but also ensured that each stage of the project supported and advanced the subsequent stages.

CHAPTER 7 CONCLUSION

7.1 Summary of Work

The ultimate aim was to overcome the drawbacks of the only clinically approved treatment in humans for advanced endothelial dystrophies, corneal transplantation, and offer a better alternative when compare with current techniques under research.

As a proof of concept, *in vitro* studies were conducted in ocular cells, demonstrating successful internalization rates. A GFP plasmid DNA was tested in the final stage of these studies, showing low internalization but sufficient for cellular studies. Optimization of the parameters for optimal internalization was planned for tissue studies.

For the *ex vivo* stage, the transfection material was switched to mRNA for three main reasons: i) the production of pDNA was complex and time-consuming, requiring fresh stock for each experiment, which increased research costs; ii) literature indicated the risk of undesired integration of plasmid DNA into the host genome, potentially leading to harmful genetic mutations (mutagenesis); and iii) mRNA-based gene transfection has been proven more effective in non-dividing cells, such as CECs, compared to pDNA. This summarizes the achievement of the sub-objective 1 that was to establish a proof of principle using ocular cells.

In this study, maintaining the integrity of the eye, particularly the cornea, was essential for subsequent stages. It was crucial for AuNPs to be in contact with CECs, and to avoid corneal desiccation, intracameral injections were determined to be the most effective delivery method.

Two improved and safer protocols for intraocular injections were successfully implemented, thus achieving the second sub-objective of this thesis. The injections in the murine model resulted with minimized damage such as bleeding, corneal collapse, and cellular death. The need for improved visualization, incubation, and positioning of the enucleated eyes at various stages led to the design and 3D printing of customized eye holders, facilitating experimentation.

In terms of irradiation, the deposited energy (100 and 150 mJ/cm² for mouse and rabbit tissues, respectively) falls within the biological window and remains well below the minimal visible laser lesion threshold of the cornea (reported as 400 mJ/cm²), minimizing side effects on other corneal layers. Additionally, AuNPs are biocompatible, and our toxicity tests confirmed that the concentrations used are safe for murine and rabbit CECs. This resumes the achievement of our third sub-objective which was to achieve a significant transfection of

mRNA in the murine model ($49 \pm 7\%$, mean \pm SD) with high cell viability (above 80 %).

Two different species were selected for this research due to their distinct advantages in ocular studies, providing a complementary *ex vivo* analysis and demonstrating the translatability of the proposed technique achieving the forth sub-objective of this work. Mice are widely used in research because of their well-characterized genetics and availability, while rabbits, with their larger eyes and physical characteristics similar to humans, offer a suitable model for ocular studies. The results of optoporation and transfection are promising, showing effective cellular uptake and high cell viability. These findings support the potential future implementation of this technique *in vivo*.

In conclusion, the integration of *in vitro* and *ex vivo* testing across two animal models in this research project has facilitated a thorough evaluation of both procedural efficacy and biological outcomes. The successful achievement of the four sub-objectives demonstrates that the primary goal of this thesis was also accomplished. Specifically, this research developed a non-invasive gene therapy method utilizing biocompatible plasmonic AuNPs, combined with laser therapy.

Our results confirm the efficacy of this approach, highlighting its potential for precise and controlled gene and drug delivery in ocular applications for corneal endothelial treatment.

7.2 Limitations

Although this thesis presents robust results, several limitations inherent to *ex vivo* models must be acknowledged.

Differences in systemic interactions and environmental conditions between living organisms and *ex vivo* tissues can influence tissue behavior and experimental outcomes. For example, corneal explants and other tissues used in *ex vivo* studies have a finite viability period outside the organism. In this study, visualization was limited to 48 hours post-enucleation due to the limited lifespan of CECs *ex vivo*, which directly impacts the duration of experiments and the time available for observation.

Furthermore, removing tissues from their natural physiological context can alter cellular behavior, gene expression, and tissue function. As a result, slight adjustments in fluence, molecule and AuNP concentrations, may be necessary when translating findings to *in vivo* models, due to the absence of integrated physiological systems and complex interactions in *ex vivo* studies.

Despite these limitations, *ex vivo* studies are invaluable for controlled investigations and can provide critical insights that complement *in vivo* research.

7.3 Future research towards *in vivo*

For *in vivo* assessment and potential future applications, the technique involves an intraocular injection that has been proved to be safe for the most challenging species: the mouse. The proposed protocol, can be implemented as presented, nevertheless for optoporation and transfection, slight modifications might be considered. Following the injection, the NPs will be allowed to incubate for 1 hour while the subject remains in a prone position. This positioning enhances the contact between NPs and CECs, as supported by the literature.

Another important consideration is the follow-up time. It is essential to evaluate longer incubation periods after irradiation to ensure the long-term negligible toxicity of NPs and genetic material. An area that requires further exploration is the pharmacokinetics of NP distribution following injection into the anterior chamber. Assessing the pathways of NP excretion from the mouse body could serve as a complementary toxicity analysis.

The implementation of other CECs markers is also suggested to increase the specificity of the technique. The implemented anti-CD44 does not target the most abundant protein expressed on the CECs, nevertheless, sufficient binding was observed for the intended application. Based on literature findings, the future use of CD166, SLC4A11, COL8A2, CYR1, CD98, and CD340 surface markers, could increase the number of AuNPs per cell due to their higher expression in CECs [161,220].

Given that the aqueous humor replacement time is reported to be around one hour, this could influence the number of NPs per cell after this period. As a result, adjustments to the fluence may be necessary, potentially requiring an increase. Additionally, precise positioning of the animal under the optical setup is crucial; therefore, using a stereotaxic instrument is recommended to minimize undesired movements and enhance precision during irradiation.

Anticipated limitations include animal breathing when focusing the laser within the sample, changing the position where the focalized light interacts with the tissue. Thus, an autofocus system or the use of adaptive optics is suggested. A consideration for treating diseased mice is that treatment must occur before the pathology is visible, in the early stages of the disease when the cornea is still transparent. *In vivo* experiments will provide follow-up exceeding 48 hours, helping determine the final success rate of the transfection technique before translating it to human samples.

Another suggestion is the evaluation of this technique in specific knock-out mice models for endothelial diseases such as Fuchs' dystrophy. This approach would allow for the direct application and assessment of the technique's efficacy in a relevant disease context. By using knock-out mice, we can gain valuable insights into the therapeutic potential and mechanistic

effects of the treatment on endothelial cell function and viability, ultimately paving the way for targeted clinical applications.

As highlighted in the thesis, when transitioning from *in vitro* to *ex vivo*, pDNA, which induces a permanent effect, was replaced with mRNA to mitigate potential genotoxicity. Further in-depth evaluation of pDNA toxicity is recommended to assess the potential long-term effects of the proposed technique

REFERENCES

- [1] I. K. Gipson, “Age-related changes and diseases of the ocular surface and cornea,” *Investigative ophthalmology & visual science*, vol. 54, no. 14, pp. ORSF48–ORSF53, 2013.
- [2] W. H. Organization, “Blindness and vision impairment,” 2023. [Online]. Available: <https://www.who.int/news-room/fact-sheets/detail/blindness-and-visual-impairment>
- [3] P. Garg *et al.*, “The value of corneal transplantation in reducing blindness,” *Eye*, vol. 19, no. 10, pp. 1106–1114, 2005.
- [4] J. P. Whitcher, M. Srinivasan, and M. P. Upadhyay, “Corneal blindness: a global perspective,” *Bulletin of the world health organization*, vol. 79, no. 3, pp. 214–221, 2001.
- [5] G. Vedana, G. Villarreal Jr, and A. S. Jun, “Fuchs endothelial corneal dystrophy: current perspectives,” *Clinical ophthalmology*, pp. 321–330, 2016.
- [6] B. D. Allan *et al.*, “Corneal transplant rejection rate and severity after endothelial keratoplasty,” *Cornea*, vol. 26, no. 9, pp. 1039–1042, 2007.
- [7] O. C. Alldredge and J. H. Krachmer, “Clinical types of corneal transplant rejection: their manifestations, frequency, preoperative correlates, and treatment,” *Archives of Ophthalmology*, vol. 99, no. 4, pp. 599–604, 1981.
- [8] J.-P. F. Roussy *et al.*, “Cost of corneal transplantation for the quebec health care system,” *Canadian Journal of Ophthalmology*, vol. 44, no. 1, pp. 36–41, 2009.
- [9] A. M. Smith, M. C. Mancini, and S. Nie, “Second window for in vivo imaging,” *Nature nanotechnology*, vol. 4, no. 11, pp. 710–711, 2009.
- [10] J. Won *et al.*, “Mouse model resources for vision research,” *Journal of ophthalmology*, vol. 2011, no. 1, p. 391384, 2011.
- [11] S. Murugan *et al.*, “Characterization of a novel mouse model for fuchs endothelial corneal dystrophy,” *Investigative Ophthalmology & Visual Science*, vol. 65, no. 4, pp. 18–18, 2024.
- [12] R. S. Snell and M. A. Lemp, “The anatomy of the eyeball as seen with the ophthalmoscope, slit lamp, and gonioscope,” *Clinical Anatomy of the Eye*, pp. 214–230, 1997.

- [13] D. K. Sunderland and A. Sapra, “Physiology, aqueous humor circulation,” 2020.
- [14] D. Atchison, *Optics of the human eye*. CRC Press, 2023.
- [15] M. la Cour and B. Ehinger, “The retina,” *Advances in Organ Biology*, vol. 10, pp. 195–252, 2005.
- [16] S. Jacob and P. Naveen, “Anatomy of the cornea,” *Mastering Endothelial Keratoplasty: DSAEK, DMEK, E-DMEK, PDEK, Air pump-assisted PDEK and others, Volume I*, pp. 1–11, 2016.
- [17] F. Rüfer *et al.*, “Age-related changes in central and peripheral corneal thickness: determination of normal values with the orbiscan ii topography system,” *Cornea*, vol. 26, no. 1, pp. 1–5, 2007.
- [18] F. Rüfer, A. Schröder, and C. Erb, “White-to-white corneal diameter: normal values in healthy humans obtained with the orbiscan ii topography system,” *Cornea*, vol. 24, no. 3, pp. 259–261, 2005.
- [19] S. Patel and L. Tutchenko, “The refractive index of the human cornea: A review,” *Contact Lens and Anterior Eye*, vol. 42, no. 5, pp. 575–580, 2019.
- [20] R. Snell and M. Lemp, “Clinical anatomy of the eye, blackwell science,” 1998.
- [21] A. M. Brooks, G. Grant, and W. Gillies, “The identification of corneal guttae,” *Cornea*, vol. 10, no. 3, pp. 249–260, 1991.
- [22] M. Thériault *et al.*, “Function-related protein expression in fuchs endothelial corneal dystrophy cells and tissue models,” *The American Journal of Pathology*, vol. 188, no. 7, pp. 1703–1712, 2018.
- [23] G. Brambatti *et al.*, “Corneal endothelial cell density and morphology in rabbits’ eyes using contact specular microscopy,” *Ciência Rural*, vol. 47, p. e20170027, 2017.
- [24] J. Bu *et al.*, “Hyperlipidemia affects tight junctions and pump function in the corneal endothelium,” *The American Journal of Pathology*, vol. 190, no. 3, pp. 563–576, 2020.
- [25] A. S. Jun *et al.*, “Aging changes of mouse corneal endothelium and descemet’s membrane,” *Experimental eye research*, vol. 83, no. 4, pp. 890–896, 2006.
- [26] W. H. Organization *et al.*, “World report on vision,” 2019.

- [27] K. Gordon, "Paying the price: The cost of vision loss in canada," *Canadian Journal of Optometry*, vol. 72, no. 2, pp. 11–11, 2010.
- [28] A. F. Cruess *et al.*, "The cost of vision loss in canada. 2. results," *Canadian journal of ophthalmology*, vol. 46, no. 4, pp. 315–318, 2011.
- [29] R. R. Bourne *et al.*, "Magnitude, temporal trends, and projections of the global prevalence of blindness and distance and near vision impairment: a systematic review and meta-analysis," *The Lancet Global Health*, vol. 5, no. 9, pp. e888–e897, 2017.
- [30] M. Matthaai *et al.*, "Fuchs endothelial corneal dystrophy: clinical, genetic, pathophysiologic, and therapeutic aspects," *Annual review of vision science*, vol. 5, no. 1, pp. 151–175, 2019.
- [31] M. Moshirfar, P. Bennett, and Y. Ronquillo, "Corneal dystrophy," 2020.
- [32] J. S. Weiss *et al.*, "Ic3d classification of corneal dystrophies—edition 2," *Cornea*, vol. 34, no. 2, pp. 117–159, 2015.
- [33] E. N. Vithana *et al.*, "Slc4a11 mutations in fuchs endothelial corneal dystrophy," *Human molecular genetics*, vol. 17, no. 5, pp. 656–666, 2008.
- [34] D. Malhotra and J. R. Casey, "Molecular mechanisms of fuchs and congenital hereditary endothelial corneal dystrophies," *Reviews of Physiology, Biochemistry and Pharmacology*, pp. 41–81, 2020.
- [35] B. W. Iliff, S. A. Riazuddin, and J. D. Gottsch, "The genetics of fuchs' corneal dystrophy," *Expert review of ophthalmology*, vol. 7, no. 4, pp. 363–375, 2012.
- [36] A. J. Aldave, J. Han, and R. F. Frausto, "Genetics of the corneal endothelial dystrophies: an evidence-based review," *Clinical genetics*, vol. 84, no. 2, pp. 109–119, 2013.
- [37] D. W. DelMonte and T. Kim, "Anatomy and physiology of the cornea," *Journal of Cataract & Refractive Surgery*, vol. 37, no. 3, pp. 588–598, 2011.
- [38] K. Bizheva *et al.*, "In vivo imaging and morphometry of the human pre-descemet's layer and endothelium with ultrahigh-resolution optical coherence tomography," *Investigative ophthalmology & visual science*, vol. 57, no. 6, pp. 2782–2787, 2016.
- [39] M.-M. Gellrich, "The fundus slit lamp," *Springerplus*, vol. 4, pp. 1–16, 2015.
- [40] W. Douthwaite and W. Evardson, "Corneal topography by keratometry," *British journal of ophthalmology*, vol. 84, no. 8, pp. 842–847, 2000.

- [41] O. Villavicencio *et al.*, “Corneal pachymetry: new ways to look at an old measurement,” *Journal of Cataract & Refractive Surgery*, vol. 40, no. 5, pp. 695–701, 2014.
- [42] I. Jalbert *et al.*, “In vivo confocal microscopy of the human cornea,” *British Journal of Ophthalmology*, vol. 87, no. 2, pp. 225–236, 2003.
- [43] S. P. SUGRUE and J. D. ZIESKE, “Zo1 in corneal epithelium: association to the zonula occludens and adherens junctions,” *Experimental eye research*, vol. 64, no. 1, pp. 11–20, 1997.
- [44] A. O. Eghrari and J. D. Gottsch, “Fuchs’ corneal dystrophy,” *Expert review of ophthalmology*, vol. 5, no. 2, pp. 147–159, 2010.
- [45] M. Ziaei, E. Sharif-Paghaleh, and B. Manzouri, “Pharmacotherapy of corneal transplantation,” *Expert Opinion on Pharmacotherapy*, vol. 13, no. 6, pp. 829–840, 2012.
- [46] D. T. Tan *et al.*, “Corneal transplantation,” *The Lancet*, vol. 379, no. 9827, pp. 1749–1761, 2012.
- [47] M. Parekh *et al.*, “Targeting corneal disorders using gene therapy,” *Expert Review of Ophthalmology*, vol. 7, no. 4, pp. 351–362, 2012.
- [48] P. E. Saw and E. Song, “Advancements in clinical rna therapeutics: Present developments and prospective outlooks,” *Cell Reports Medicine*, 2024.
- [49] M. Y. Rincon, T. VandenDriessche, and M. K. Chuah, “Gene therapy for cardiovascular disease: advances in vector development, targeting, and delivery for clinical translation,” *Cardiovascular research*, vol. 108, no. 1, pp. 4–20, 2015.
- [50] M. H. Amer, “Gene therapy for cancer: present status and future perspective,” *Molecular and cellular therapies*, vol. 2, pp. 1–19, 2014.
- [51] H. Moradian *et al.*, “mrna transfection-induced activation of primary human monocytes and macrophages: dependence on carrier system and nucleotide modification,” *Scientific reports*, vol. 10, no. 1, p. 4181, 2020.
- [52] H. Youn and J.-K. Chung, “Modified mrna as an alternative to plasmid dna (pdna) for transcript replacement and vaccination therapy,” *Expert opinion on biological therapy*, vol. 15, no. 9, pp. 1337–1348, 2015.
- [53] S. Zou *et al.*, “Lipid-mediated delivery of rna is more efficient than delivery of dna in non-dividing cells,” *International journal of pharmaceuticals*, vol. 389, no. 1-2, pp. 232–243, 2010.

- [54] L. Warren *et al.*, “Highly efficient reprogramming to pluripotency and directed differentiation of human cells with synthetic modified mrna,” *Cell stem cell*, vol. 7, no. 5, pp. 618–630, 2010.
- [55] A. M. Lam and P. R. Cullis, “Calcium enhances the transfection potency of plasmid dna–cationic liposome complexes,” *Biochimica et Biophysica Acta (BBA)-Biomembranes*, vol. 1463, no. 2, pp. 279–290, 2000.
- [56] K. Le Blay *et al.*, “Efficient transient gene expression in neurosphere with jetmessenger™ mrna transfection reagent.”
- [57] P. Guo, “The emerging field of rna nanotechnology,” *Nature nanotechnology*, vol. 5, no. 12, pp. 833–842, 2010.
- [58] M. A. Hink *et al.*, “Structural dynamics of green fluorescent protein alone and fused with a single chain fv protein,” *Journal of Biological Chemistry*, vol. 275, no. 23, pp. 17 556–17 560, 2000.
- [59] M. Kloczewiak *et al.*, “A biopharmaceutical perspective on higher-order structure and thermal stability of mrna vaccines,” *Molecular pharmaceutics*, vol. 19, no. 7, pp. 2022–2031, 2022.
- [60] M. Yuan *et al.*, “mrna nanodelivery systems: targeting strategies and administration routes,” *Biomaterials Research*, vol. 27, no. 1, p. 90, 2023.
- [61] T. Niidome and L. Huang, “Gene therapy progress and prospects: nonviral vectors,” *Gene therapy*, vol. 9, no. 24, pp. 1647–1652, 2002.
- [62] Z. X. Chong, S. K. Yeap, and W. Y. Ho, “Transfection types, methods and strategies: a technical review,” *PeerJ*, vol. 9, p. e11165, 2021.
- [63] T. K. Kim and J. H. Eberwine, “Mammalian cell transfection: the present and the future,” *Analytical and bioanalytical chemistry*, vol. 397, pp. 3173–3178, 2010.
- [64] D. A. Balazs and W. Godbey, “Liposomes for use in gene delivery,” *Journal of drug delivery*, vol. 2011, no. 1, p. 326497, 2011.
- [65] T. M. Allen and P. R. Cullis, “Liposomal drug delivery systems: from concept to clinical applications,” *Advanced drug delivery reviews*, vol. 65, no. 1, pp. 36–48, 2013.
- [66] A. V. Borovjagin *et al.*, “Adenovirus-based vectors for the development of prophylactic and therapeutic vaccines,” *Novel Technologies for Vaccine Development*, pp. 203–271, 2014.

- [67] H. Manoj and M. Muthaiyan Shanmugam, “Microinjection-based drug delivery,” in *Advanced Drug Delivery: Methods and Applications*. Springer, 2023, pp. 155–178.
- [68] K. Blair-Parks, B. C. Weston, and D. A. Dean, “High-level gene transfer to the cornea using electroporation,” *The Journal of Gene Medicine: A cross-disciplinary journal for research on the science of gene transfer and its clinical applications*, vol. 4, no. 1, pp. 92–100, 2002.
- [69] J. L. Young and D. A. Dean, “Electroporation-mediated gene delivery,” *Advances in genetics*, vol. 89, pp. 49–88, 2015.
- [70] U. K. Tirlapur and K. König, “Targeted transfection by femtosecond laser,” *Nature*, vol. 418, no. 6895, pp. 290–291, 2002.
- [71] A. Vogel and V. Venugopalan, “Mechanisms of pulsed laser ablation of biological tissues,” *Chemical reviews*, vol. 103, no. 2, pp. 577–644, 2003.
- [72] R. R. Krueger, Y. S. Rabinowitz, and P. S. Binder, “The 25th anniversary of excimer lasers in refractive surgery: historical review,” *Journal of Refractive Surgery*, vol. 26, no. 10, pp. 749–760, 2010.
- [73] J. M. Krauss and C. A. Puliafito, “Lasers in ophthalmology,” *Lasers in surgery and medicine*, vol. 17, no. 2, pp. 102–159, 1995.
- [74] M. A. Gilmour, “Lasers in ophthalmology,” *Veterinary Clinics: Small Animal Practice*, vol. 32, no. 3, pp. 649–672, 2002.
- [75] A. Vogel *et al.*, “Cavitation bubble dynamics and acoustic transient generation in ocular surgery with pulsed neodymium: Yag lasers,” *Ophthalmology*, vol. 93, no. 10, pp. 1259–1269, 1986.
- [76] J. Marshall, “Lasers in ophthalmology: the basic principles,” *Eye*, vol. 2, no. 1, pp. S98–S112, 1988.
- [77] J. S. Schuman *et al.*, “Holmium laser sclerectomy: success and complications,” *Ophthalmology*, vol. 100, no. 7, pp. 1060–1065, 1993.
- [78] H. K. Soong and J. B. Malta, “Femtosecond lasers in ophthalmology,” *American journal of ophthalmology*, vol. 147, no. 2, pp. 189–197, 2009.
- [79] C. Wang *et al.*, “Femtosecond laser crosslinking of the cornea for non-invasive vision correction,” *Nature Photonics*, vol. 12, no. 7, pp. 416–422, 2018.

- [80] S. Batabyal, Y.-T. Kim, and S. Mohanty, “Ultrafast laser-assisted spatially targeted optoporation into cortical axons and retinal cells in the eye,” *Journal of Biomedical Optics*, vol. 22, no. 6, pp. 060 504–060 504, 2017.
- [81] S. Batabyal *et al.*, “Nano-enhanced optical gene delivery to retinal degenerated mice,” *Current gene therapy*, vol. 19, no. 5, pp. 318–329, 2019.
- [82] R. Barbuscha *et al.*, “Femtosecond laser system for micromachining of the materials,” in *18th International School on Quantum Electronics: Laser Physics and Applications*, vol. 9447. SPIE, 2015, pp. 130–135.
- [83] K. König, “Cornea surgery with nanojoule femtosecond laser pulses,” in *Ophthalmic Technologies XV*, vol. 5688. SPIE, 2005, pp. 288–293.
- [84] K. Sugioka, M. Meunier, and A. Piqué, *Laser precision microfabrication*. Springer, 2010, vol. 135.
- [85] A. Vogel *et al.*, “Mechanisms of femtosecond laser nanoprocessing of biological cells and tissues,” in *Journal of Physics: Conference Series*, vol. 59, no. 1. IOP Publishing, 2007, p. 249.
- [86] R. R. Gattass and E. Mazur, “Femtosecond laser micromachining in transparent materials,” *Nature photonics*, vol. 2, no. 4, pp. 219–225, 2008.
- [87] M. Yamaji *et al.*, “Three dimensional micromachining inside a transparent material by single pulse femtosecond laser through a hologram,” *Applied Physics Letters*, vol. 93, no. 4, 2008.
- [88] H. Huang, L.-M. Yang, and J. Liu, “Micro-hole drilling with femtosecond fiber laser,” in *Laser Applications in Microelectronic and Optoelectronic Manufacturing (LAMOM) XVIII*, vol. 8607. SPIE, 2013, pp. 46–54.
- [89] R. Le Harzic *et al.*, “Comparison of heat-affected zones due to nanosecond and femtosecond laser pulses using transmission electronic microscopy,” *Applied Physics Letters*, vol. 80, no. 21, pp. 3886–3888, 2002.
- [90] C. Vergés and E. Llevat, “Laser cataract surgery: technique and clinical results,” *Journal of Cataract & Refractive Surgery*, vol. 29, no. 7, pp. 1339–1345, 2003.
- [91] A. Vogel *et al.*, “Intraocular photodisruption with picosecond and nanosecond laser pulses: tissue effects in cornea, lens, and retina.” *Investigative ophthalmology & visual science*, vol. 35, no. 7, pp. 3032–3044, 1994.

- [92] L. J. Esposito, “Lasers in ophthalmology—basic, diagnostic and surgical aspects: A review,” *Archives of Ophthalmology*, vol. 122, no. 7, pp. 1094–1095, 2004.
- [93] P. A. Barnes and K. Rieckhoff, “Laser induced underwater sparks,” *Applied Physics Letters*, vol. 13, no. 8, pp. 282–284, 1968.
- [94] E. Boulais *et al.*, “Plasmonics for pulsed-laser cell nanosurgery: Fundamentals and applications,” *Journal of Photochemistry and Photobiology C: Photochemistry Reviews*, vol. 17, pp. 26–49, 2013.
- [95] E. Lukianova-Hleb *et al.*, “Plasmonic nanobubbles as transient vapor nanobubbles generated around plasmonic nanoparticles,” *ACS nano*, vol. 4, no. 4, pp. 2109–2123, 2010.
- [96] D. Lapotko, “Optical excitation and detection of vapor bubbles around plasmonic nanoparticles,” *Optics express*, vol. 17, no. 4, pp. 2538–2556, 2009.
- [97] B. Zysset, J. Fujimoto, and T. Deutsch, “Time-resolved measurements of picosecond optical breakdown,” *Applied Physics B*, vol. 48, pp. 139–147, 1989.
- [98] C. Puliafito *et al.*, “Laser-tissue interactions in the nanosecond, picosecond and femtosecond time domains,” in *Photoacoustic and Photothermal Phenomena II: Proceedings of the 6th International Topical Meeting, Baltimore, Maryland, July 31–August 3, 1989*. Springer, 1990, pp. 420–427.
- [99] N. Shen *et al.*, “Photodisruption in biological tissues and single cells using femtosecond laser pulses,” in *Technical Digest. Summaries of papers presented at the Conference on Lasers and Electro-Optics. Postconference Technical Digest (IEEE Cat. No. 01CH37170)*. IEEE, 2001, pp. 403–404.
- [100] C. B. Schaffer *et al.*, “Dynamics of femtosecond laser-induced breakdown in water from femtoseconds to microseconds,” *Optics express*, vol. 10, no. 3, pp. 196–203, 2002.
- [101] A. N. Bashkatov *et al.*, “Optical properties of human skin, subcutaneous and mucous tissues in the wavelength range from 400 to 2000 nm,” *Journal of Physics D: Applied Physics*, vol. 38, no. 15, p. 2543, 2005.
- [102] O. Ren and R. Birngruber, “Axicon: a new laser beam delivery system for corneal surgery,” *IEEE journal of quantum electronics*, vol. 26, no. 12, pp. 2305–2308, 1990.
- [103] M.-F. Tsai *et al.*, “Au nanorod design as light-absorber in the first and second biological near-infrared windows for in vivo photothermal therapy,” *ACS nano*, vol. 7, no. 6, pp. 5330–5342, 2013.

- [104] C. Jumelle *et al.*, “Delivery of molecules into corneal endothelium using nanoparticles activated by femtosecond laser pulses: proof of concept,” *Acta Ophthalmologica*, vol. 90, 2012.
- [105] C. Yao *et al.*, “Cancer cell-specific protein delivery by optoporation with laser-irradiated gold nanorods,” *Journal of Biophotonics*, vol. 13, no. 7, p. e202000017, 2020.
- [106] A. M. Wilson *et al.*, “In vivo laser-mediated retinal ganglion cell optoporation using kv1. 1 conjugated gold nanoparticles,” *Nano letters*, vol. 18, no. 11, pp. 6981–6988, 2018.
- [107] F. Lavoie-Cardinal *et al.*, “Gold nanoparticle-assisted all optical localized stimulation and monitoring of ca²⁺ signaling in neurons,” *Scientific reports*, vol. 6, no. 1, p. 20619, 2016.
- [108] A. Bucharskaya *et al.*, “Towards effective photothermal/photodynamic treatment using plasmonic gold nanoparticles,” *International journal of molecular sciences*, vol. 17, no. 8, p. 1295, 2016.
- [109] T. E. Pylaev *et al.*, “Optoporation and recovery of living cells under au nanoparticle layer-mediated nir-laser irradiation,” *ACS Applied Nano Materials*, vol. 4, no. 12, pp. 13 206–13 217, 2021.
- [110] M. Hasanzadeh Kafshgari *et al.*, “Antibody-functionalized gold nanostar-mediated on-resonance picosecond laser optoporation for targeted delivery of rna therapeutics,” *Small*, vol. 17, no. 19, p. 2007577, 2021.
- [111] T. Pylaev *et al.*, “A novel cell transfection platform based on laser optoporation mediated by au nanostar layers,” *Journal of biophotonics*, vol. 12, no. 1, p. e201800166, 2019.
- [112] D. P. O’Neal *et al.*, “Photo-thermal tumor ablation in mice using near infrared-absorbing nanoparticles,” *Cancer letters*, vol. 209, no. 2, pp. 171–176, 2004.
- [113] L. R. Hirsch *et al.*, “Nanoshell-mediated near-infrared thermal therapy of tumors under magnetic resonance guidance,” *Proceedings of the National Academy of Sciences*, vol. 100, no. 23, pp. 13 549–13 554, 2003.
- [114] T. Wriedt, “Mie theory: a review,” *The Mie theory: Basics and applications*, pp. 53–71, 2012.

- [115] L. Jauffred *et al.*, “Plasmonic heating of nanostructures,” *Chemical reviews*, vol. 119, no. 13, pp. 8087–8130, 2019.
- [116] V. Pustovalov, A. Smetannikov, and V. Zharov, “Photothermal and accompanied phenomena of selective nanophotothermolysis with gold nanoparticles and laser pulses,” *Laser Physics Letters*, vol. 5, no. 11, p. 775, 2008.
- [117] E. Y. Lukianova-Hleb *et al.*, “Selective gene transfection of individual cells in vitro with plasmonic nanobubbles,” *Journal of Controlled Release*, vol. 152, no. 2, pp. 286–293, 2011.
- [118] ———, “Cell-specific transmembrane injection of molecular cargo with gold nanoparticle-generated transient plasmonic nanobubbles,” *Biomaterials*, vol. 33, no. 21, pp. 5441–5450, 2012.
- [119] R. Lachaine, E. Boulais, and M. Meunier, “From thermo-to plasma-mediated ultrafast laser-induced plasmonic nanobubbles,” *Acs Photonics*, vol. 1, no. 4, pp. 331–336, 2014.
- [120] A. Vogel *et al.*, “Mechanisms of femtosecond laser nanosurgery of cells and tissues,” *Applied physics B*, vol. 81, pp. 1015–1047, 2005.
- [121] A. A. Davis *et al.*, “Optoporation and genetic manipulation of cells using femtosecond laser pulses,” *Biophysical journal*, vol. 105, no. 4, pp. 862–871, 2013.
- [122] P. M. Tiwari *et al.*, “Functionalized gold nanoparticles and their biomedical applications,” *Nanomaterials*, vol. 1, no. 1, pp. 31–63, 2011.
- [123] C. Darvot, P. Hardy, and M. Meunier, “Laser-induced plasmon-mediated treatment of retinoblastoma in viscous vitreous phantom,” *Journal of Biophotonics*, vol. 12, no. 11, p. e201900193, 2019.
- [124] N. Katchinskiy *et al.*, “Anti-epcam gold nanorods and femtosecond laser pulses for targeted lysis of retinoblastoma,” *Advanced Therapeutics*, vol. 1, no. 1, p. 1800009, 2018.
- [125] Z. Sharif and W. Sharif, “Corneal neovascularization: updates on pathophysiology, investigations & management,” *Romanian journal of ophthalmology*, vol. 63, no. 1, p. 15, 2019.
- [126] C. Jumelle *et al.*, “Delivery of molecules into human corneal endothelial cells by carbon nanoparticles activated by femtosecond laser,” *PloS one*, vol. 10, no. 7, p. e0132023, 2015.

- [127] N. Pescosolido *et al.*, “Journal of ocular pharmacology and therapeutics,” *JOURNAL OF OCULAR PHARMACOLOGY AND THERAPEUTICS*, 2012.
- [128] J. M. Liebmann *et al.*, “Evolving guidelines for intracameral injection,” *Journal of glaucoma*, vol. 29, pp. S1–S7, 2020.
- [129] P. A. Samsel *et al.*, “A novel method for the induction of experimental glaucoma using magnetic microspheres,” *Investigative ophthalmology & visual science*, vol. 52, no. 3, pp. 1671–1675, 2011.
- [130] J. E. Morgan and J. R. Tribble, “Microbead models in glaucoma,” *Experimental eye research*, vol. 141, pp. 9–14, 2015.
- [131] M. Á. Solinís *et al.*, “Treatment of ocular disorders by gene therapy,” *European Journal of Pharmaceutics and Biopharmaceutics*, vol. 95, pp. 331–342, 2015.
- [132] S. Barabino and M. R. Dana, “Animal models of dry eye: a critical assessment of opportunities and limitations,” *Investigative ophthalmology & visual science*, vol. 45, no. 6, pp. 1641–1646, 2004.
- [133] J. T. Henriksson, A. M. McDermott, and J. P. Bergmanson, “Dimensions and morphology of the cornea in three strains of mice,” *Investigative ophthalmology & visual science*, vol. 50, no. 8, pp. 3648–3654, 2009.
- [134] M. Matthaei *et al.*, “Systematic assessment of microneedle injection into the mouse cornea,” *European journal of medical research*, vol. 17, pp. 1–6, 2012.
- [135] J. T. Henriksson, A. J. Bron, and J. P. Bergmanson, “An explanation for the central to peripheral thickness variation in the mouse cornea,” *Clinical & experimental ophthalmology*, vol. 40, no. 2, pp. 174–181, 2012.
- [136] D. R. Larson *et al.*, “Anterior chamber depth in mice is controlled by several quantitative trait loci,” *Plos one*, vol. 18, no. 8, p. e0286897, 2023.
- [137] H. Yüksel *et al.*, “Anterior segment parameters of rabbits with rotating scheimpflug camera,” *Veterinary ophthalmology*, vol. 18, no. 3, pp. 210–213, 2015.
- [138] G. Bozkir *et al.*, “Measurements of axial length and radius of corneal curvature in the rabbit eye,” *Acta Medica Okayama*, vol. 51, no. 1, pp. 9–11, 1997.
- [139] X. Wang and Q. Wu, “Normal corneal thickness measurements in pigmented rabbits using spectral-domain anterior segment optical coherence tomography,” *Veterinary ophthalmology*, vol. 16, no. 2, pp. 130–134, 2013.

- [140] J. P. Bergmanson, A. R. Burns, and M. K. Walker, “Central versus peripheral thickness in the human cornea explained,” *Contact Lens and Anterior Eye*, vol. 47, no. 3, p. 102165, 2024.
- [141] V. Bhardwaj and G. P. Rajeshbhai, “Axial length, anterior chamber depth-a study in different age groups and refractive errors,” *Journal of clinical and diagnostic research: JCDR*, vol. 7, no. 10, p. 2211, 2013.
- [142] Hamilton needle gauge chart. [Online]. Available: <https://www.hamiltoncompany.com/laboratory-products/needles-knowledge/needle-gauge-chart>
- [143] M. K. Ko *et al.*, “Feedback-controlled constant-pressure anterior chamber perfusion in live mice,” *Molecular vision*, vol. 20, p. 163, 2014.
- [144] Y. A. Ito *et al.*, “A magnetic microbead occlusion model to induce ocular hypertension-dependent glaucoma in mice,” *JoVE (Journal of visualized experiments)*, no. 109, p. e53731, 2016.
- [145] S. Jiang *et al.*, “Experimental study of needle–tissue interaction forces: effect of needle geometries, insertion methods and tissue characteristics,” *Journal of biomechanics*, vol. 47, no. 13, pp. 3344–3353, 2014.
- [146] L. Hirsch *et al.*, “Impact of a modified needle tip geometry on penetration force as well as acceptability, preference, and perceived pain in subjects with diabetes,” *Journal of diabetes science and technology*, vol. 6, no. 2, pp. 328–335, 2012.
- [147] M. G. Jushiddi *et al.*, “Bevel angle study of flexible hollow needle insertion into biological mimetic soft-gel: Simulation and experimental validation,” *Journal of the mechanical behavior of biomedical materials*, vol. 111, p. 103896, 2020.
- [148] A. Matthews *et al.*, “Indentation and needle insertion properties of the human eye,” *Eye*, vol. 28, no. 7, pp. 880–887, 2014.
- [149] O. O’Donnell *et al.*, “Time to consider blunt needles for implant surgery? a systematic review and meta-analysis shows that blunt suture needles reduce glove perforation,” *the surgeon*, 2023.
- [150] J. E. Heavner *et al.*, “Sharp versus blunt needle: a comparative study of penetration of internal structures and bleeding in dogs,” *Pain Practice*, vol. 3, no. 3, pp. 226–231, 2003.

- [151] D. S. Lam *et al.*, “Efficacy and safety of immediate anterior chamber paracentesis in the treatment of acute primary angle-closure glaucoma: a pilot study,” *Ophthalmology*, vol. 109, no. 1, pp. 64–70, 2002.
- [152] A. Nguyen and C. L. Kraus, “Surgical steps,” *Pediatric Cataract Surgery and IOL Implantation: A Case-Based Guide*, pp. 89–104, 2020.
- [153] S.-W. D. Tsen *et al.*, “Femtosecond laser treatment enhances dna transfection efficiency in vivo,” *Journal of biomedical science*, vol. 16, pp. 1–7, 2009.
- [154] S. Batabyal *et al.*, “Laser-assisted targeted gene delivery to degenerated retina improves retinal function,” *Journal of biophotonics*, vol. 14, no. 1, p. e202000234, 2021.
- [155] J. A. Brydson, *Plastics materials*, 7th ed. Oxford, UK: Butterworth-Heinemann, 1999.
- [156] F. Masse *et al.*, “Gold nanoparticles in ophthalmology,” *Medicinal research reviews*, vol. 39, no. 1, pp. 302–327, 2019.
- [157] A. Sani, C. Cao, and D. Cui, “Toxicity of gold nanoparticles (aunps): A review,” *Biochemistry and biophysics reports*, vol. 26, p. 100991, 2021.
- [158] É. Boulais, R. Lachaine, and M. Meunier, “Plasma mediated off-resonance plasmonic enhanced ultrafast laser-induced nanocavitation,” *Nano letters*, vol. 12, no. 9, pp. 4763–4769, 2012.
- [159] R. Lachaine *et al.*, “Rational design of plasmonic nanoparticles for enhanced cavitation and cell perforation,” *Nano letters*, vol. 16, no. 5, pp. 3187–3194, 2016.
- [160] C. Darviot *et al.*, “Multiplexed immunolabelling of cancer using bioconjugated plasmonic gold–silver alloy nanoparticles,” *Nanoscale Advances*, vol. 6, no. 17, pp. 4385–4393, 2024.
- [161] N. Okumura *et al.*, “Cell surface markers of functional phenotypic corneal endothelial cells,” *Investigative ophthalmology & visual science*, vol. 55, no. 11, pp. 7610–7618, 2014.
- [162] S. Lakshmanan *et al.*, “Physical energy for drug delivery; poration, concentration and activation,” *Advanced drug delivery reviews*, vol. 71, pp. 98–114, 2014.
- [163] S. Bolte and F. P. Cordelières, “A guided tour into subcellular colocalization analysis in light microscopy,” *Journal of microscopy*, vol. 224, no. 3, pp. 213–232, 2006.

- [164] F. Stracke, I. Rieman, and K. König, “Optical nanoinjection of macromolecules into vital cells,” *Journal of Photochemistry and Photobiology B: Biology*, vol. 81, no. 3, pp. 136–142, 2005.
- [165] J. H. Urcola, M. Hernández, and E. Vecino, “Three experimental glaucoma models in rats: comparison of the effects of intraocular pressure elevation on retinal ganglion cell size and death,” *Experimental eye research*, vol. 83, no. 2, pp. 429–437, 2006.
- [166] J. W. Streilein, J. Y. Niederkorn, and J. A. Shadduck, “Systemic immune unresponsiveness induced in adult mice by anterior chamber presentation of minor histocompatibility antigens,” *The Journal of experimental medicine*, vol. 152, no. 4, pp. 1121–1125, 1980.
- [167] K. P. Ponder and A. Auricchio, “Gene therapy for ocular problems in mucopolysaccharidosis: an experimental and promising approach with benefits in animal models—a review,” *Clinical & Experimental Ophthalmology*, vol. 38, pp. 43–51, 2010.
- [168] E. K. Schneider-Futschik and F. Reyes-Ortega, “Advantages and disadvantages of using magnetic nanoparticles for the treatment of complicated ocular disorders,” *Pharmaceutics*, vol. 13, no. 8, p. 1157, 2021.
- [169] B. E. Koktekir and B. S. Aslan, “Safety of prophylactic intracameral moxifloxacin use in cataract surgery,” *Journal of ocular pharmacology and therapeutics*, vol. 28, no. 3, pp. 278–282, 2012.
- [170] J. M. Liebmann *et al.*, “Evolving guidelines for intracameral injection,” *Journal of glaucoma*, vol. 29, pp. S1–S7, 2020.
- [171] N. Mamalis, “Intracameral medication: is it worth the risk?” *Journal of Cataract & Refractive Surgery*, vol. 34, no. 3, pp. 339–340, 2008.
- [172] J. R. Crouch *et al.*, “A velocity-dependent model for needle insertion in soft tissue,” in *Medical Image Computing and Computer-Assisted Intervention—MICCAI 2005: 8th International Conference, Palm Springs, CA, USA, October 26-29, 2005, Proceedings, Part II 8*. Springer, Conference Proceedings, pp. 624–632.
- [173] A. M. Okamura, C. Simone, and M. D. O’leary, “Force modeling for needle insertion into soft tissue,” *IEEE transactions on biomedical engineering*, vol. 51, no. 10, pp. 1707–1716, 2004.
- [174] M. Mahvash and P. E. Dupont, “Mechanics of dynamic needle insertion into a biological material,” *IEEE Transactions on Biomedical Engineering*, vol. 57, no. 4, pp. 934–943, 2009.

- [175] A. Leibinger *et al.*, “Soft tissue phantoms for realistic needle insertion: a comparative study,” *Annals of biomedical engineering*, vol. 44, pp. 2442–2452, 2016.
- [176] A. Frid *et al.*, “New injection recommendations for patients with diabetes,” *Diabetes & metabolism*, vol. 36, pp. S3–S18, 2010.
- [177] L. Heinemann *et al.*, “Needle technology for insulin administration: a century of innovation,” *Journal of Diabetes Science and Technology*, vol. 17, no. 2, pp. 449–457, 2023.
- [178] H. Egekvist, P. Bjerring, and L. Arendt-Nielsen, “Pain and mechanical injury of human skin following needle insertions,” *European journal of pain*, vol. 3, no. 1, pp. 41–49, 1999.
- [179] P. Han *et al.*, “Models of the cutting edge geometry of medical needles with applications to needle design,” *International Journal of Mechanical Sciences*, vol. 65, no. 1, pp. 157–167, 2012.
- [180] S. P. DiMaio and S. E. Salcudean, “Needle insertion modeling and simulation,” *IEEE Transactions on robotics and automation*, vol. 19, no. 5, pp. 864–875, 2003.
- [181] T. Podder *et al.*, “Effects of tip geometry of surgical needles: an assessment of force and deflection,” in *IFMBE Proc*, vol. 11. Citeseer, 2005, pp. 1727–1983.
- [182] Y. Wang *et al.*, “Optimal needle design for minimal insertion force and bevel length,” *Medical Engineering & Physics*, vol. 36, no. 9, pp. 1093–1100, 2014.
- [183] Y. A. Ito *et al.*, “A magnetic microbead occlusion model to induce ocular hypertension-dependent glaucoma in mice,” *JoVE (Journal of Visualized Experiments)*, no. 109, p. e53731, 2016.
- [184] T. Igarashi *et al.*, “Direct comparison of administration routes for aav8-mediated ocular gene therapy,” *Current eye research*, vol. 38, no. 5, pp. 569–577, 2013.
- [185] O. Dratviman-Storobinsky *et al.*, “Effect of subconjunctival and intraocular bevacizumab injection on angiogenic gene expression levels in a mouse model of corneal neovascularization,” *Molecular vision*, vol. 15, p. 2326, 2009.
- [186] C.-H. Lin *et al.*, “A protocol to inject ocular drug implants into mouse eyes,” *STAR protocols*, vol. 3, no. 1, p. 101143, 2022.
- [187] D. J. van Gerwen, J. Dankelman, and J. J. van den Dobbelsteen, “Needle–tissue interaction forces—a survey of experimental data,” *Medical engineering & physics*, vol. 34, no. 6, pp. 665–680, 2012.

- [188] S. Misra *et al.*, “Needle-tissue interaction forces for bevel-tip steerable needles,” in *2008 2nd IEEE RAS & EMBS International Conference on Biomedical Robotics and Biomechatronics*. IEEE, Conference Proceedings, pp. 224–231.
- [189] R. R. Mohan, L. M. Martin, and N. R. Sinha, “Novel insights into gene therapy in the cornea,” *Experimental eye research*, vol. 202, p. 108361, 2021.
- [190] S. Feizi, “Corneal endothelial cell dysfunction: etiologies and management,” *Therapeutic advances in ophthalmology*, vol. 10, p. 2515841418815802, 2018.
- [191] H. Tanaka *et al.*, “Panoramic view of human corneal endothelial cell layer observed by a prototype slit-scanning wide-field contact specular microscope,” *British Journal of Ophthalmology*, vol. 101, no. 5, pp. 655–659, 2017.
- [192] R. Vaiciulienė *et al.*, “Risk factors for fluctuations in corneal endothelial cell density,” *Experimental and Therapeutic Medicine*, vol. 23, no. 2, pp. 1–9, 2022.
- [193] C.-P. Yao *et al.*, “Laser-based gene transfection and gene therapy,” *IEEE transactions on nanobioscience*, vol. 7, no. 2, pp. 111–119, 2008.
- [194] N.-S. Yang, “Gene transfer into mammalian somatic cells in vivo,” *Critical Reviews in Biotechnology*, vol. 12, no. 4, pp. 335–356, 1992.
- [195] R. R. Mohan *et al.*, “Gene therapy in the cornea: 2005–present,” *Progress in retinal and eye research*, vol. 31, no. 1, pp. 43–64, 2012.
- [196] N. Sayed *et al.*, “Gene therapy: Comprehensive overview and therapeutic applications,” *Life sciences*, vol. 294, p. 120375, 2022.
- [197] I. B. Clark *et al.*, “Optoinjection for efficient targeted delivery of a broad range of compounds and macromolecules into diverse cell types,” *Journal of biomedical optics*, vol. 11, no. 1, pp. 014 034–014 034, 2006.
- [198] S. H. Chung and E. Mazur, “Surgical applications of femtosecond lasers,” *Journal of biophotonics*, vol. 2, no. 10, pp. 557–572, 2009.
- [199] R. Xiong *et al.*, “Laser-assisted photoporation: fundamentals, technological advances and applications,” *Advances in Physics: X*, vol. 1, no. 4, pp. 596–620, 2016.
- [200] J. Li and K. Pu, “Development of organic semiconducting materials for deep-tissue optical imaging, phototherapy and photoactivation,” *Chemical Society Reviews*, vol. 48, no. 1, pp. 38–71, 2019.

- [201] A. M. Alkilany and C. J. Murphy, “Toxicity and cellular uptake of gold nanoparticles: what we have learned so far?” *Journal of nanoparticle research*, vol. 12, pp. 2313–2333, 2010.
- [202] H. M. AlGhosain *et al.*, “Systemic toxicity of intravitreally injected gold nanorods in mice: Effects of size, surface conjugation, and post-injection period,” 2024.
- [203] S. A. Bansal *et al.*, “Role of gold nanoparticles in advanced biomedical applications,” *Nanoscale Advances*, vol. 2, no. 9, pp. 3764–3787, 2020.
- [204] M. R. Ali *et al.*, “Efficacy, long-term toxicity, and mechanistic studies of gold nanorods photothermal therapy of cancer in xenograft mice,” *Proceedings of the National Academy of Sciences*, vol. 114, no. 15, pp. E3110–E3118, 2017.
- [205] P. S. Ghosh *et al.*, “Efficient gene delivery vectors by tuning the surface charge density of amino acid-functionalized gold nanoparticles,” *ACS nano*, vol. 2, no. 11, pp. 2213–2218, 2008.
- [206] E. Bergeron *et al.*, “Cell-specific optoporation with near-infrared ultrafast laser and functionalized gold nanoparticles,” *Nanoscale*, vol. 7, no. 42, pp. 17 836–17 847, 2015.
- [207] A. R. Ziefuß *et al.*, “Laser fragmentation of colloidal gold nanoparticles with high-intensity nanosecond pulses is driven by a single-step fragmentation mechanism with a defined educt particle-size threshold,” *The Journal of Physical Chemistry C*, vol. 122, no. 38, pp. 22 125–22 136, 2018.
- [208] S. Di Bucchianico *et al.*, “Cyto-and genotoxicity assessment of gold nanoparticles obtained by laser ablation in a549 lung adenocarcinoma cells,” *Journal of Nanoparticle Research*, vol. 17, pp. 1–14, 2015.
- [209] J. Baumgart *et al.*, “Off-resonance plasmonic enhanced femtosecond laser optoporation and transfection of cancer cells,” *Biomaterials*, vol. 33, no. 7, pp. 2345–2350, 2012.
- [210] É. Boulais, R. Lachaine, and M. Meunier, “Plasma-mediated nanocavitation and photothermal effects in ultrafast laser irradiation of gold nanorods in water,” *The Journal of Physical Chemistry C*, vol. 117, no. 18, pp. 9386–9396, 2013.
- [211] D. G. Ogando *et al.*, “Inducible slc4a11 knockout triggers corneal edema through perturbation of corneal endothelial pump,” *Investigative Ophthalmology & Visual Science*, vol. 62, no. 7, pp. 28–28, 2021.

- [212] B. Jue and D. M. Maurice, “The mechanical properties of the rabbit and human cornea,” *Journal of biomechanics*, vol. 19, no. 10, pp. 847–853, 1986.
- [213] M. Goel *et al.*, “Aqueous humor dynamics: a review,” *The open ophthalmology journal*, vol. 4, p. 52, 2010.
- [214] L. Hoffart *et al.*, “Surface ablation of corneal stroma with few-cycle laser pulses at 800 nm,” *Optics Express*, vol. 19, no. 1, pp. 230–240, 2010.
- [215] S. Arba-Mosquera and T. Hollerbach, “Ablation resolution in laser corneal refractive surgery: the dual fluence concept of the amaris platform,” *Advances in Optical Technologies*, vol. 2010, no. 1, p. 538541, 2010.
- [216] G. Girard *et al.*, “Femtosecond laser ablation thresholds for cornea and transparent materials,” *Investigative Ophthalmology & Visual Science*, vol. 45, no. 13, pp. 2920–2920, 2004.
- [217] M. S. Sidhu *et al.*, “Femtosecond laser-assisted selective reduction of neovascularization in rat cornea,” *Lasers in Medical Science*, vol. 29, pp. 1417–1427, 2014.
- [218] S. Patskovsky, M. Qi, and M. Meunier, “Single point single-cell nanoparticle mediated pulsed laser optoporation,” *Analyst*, vol. 145, no. 2, pp. 523–529, 2020.
- [219] S. Park *et al.*, “Protocol for vital dye staining of corneal endothelial cells,” *Cornea*, vol. 31, no. 12, pp. 1476–1479, 2012.
- [220] M. Yoshihara *et al.*, “Discovery of molecular markers to discriminate corneal endothelial cells in the human body,” *PLoS One*, vol. 10, no. 3, p. e0117581, 2015.

APPENDIX A SUPPLEMENTARY MATERIAL FOR OPTIMIZATION OF INTRACAMERAL INJECTIONS IN THE MOUSE EYE MODEL

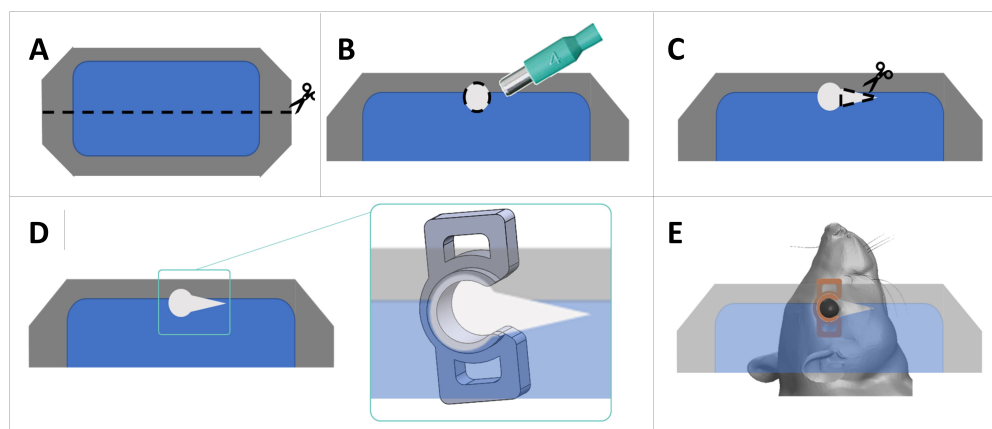


Figure A.1 Mouse eye globe immobilization. (A) A Tegaderm was cut in two, (B) a 4 mm hole was made for placing the ocular globe, and (C) a small triangle was cut to facilitate the access to the needle. (D) The Tegaderm was then placed on top of the 3D-printed eye holder. (E) The holder and Tegaderm can be placed over the periocular region of the mouse, in line with the eye.

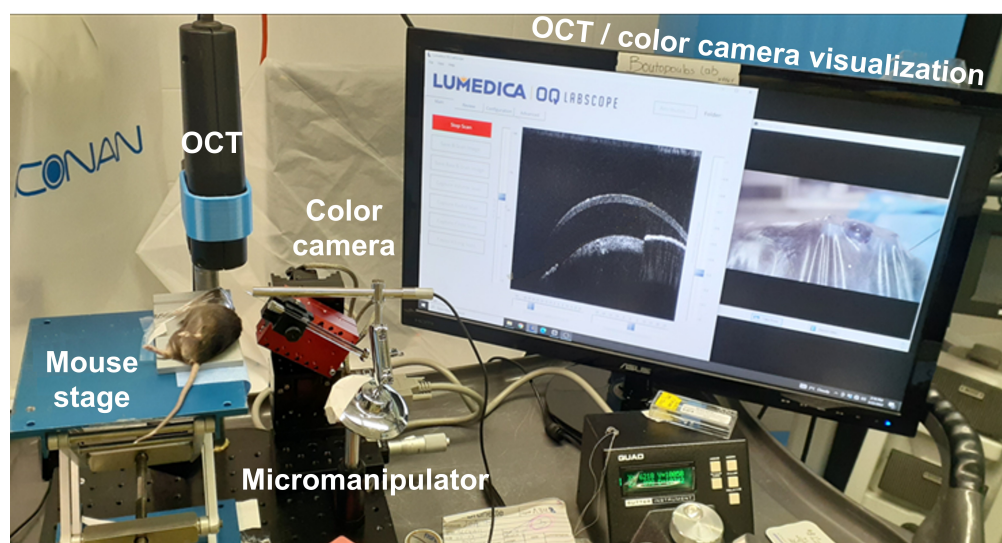


Figure A.2 Montage used for OCT and color camera monitoring of injections. The mouse is positioned on a stage to align the head near the OCT focal point, with fine adjustments made using the OCT support. The needle is mounted on the micromanipulator close to the eye, with its angle adjusted parallel to the limbus. The color camera is placed perpendicular to the OCT axis, allowing simultaneous visualization of both images to monitor the alignment and the injection.

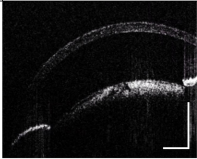
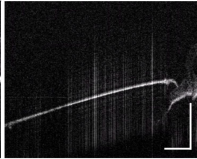
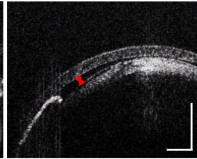


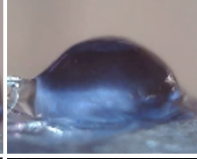
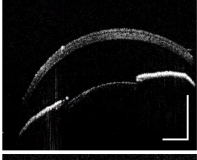
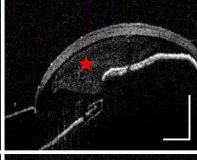
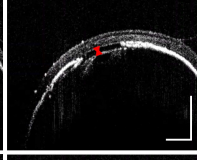
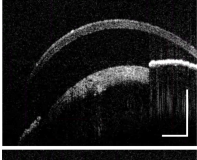
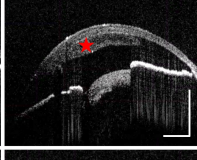
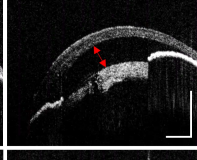
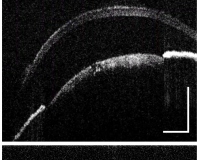
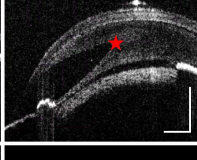
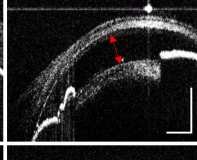
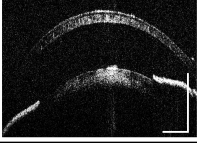
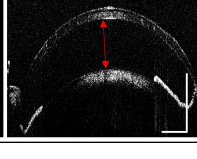
ACD (mean \pm SEM μm)	Before (BI)	During (DI)	After injection (AI)
31 G BI: 465 ± 29 AI: 187 ± 79			
Color Camera			
33 G BI: 521 ± 15 AI: 289 ± 102			
34 G BI: 505 ± 26 AI: 278 ± 67			
35 G BI: 423 ± 16 AI: 381 ± 34			
35 G blunt BI: 458 ± 11 AI: 473 ± 24		No image taken during injection with blunt needles	

Figure A.3 Anterior chamber imaging during injection. Simultaneous visualization by OCT and color camera of the ACD before (BI; Column 2), during (DI; Column 3), and after (AI; Column 4) injection. Needle gauge and ACD are detailed in column 1. Eyes were injected with $0.5 \mu\text{L}$ of OCT contrast agent (indicated with a star) in procedures involving a sharp needle and $0.5 \mu\text{L}$ of a fluorescein-stained solution in those involving a blunt needle. The double-headed arrows show the AC after injection. For 31 G, image acquisition during injection was prevented by the large diameter ($220 \mu\text{m}$) needle deforming and pushing the globe out of the OCT field, as also illustrated by the color photos on the third row. For 33 G, iris and lens damage resulted in the loss of clear boundaries that prevented ACD measurements. In the case of blunt needle tests, the injected fluorescein was not visible with the OCT, nevertheless, ACD images taken before and after injection demonstrated the absence of leakage using this technique, resulting in an AC deeper after than before injection. SEM: Standard error of the mean. Scale bar: $500 \mu\text{m}$ for all images.

APPENDIX B SUPPLEMENTARY MATERIAL FOR FEMTOSECOND LASER GOLD NANOPARTICLE-MEDIATED *EX VIVO* MRNA DELIVERY WITH HIGH SPECIFICITY IN CORNEAL ENDOTHELIAL CELLS

Murine eyes enucleation and corneal dissection. The eyes were enucleated using fine curved forceps (UZ-07387-12, Cole-Parmer, Illinois, US) gently pushing the periocular region protruding the eye for its isolation. Subsequently, each mouse eye was stabilized by grasping the sclera with curved forceps, followed by dissecting the cornea with 6 mm straight Vannas capsulotomy scissors (E3386, Storz Instruments, Bausch + Lomb, Rochester, US). An incision was carefully made along the limbal level, cutting small sections of the cornea incrementally to prevent tissue deformation that could lead to corneal tissue deformation or wrinkles, ultimately affecting cell viability.

Fluorescence images for murine CECs viability at different fluence values. Figure B.1 shows Calcein-AM assessment for viability including an example of the ocular globe condition 48 hours after irradiation. The viability percentage (mean \pm SD for $n=3$) is shown in the upper right corner of the Calcein-AM images for each irradiation condition. At 200 mJ/cm², the bubbles formed due to laser interaction within the aqueous environment can be visualized from the full globe picture, anticipating cell damage after the incubation period.

Fluorescence images for murine CEC transfection at different fluence values. Figure B.2 shows internalization and thus transfection using Cy3-mRNA. An example of the ocular globe condition 48 hours after irradiation for each fluence condition is presented. The transfection percentage (mean \pm SD for $n=3$) is shown in the upper right corner of the Cy3-mRNA images for each irradiation condition.

3D design of holders for mouse and rabbit eyes. Different holders were designed to improve the positioning for incubation and irradiation of murine and rabbit eyes. Three different designs were adapted for this study. Two different holders were designed for mice. The first holder followed the curvature radius of the cornea (1.4 mm) for incubation of AuNPs (B.3A). Nevertheless, to improve the grip when holding the eye during irradiation, a second holder was designed where only lateral walls were holding the sample, avoiding the rolling of the eye ball during laser treatment (B.3B). Conversely, for rabbit samples, one holder was enough to keep the curvature radius (7.26 mm) during incubation and subsequently perform irradiation as shown in Figure B.3C.

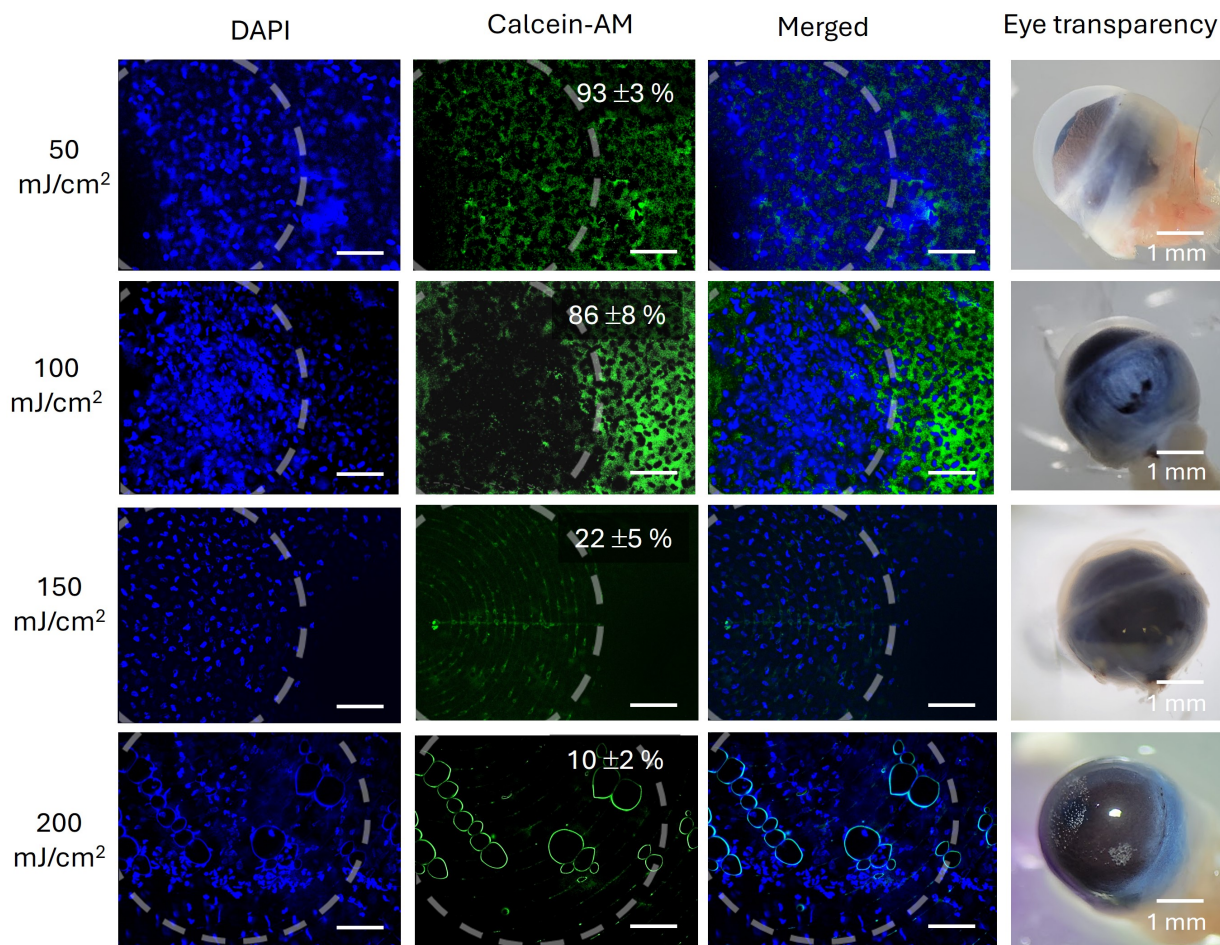


Figure B.1 Murine CEC viability 48 hour post-irradiation. The first column indicates the fluence value for each row. Fluorescent images show the cell nuclei in blue (DAPI) with the corresponding green counterpart for alive cells (Calcein-AM). Merged images can be visualized along with transparent corneas incubated for 48 hours at 37°C and 5% CO₂. The scale bar corresponds to 100 μ m otherwise indicated.

Rabbit eyes enucleation and corneal dissection. A lateral canthotomy incision was made in the lateral canthus of the eye with Steven's tenotomy scissors (E3562, Storz Ophthalmic instruments, Missouri US). Subsequently, an incision was made in the bulbar conjunctiva to cut the rectus muscle followed by the upper and lower muscles, an enucleation spoon was utilized to hold the eye and cut the optic nerve. Following enucleation, the eyes were promptly immersed in balanced salt solution (65079550, BSS, Alcon, Mississauga, Canada) for rinsing and moisture retention. Cornea dissection was performed by decontamination with povidone iodine 0.1% for 15 minutes followed by BSS washing. The excess muscles and tissues surrounding the ocular globe were first removed. An incision in the limbus was made using a dual bevel 1 mm angled knife (8065921541, Alcon, Geneva, Switzerland) while hold-

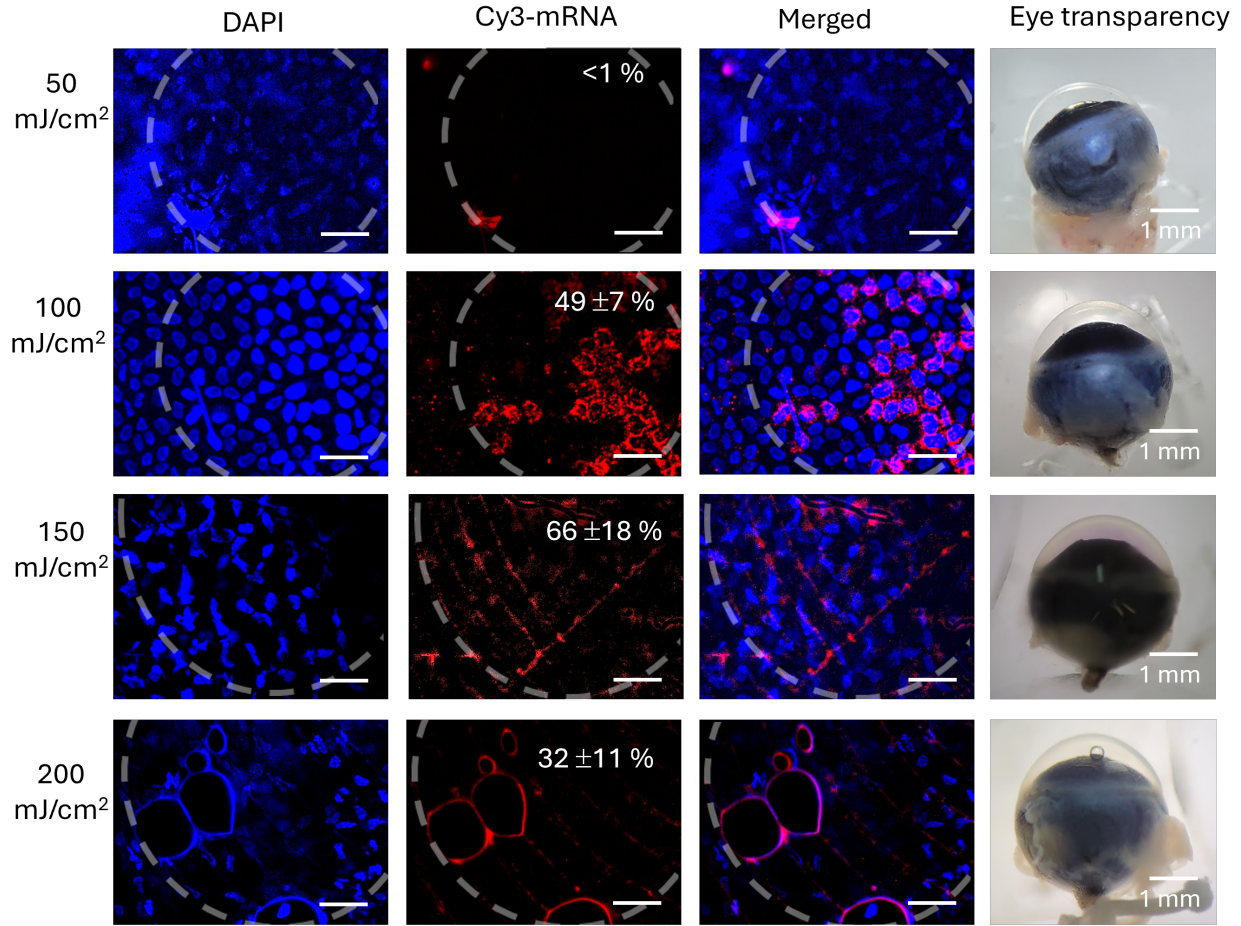


Figure B.2 Murine CEC transfection 48 hour post-irradiation. The first column indicates the fluence value for each row. Fluorescent images show the cell nuclei in blue (DAPI) with the corresponding red counterpart for transfected cells (Cy3-mRNA). Merged images can be visualized along with transparent corneas incubated for 48 hours at 37°C and 5% CO₂. The scale bar corresponds to 50 μ m otherwise indicated.

ing the sclera with 0.5 mm suturing forceps (E1798, Castroviejo, Storz Instruments, Bausch + Lomb, Rochester, US).

Curved corneal scissors (E3220, Castroviejo, Storz Instruments, Bausch + Lomb, Rochester, US) were introduced to cut small sections along the periphery of the cornea, keeping the forceps and scissors close to avoid the deformation or folding of the tissue. The posterior part of the eye was gently separated from the cornea. The iris was removed from the cornea using forceps, maintaining close proximity to prevent tissue deformation. Throughout the procedure, the cornea remained immersed in BSS.

Fluorescence images for rabbit CEC viability at different fluence values. Figure

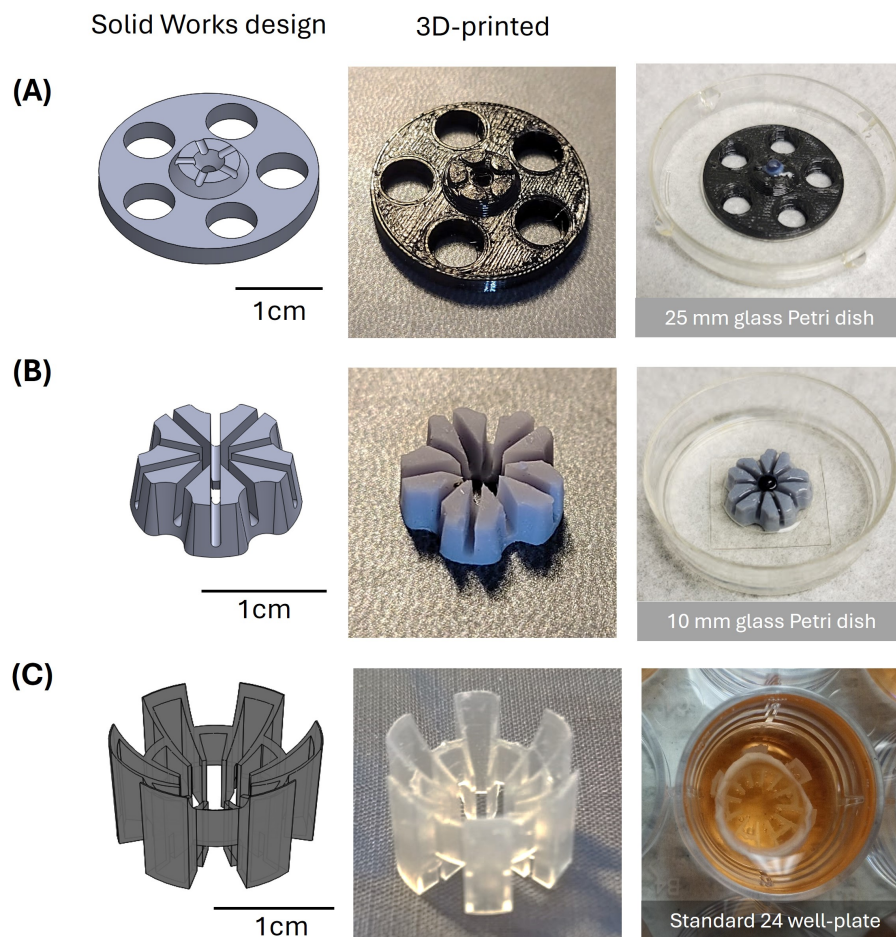


Figure B.3 3D design for rabbit and mouse eye holders. **(A)** Rabbit eye holder for incubation and irradiation. **(B)** Mouse eye holder for incubation post-injection. **(C)** Mouse eye holder for irradiation and incubation post-irradiation.

B.4 illustrates the viability percentage per fluence value. The first column shows the irradiation condition. Cell nuclei are shown in blue (DAPI) with the corresponding counterpart for alive cells in green (Calcein-AM). The viability percentage (mean \pm SD for $n=3$) is shown in the upper right corner of the Calcein-AM images. The dotted line illustrates the irradiation area. More than 70 % of cells remained alive after irradiation and manipulation of rabbit corneas for fluences up to 200 mJ/cm². Detachment of endothelial cells is reported when exposed at 250 mJ/cm². Corneas were incubated for 48 hours in Opti-MEM at 37°C and 5% CO₂.

Fluorescence images for rabbit CEC uptake at different fluence values. Figure B.5 illustrates the uptake percentage per fluence value. The first column shows the irradiation condition. Cell nuclei are shown in blue (DAPI) with the corresponding uptake 48 hours post-

irradiation in red (PI). The internalization percentage (mean \pm SD for n=3) is shown in the upper right corner of the PI images (third column). The dotted line illustrates the irradiation area. Cell uptake resulted more efficient when irradiated at 200 mJ/cm². In contrast, for irradiation at 250 mJ/cm², the pitch size was increased to 50 μ m to reduce energy exposure in CECs as higher energy levels lead to cellular detachment and subsequent decrease in cell viability. Corneas were incubated for 48 hours in Opti-MEM at 37 °C and 5% CO₂ before imaging.

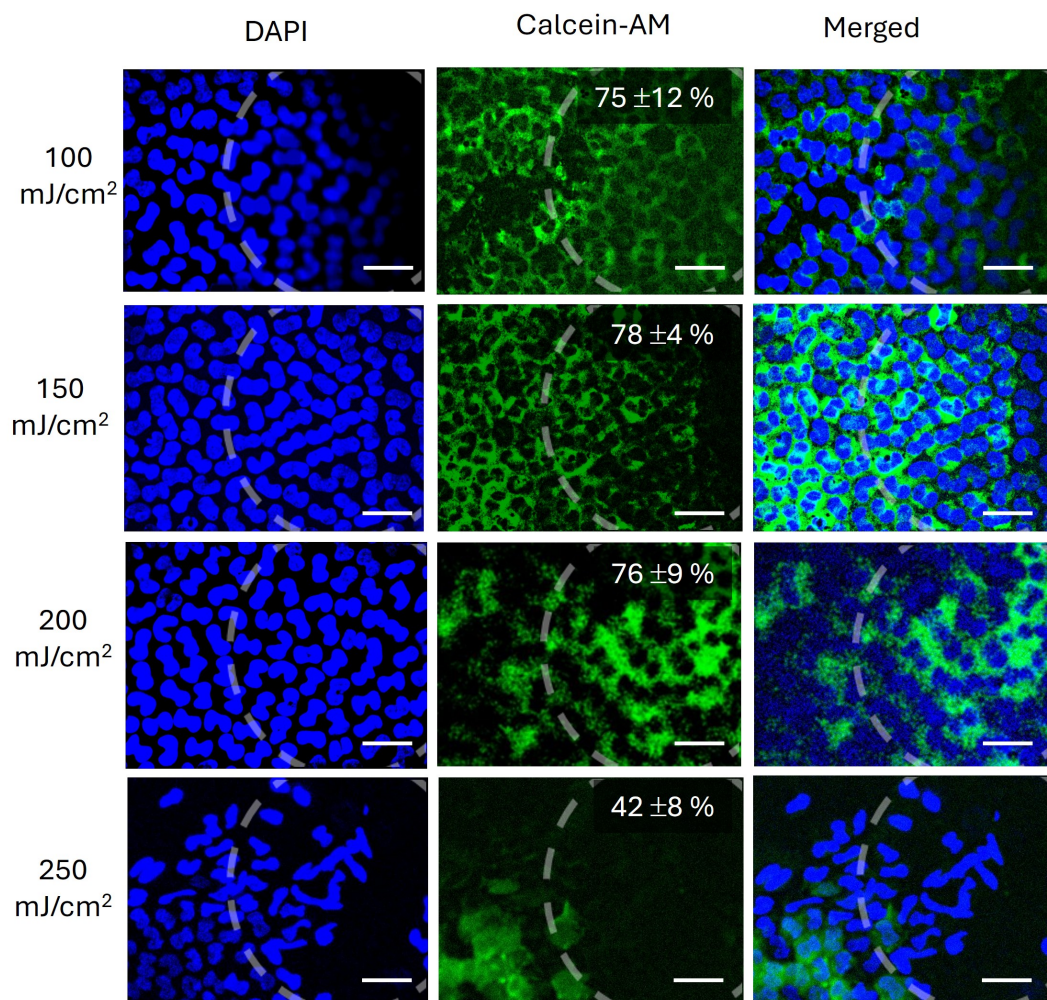


Figure B.4 Rabbit CEC fluorophore uptake 48 hour post-irradiation. The first column indicates the fluence value for each row. Fluorescent images show cell nuclei in blue (DAPI) with the corresponding viability stained in green with Calcein-AM. Merged images can be visualized along with dotted lines indicating laser irradiation areas. The scale bar corresponds to 50 μm .

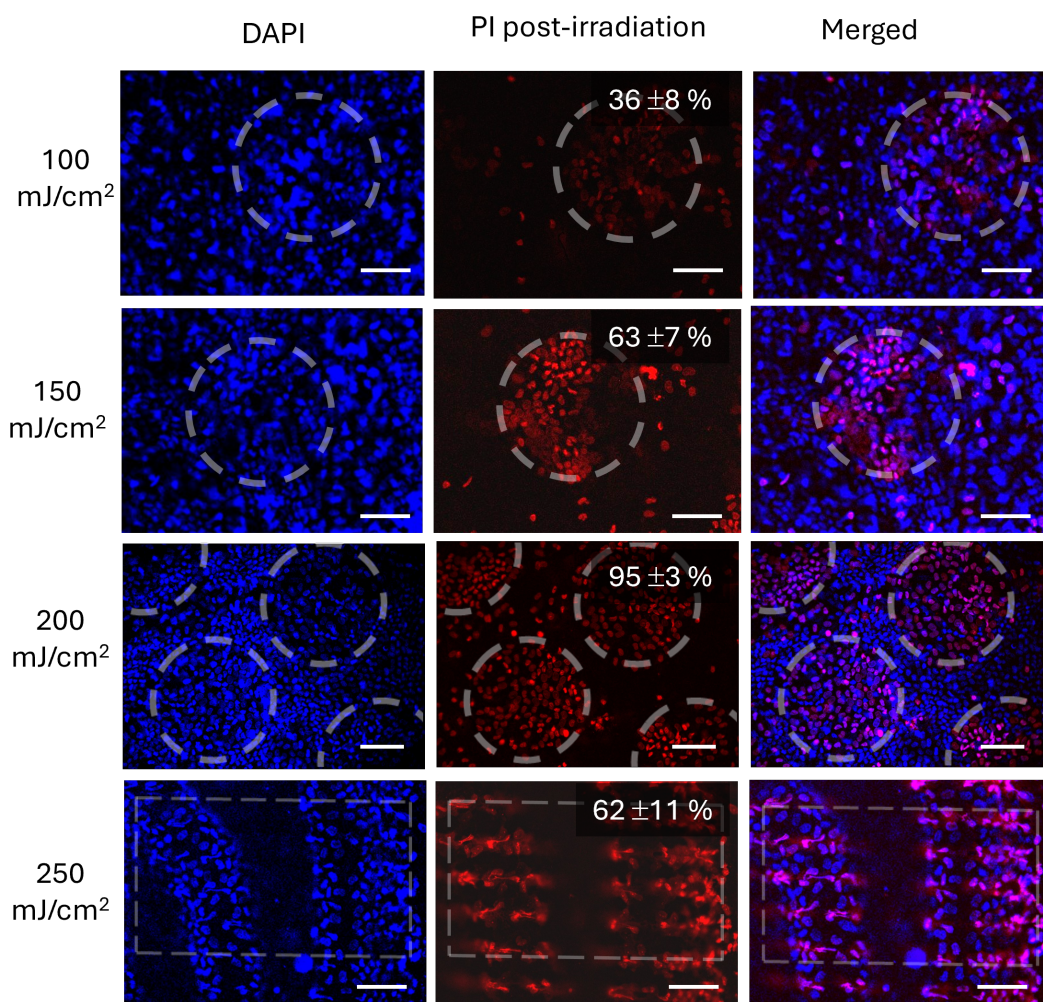


Figure B.5 Rabbit CEC fluorophore uptake 48 hour post-irradiation. The first column indicates the fluence value for each row. Fluorescent images show cell nuclei in blue (DAPI) with the corresponding uptake in red (PI). Merged images can be visualized along with dotted lines indicating laser irradiation areas. The scale bar corresponds to 100 μm .

APPENDIX C ARTICLE 2: DYNAMIC MULTISPECTRAL DETECTION OF BACTERIA WITH NANOPLASMONIC MARKERS

This paper was published in the journal *Nanoscale* from the Royal Society of Chemistry on December 31st 2022. A promising analytical method for detecting the presence of bacteria has been published as part of a side research project. This technique utilizes the optical properties and dynamics of plasmonic markers when attached to pathogens. Authors: Jennyfer Zapata-Farfan,¹ Morteza Hasanzadeh Kafshgari,¹ Sergiy Patskovsky,¹ and Michel Meunier.¹

¹ Department of Engineering Physics, Polytechnique Montréal, Montréal, Québec, H3C 3A7, Canada.

The author of this thesis and first author of the paper, Jennyfer Zapata-Farfan, performed the conception and improvement of the experimental setup, imaging, data analysis and article writing. Morteza H. Kafshgari, participated in part of the experiments, Sergiy Patskovsky, and Michel Meunier participated in the discussions and revision of the text.




Abstract

Culture-based diagnosis of bacterial diseases is a time-consuming technique that can lead not only to antibiotic resistance or bacterial mutation but also to fast-spreading diseases. Such mutations contribute to the fast deterioration of the patient's health and in some cases the death depending on the complexity of the infection. There is great interest in developing widely available molecular-level diagnostics that provide accurate and rapid diagnosis at the individual level and that do not require sophisticated analysis or expensive equipment. Here, we present a promising analytical approach to detect the presence of pathogenic bacteria based on their dynamic properties enhanced with nanoplasmonic biomarkers. These markers have shown greater photostability and biocompatibility compared to fluorescent markers and quantum dots, and serve as both a selective marker and an amplifying agent in optical biomedical detection. We show that a simple dark-field side-illumination technique can provide sufficiently high-contrast dynamic images of individual plasmonic nanoparticles attached to *Escherichia coli* (*E. coli*) for multiplex biodetection. Combined with numerical dynamic filtering, our proposed system shows great potential for the deployment of portable commercial devices for rapid diagnostic tests available to physicians in emergency departments, clinics and public hospitals as point-of-care devices.

PAPER

[View Article Online](#)
[View Journal](#) | [View Issue](#)
Cite this: *Nanoscale*, 2023, **15**, 3309

Dynamic multispectral detection of bacteria with nanoplasmonic markers†

 Jennyfer Zapata-Farfan, , Morteza Hasanzadeh Kafshgari, Sergiy Patskovsky  and Michel Meunier *

Culture-based diagnosis of bacterial diseases is a time-consuming technique that can lead not only to antibiotic resistance or bacterial mutation but also to fast-spreading diseases. Such mutations contribute to the fast deterioration of the patient's health and in some cases the death depending on the complexity of the infection. There is great interest in developing widely available molecular-level diagnostics that provide accurate and rapid diagnosis at the individual level and that do not require sophisticated analysis or expensive equipment. Here, we present a promising analytical approach to detect the presence of pathogenic bacteria based on their dynamic properties enhanced with nanoplasmonic biomarkers. These markers have shown greater photostability and biocompatibility compared to fluorescent markers and quantum dots, and serve as both a selective marker and an amplifying agent in optical biomedical detection. We show that a simple dark-field side-illumination technique can provide sufficiently high-contrast dynamic images of individual plasmonic nanoparticles attached to *Escherichia coli* (*E. coli*) for multiplex biodetection. Combined with numerical dynamic filtering, our proposed system shows great potential for the deployment of portable commercial devices for rapid diagnostic tests available to physicians in emergency departments, clinics and public hospitals as point-of-care devices.

 Received 1st June 2022,
 Accepted 31st December 2022

DOI: 10.1039/d2nr03047k

rsc.li/nanoscale

1. Introduction

The prevalence of infectious pathogens such as viruses and antibiotic-resistant bacteria, as the most paramount public health concern is increasing at an alarming rate.¹ The lack of efficient antiviral therapeutics for treating viral infections, such as coronaviruses (*e.g.*, SARS-CoV)² and effective drugs for managing antibiotic-resistant bacteria drastically affects normal human habits.^{3,4} These growing crises are derived from a series of unhealthy lifestyles, including overconsumption, inappropriate prescription, extensive agricultural use of antibiotics,^{5,6} and limited resources and technologies for the development of effective antiviral therapeutics due to scientific, economic and regulatory obstacles.⁷ To address this challenge, healthy lifestyles, elaborated medical policy workflows, and improved point-of-care diagnostic approaches must be implemented, with the aim of achieving a manageable health and economic burden on the health care system and patients.^{8–10} The necessity of a rapid, accurate, and reliable detection strategy for different infectious pathogens (*e.g.*, viral

and antibiotic-resistant bacterial strains) must therefore be overcome.

To detect pathogens in biofluids,¹¹ microbiological, immunological,¹² and polymerase chain reaction (PCR) methods¹³ are commonly used in clinics, despite their complexity and expensive multi-step processes. For example, fluorophore-labelled pathogenic strains can be detected, counted, and examined by using flow cytometry¹⁴ and fluorescence imaging.¹⁵ To improve the detection accuracy and sensitivity of Raman¹⁶ and fluorescence¹⁷ biosensors functional nanomaterials can be incorporated that work as a contrast agent with an ability to rapidly interact with pathogens *via* a biological component. However, some functional nanomaterials used for fluorescence imaging, such as quantum dots,^{18–20} have shown a range of drawbacks, including short shelf-life, fluorescence instability, toxicity, the need for a complex bio-functionalization procedures.

In contrast, plasmonic nanoprobess such as gold and silver nanoparticles, have emerged as an effective alternative to other biomarkers for the detection of pathogenic organisms.^{21–26} Due to their strong light scattering efficiency and long-term stability (without flickering and photobleaching), such nanomaterials can be used in the development of novel sensing methodology based on the continuous analysis of the free motion of biofunctionalized particles in dynamic biological systems.

Department of Engineering Physics, Polytechnique Montréal, Montréal, Québec, H3C 3A7, Canada. E-mail: michel.meunier@polymtl.ca

† Electronic supplementary information (ESI) available. See DOI: <https://doi.org/10.1039/d2nr03047k>

In this article, we describe the basic concepts of three-dimensional dynamic detection of a plasmonic NP-bacteria complex and present its advantages over a conventional static nanoparticle-enhanced biosensing. We demonstrate the performance of optical darkfield technology for reliable detection and fast-tracking of even single NPs, which can provide a single-cell detection limit. The use of different NPs with different spectral properties will allow the development of multiplex diagnostics and the differentiation of bacteria in a biological solution. In addition, we designed and investigated a simplified optical detection setup based on side-illumination darkfield NPs imaging and discussed its potential applications in two portable schemes for personalized and point-of-care applications. We believe that the presented technology can improve the quality of healthcare and environmental monitoring of infectious microorganisms.

2. Experimental section

2.1. Plasmonic nanoparticles

The performance of multiplexed nanoplasmonic microscopy depends on the optical detection method and the choice of NPs used as markers. In our case, we selected two NPs markers with similar scattering efficiency and for which the spectral position of their resonance peak stays in the detection range of a conventional CMOS camera (400–800 nm). From the optical point of view, the visualization of NPs above 60 nm in diameter is achievable with low magnification, which enables the possibility of reducing the cost and volume of the device. For the proof-of-concept, AuNPs (50 $\mu\text{g mL}^{-1}$, 100 nm in diameter, A11-100-CIT) and AuNRs (60 $\mu\text{g mL}^{-1}$, 40 nm \times 80 nm, A12-40-650-NEG) purchased from Nanopartz (Loveland, CO, U.S.A.) were used. Citrate-capped AuNPs and AuNRs were stored at 4 °C in the dark to minimize photoinduced oxidation. With the appropriate functionalization, the NPs were attached to the body or flagella of the *E. coli*, showing a difference in motility (bacterial dependent). In this case, the change in velocity was used as an indicator of the presence of bacteria in a sample whose volume could be less than 1 mL, as shown in the Results section. The images were taken with a Nikon 60 \times objective (NA = 0.7) and colour CMOS PCO-Panda 4.2 camera (PCO AG, Kelheim, Germany). On the other side, the tracking of the NPs was made by using the software ImageJ (plug-in NanoTrackJ²⁷) taking.

2.2. Preparation of bacteria samples

E. coli strain ATCC 25922 purchased from ATCC (Manassas, VA, U.S.A.) was used in culture-free mode and incubated with functionalized AuNPs. *E. coli* were thawed and resuspended on Trypticase soy broth (TSB) at 37 °C for 24 h, followed by subsequently mixing 50 μL of bacterial cells (at a concentration of 1E6 bacterial cells per mL) with 5 μL of functionalized AuNPs in PBS. After 30 min of incubation, the sample was placed in a custom-made sample holder, consisting of a microscope slide with a double-sided tape (5 μm thickness; purchased from

Nitto, Osaka, Japan) cut as an O-ring and a coverslip to seal the chamber-like sample holder. This simple arrangement was made to facilitate the visualization of the analyte with the side-illumination adaptor. Once the NPs are added to the bacteria, the sample contains free NPs, bacteria, and NPs attached to bacteria.

2.3. Nanoparticle functionalization

In the first stage of the conjugation, 100 nm AuNPs were coated with poly(ethylene glycol) (PEG) purchased from Nanocs (New York, NY, U.S.A.) in order to have a COOH functional group. Subsequently, the EDC/NHS (1-ethyl-3-[3-dimethylamino-propyl]-carbodiimide hydrochloride/*N*-hydroxysuccinimide) protocol is performed to conjugate with the specific antibody.

Our colloidal AuNPs have a concentration of 4.9E9 NPs per mL, which corresponds to the commercial concentration of bare NPs. The number of plasmonic markers regarding the number of bacteria is intended to be in excess so that the probability of attachment is higher.

In this case, the anti-*E. coli* polyclonal antibody (Outer Membrane Protein-A (OmpA) 111120) purchased from Antibody Research (Saint Charles, MO, U.S.A.) was used at a concentration of 1 mg mL⁻¹. After conjugation, the AuNPs were centrifugated and resuspended in Phosphate Buffered Saline (PBS) purchased from Merck KGaA (Darmstadt, Germany) to mix with the *E. coli*. In order to corroborate the presence of the antibody on the surface of the NPs, ultraviolet-visible (UV-VIS) spectra were taken from bare and functionalized NPs, observing an expected slight shift in the plasmonic peak after conjugation as shown in our previous work,²³ and in accordance with the literature.²⁸

2.4. Hyperspectral measurements

A custom-made hyperspectral (HS) camera was used to measure the spectra of the plasmonic nanomaterial. The HS images were taken in a range of 400–700 nm. We observed excellent agreement between the theoretical calculations (Mie Theory) and the manufacturer data of the plasmonic peak of the two different markers that were selected for this work.

3. Results and discussion

3.1. Microscopy visualization of bacteria with plasmonic NPs

A 3D multispectral microscopy platform was built based on an inverted Eclipse Ti microscope (Nikon, Mississauga, ON, Canada) for the dynamic detection of the immunoplasmonic marker-decorated bacteria. The microscopy system was equipped with an oil immersion objective with a magnification of 100 \times and a variable numerical aperture (NA = 0.5–1.3) used for the reflected light microscopy (RLM) method.^{29–31} The microscopy illumination was provided by a standard white light source (Nikon) with a 50 W halogen lamp and a 50/50 beam splitter providing a smooth illumination across the entire operating range (Fig. 1a). A similar halogen lamp source

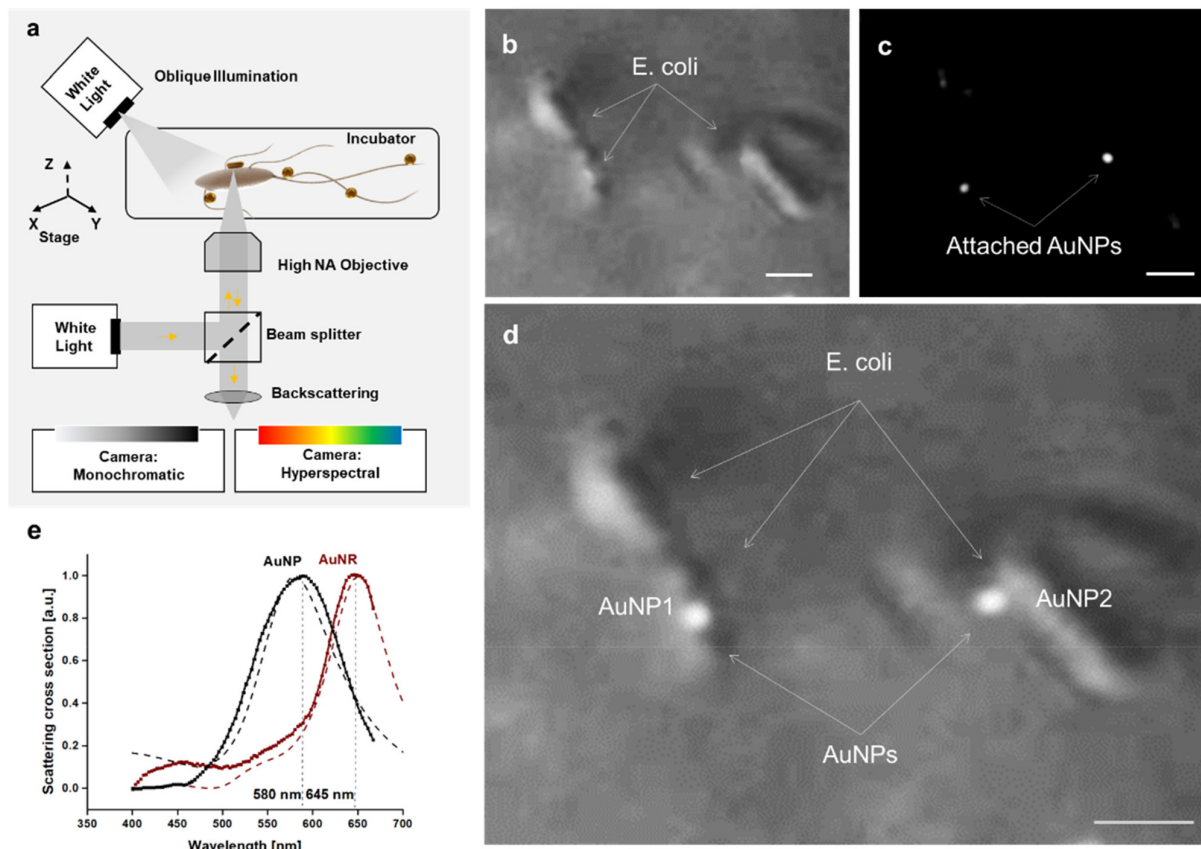


Fig. 1 Platform for plasmonic optical sensor for bioimaging the dynamics of plasmonic NP-decorated bacteria; (a) schematic representation of the RLM optical system based on high NA immersion objective for plasmonic bioimaging with integrated oblique illumination mode for bacteria visualization and hyperspectral camera for NPs multiplexing. (b) Bacteria imaging using oblique illumination mode (plasmonic NPs are invisible); (c) corresponding image of NPs using back reflection mode; (d) *E. coli* visualized with the oblique illumination and backscattering simultaneously using high NA objective (100 \times /1.25); (b–d) Images correspond to three different frames of a video available in the ESI (Video 1, ESI†); (e) scattering cross-section of 100 nm AuNPs and 40 \times 80 nm AuNRs measured with the hyperspectral camera in comparison with Mie Theory calculations (AuNP) and finite element approach (AuNR); solid line: HS measured data, dotted line: simulated response. The scale bars correspond to 1 μ m.

was used for the OLM microscopy. Imaging was done with a fast-monochromatic CMOS camera or a hyperspectral (HS) camera to perform multiplexing when more than one type of plasmonic marker was used. The optimal experimental conditions for samples of a mixture of bacteria and NPs during long-term measurements were provided by a portable incubator (Live Cell Instrument CU-501, Chamlide TC-W, Gyeonggi-do, Republic of Korea) placed on the microscope stage. Accordingly, this 3D multispectral bioimaging platform provided a high-contrast visualization of the plasmonic NPs with fast (up to 50 fps) imaging, high-resolution microscopy for bacteria detection (*E. coli* size range: 500–1000 nm), the possibility of spectral identification and differentiation of plasmonic NPs, as well as the 3D translation stage for analyzing the volume of the sample.

We have prepared a sample with the mixture of *E. coli* bacteria and two different types of plasmonic NPs, AuNPs (50 μ g ml^{−1}, 100 nm in diameter) and AuNRs (60 μ g ml^{−1}, 40 nm \times 80 nm). In the sample, we expect to detect free plasmonic NPs,

free-floating and precipitated bacteria, as well as *E. coli* bacteria decorated with plasmonic markers. Of the various microscopy modes used for bacterial imaging,^{32,33} such as transmission and phase contrast, for this work we selected OIM.³⁴ OIM can be easily combined with other microscopy methods and is achieved by fine-tuning the light transmission angle and adjusting the 100 \times variable lens aperture accordingly. Herein, the best 3D-like image of bacteria was obtained when the objective aperture was adjusted to provide the limit of DF and bright-field microscopy. As shown in Fig. 1b–d, the visualization of bacteria confirms the real-time recognition and spatial tracking of individual bacterial cells, where a frame from a video available in the ESI is shown (Video 1, ESI†).

The detection of dynamic objects is highly dependent on the relationship between the velocity of the entities as well as camera speed and exposure time. Since a wide range of economical and fast CMOS cameras are available (50–600 fps), the dynamic image limitation mainly relates to the exposure time and the intensity of the objects. In this case, the imaging of

plasmonic NPs using RLM with a high numerical aperture objective has provided an intense scattering signal for the plasmonic NPs to enable fast detection, *i.e.*, at 50 fps and exposure time of 15–20 ms. For *E. coli* with attached plasmonic NPs and free plasmonic NPs in the solution (see Video 1, ESI†). By turning off the reflected light illumination and leaving the oblique illumination on, only bacteria will be detected (Fig. 1b).

As shown in the literature, high contrast imaging of plasmonic NPs in a highly diffusive medium can be obtained by using reflected light microscopy (RLM) with a high numerical aperture oil-immersion objective.^{29–31} In Fig. 1c we present an image of the prepared bacteria-NP sample, wherein the high-intensity bright spots correspond to the scattering from plasmonic NPs detected by RLM. This RLM mode of microscopy was found very effective for detecting NPs but provides no information about biological objects in the solution due to the low scattering signal from the cellular membrane.³⁵ Accordingly, the combination of microscopy techniques, such as RLM and OLM, can improve the visualization of the complex system with bacteria and plasmonic NPs (see Fig. 1d).

Two types of plasmonic NPs, AuNPs and AuNRs, were used to validate the feasibility of the plasmonic optical biosensor for reliable NP spectral differentiation and multiplexing. Based on the size and composition-dependent features of plasmonic NPs and the simulation of their optical properties by means of Mie Theory (nanospheres) and finite element approach (nanorods), the theoretical scattering peak of the AuNPs is at 580 nm, while the position of the AuNRs peak is at 650 nm. Such spectral differences of the plasmonic material can be distinguished as different colours in the working solution when looking at the sample under the microscope. Nevertheless, in the case of samples composed of not only plasmonic material but also organic compounds (*i.e.*, bacteria), differentiation methods based on multispectral or hyperspectral techniques are required for accurate identification. For this reason, the optical biosensor is equipped with a hyperspectral camera that uses a continuously variable filter (Delta Optical Thin Film) as a dispersion element to separate the different wavelengths for spectral scanning. The camera provides a fairly fast (<1 min) spectral scan of the sample, and due to the possibility of wide-angle imaging, it allows temporal NPs tracking, generates HS data even for dynamic objects, and exhibits agreement with the theoretical curves for the corresponding AuNPs and AuNRs (Fig. 1e).

3.2. Portable optical setup for dynamic bacteria detection

The development of the optical biosensor for rapid DF imaging has demonstrated the promising potential of plasmonic NPs as selective markers for dynamic detection and differentiation of bacteria. However, traditional microscopy-based optical biosensors, demanding high-power lenses as well as professional operators, are not easily converted to an accessible point-of-care setting for fast and affordable diagnosis. Cost-efficient DF microscopy with the potential for miniaturization can facilitate the visualization of plasmonic NPs with a

sufficient spectral contrast required for multiplex detection. The portable DF imaging method with side-illumination has been developed for dynamic detection of the bacteria-NP complex (Fig. 2a).³⁶ The principle of side-illumination is based on a lateral sample illumination and it is practically implemented by coupling and propagating light in a waveguide through a standard microscope slide with a thickness of 1 mm. The light source is an array of tri-colour light-emitting diodes (LEDs) for RGB illumination.

Recent progress in the miniaturization of high-intensity LEDs allows direct light coupling to microscope slides and the possibility of manual or fast automatic light intensity modulation to enhance the NPs' contrast for diagnostic purposes. In addition, the development of CMOS camera technology facilitates the assembly of a high-speed image detector. The dark-field side-illumination images of bacterial cells with AuNPs (Fig. 2b) and AuNRs (Fig. 2c) mixed in culture media were taken using a Nikon 60× objective (NA = 0.7) and colour CMOS PCO-Panda 4.2 camera. Since plasmonic NPs are easily distinguishable, free and bacteria-attached NPs can be visually differentiated as the objective (60× magnification) provided sufficient resolution to detect individual *E. coli*. RGB illumination combined with colour camera detection can be used for a simplified multispectral differentiation of plasmonic NPs. This method is not as accurate as the HS camera used in traditional microscopy but, it remains possible to spectrally separate at least two independent plasmonic markers as we have presented here, AuNPs and AuNRs.

The DF method provides sufficient contrast to reliably detect NPs even when using low magnification objectives with an estimated NPs contrast of ~7 (4× objective) and ~30 (10× objective) (Fig. 2d). The use of these low-power objectives may limit the visualization of bacteria; however, the scattering of plasmonic markers can be easily detected in a wide field of view. Since the plasmonic material is on the cell membrane of the *E. coli*, this facilitates the use of larger sample volumes and simplifies the optical setup miniaturization.

For multispectral differentiation of NPs, the principle is shown in Fig. 3, the spectral response of the source (LED illumination) is combined with the Bayer filter properties of the colour camera (Fig. 3a) and subsequently multiplied by the scattering properties of the plasmonic markers (Fig. 3b).³⁷ Software assistance can be used to recalibrate and compare the detected intensity of each channel (RGB), thereby providing information on the marker type. The proposed optical biosensor is also able to differentiate several individual NPs bound to a single bacterial cell, creating an array of NPs, thereby providing quantitative detection of bacteria-NPs complexes in the working solution. The dynamic detection of plasmonic markers is a reliable approach permitting a real-time quantitative analysis of alive and moving pathogens compared to fixed or dead biological objects. In this case, live dynamic bacteria can be quantified not only with a single attached NP (Video 2, ESI†), but also with an array of NPs. In the second case (*i.e.*, having an array of NPs) the plasmonic markers need to have not only common dynamics between them but also a

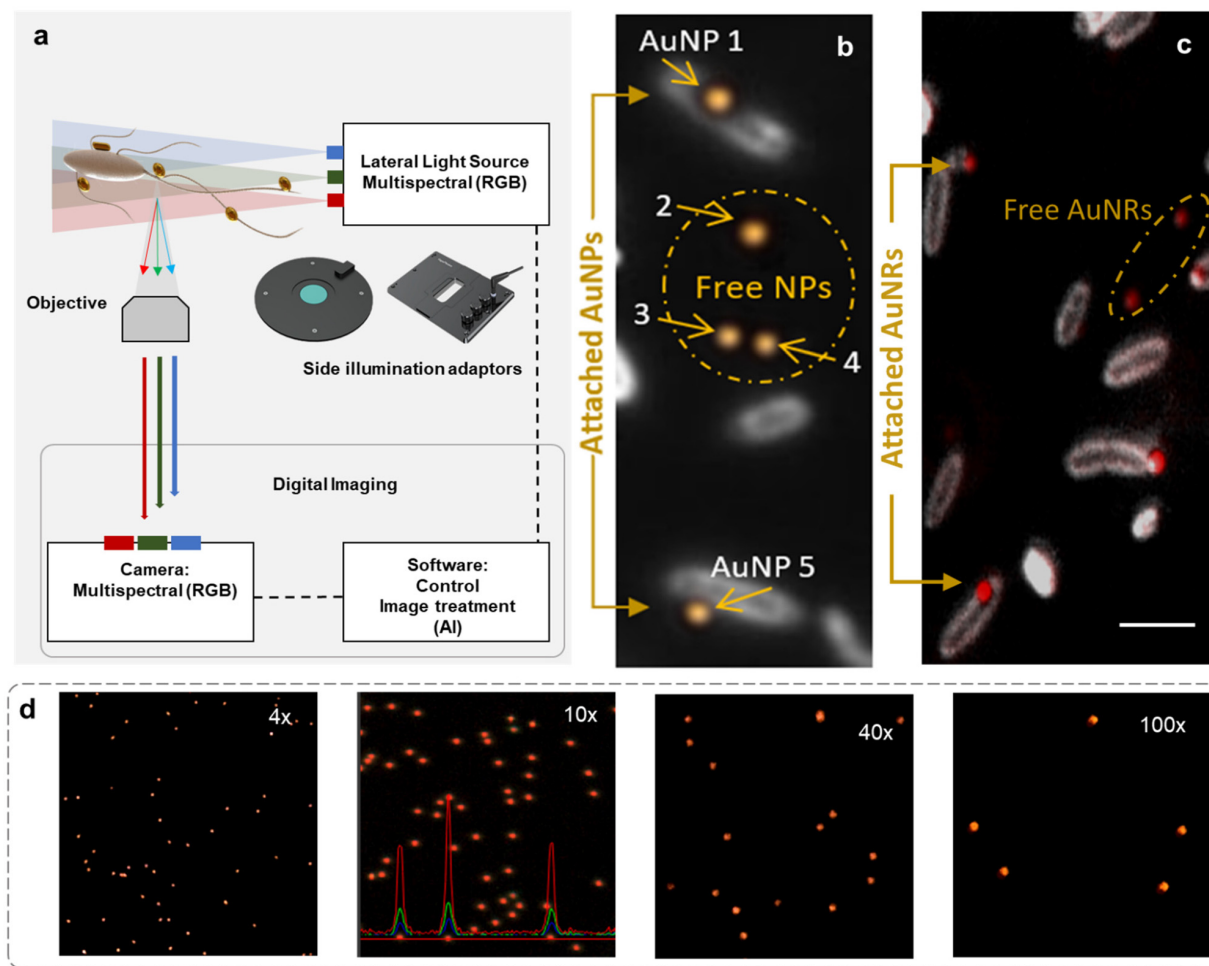


Fig. 2 Side-illumination microscopy for detection of the dynamics of plasmonic NPs-bacteria complex; (a) schematic representation of a portable optical setup with side-illumination darkfield mode and RGB camera for multispectral NPs detection; (b) dark-field image of *E. coli* mixture with 100 nm AuNPs; (c) image of 40 nm \times 80 nm AuNRs attached to *E. coli*; (d) 100 nm diameter AuNPs visualized at different magnifications with the side-illumination adaptor. The scale bar corresponds to 1 μ m (RGB: Red Green Blue; AI = Artificial intelligence).

constant spatial distribution to be considered as a cluster attached to one bacterial cell. The presented device can determine the above-mentioned characteristics in real-time, showing the same distance between NPs along the whole displacement of the *E. coli* (Fig. 4a and b). As an example, we have provided a video of AuNPs bound to *E. coli* flagella (Video 3, ESI†), where the nanomarkers have kept the same distance and dynamic pattern of the target bacteria during the movement compared to Brownian dynamics of free AuNPs.

3.3. Dynamic detection of bacteria with plasmonic markers

Several methods have already been developed for the dynamic characterization of nano- and microparticles. These methods can evaluate whether bacteria are dead or alive, how quickly live bacteria multiply, and how they interact with external stimuli.^{38–40} In addition, certain approaches, including dynamic light scattering (DLS),⁴¹ particle scattering diffusome-

try (PSD)⁴² and nanoparticle tracking analysis (NTA),²⁷ can be adapted for the investigation of bacteria decorated with immunoplasmonic bioprobes.

The DLS technique has been frequently employed; however, it faces the major challenge of distinguishing and tracking individual NPs and arrays, as well as the experimental implementation of multiplex detection. PSD, based on dark field microscopy and particle image velocimetry, has also exhibited limitations for analyzing the diffusivity of dynamic objects undergoing Brownian motion. By contrast, NTA enables the calculation of the size of particles based on their spatial trajectories by means of the particle tracking velocimetry (PTV) method.

To study the dynamics of bacteria-NP complexes, a simple microfluidic measuring cell was fabricated. A conventional microscope slide (25 \times 75 mm) was used as a base, where two holes of 1 mm in diameter were laser-drilled to insert a stain-

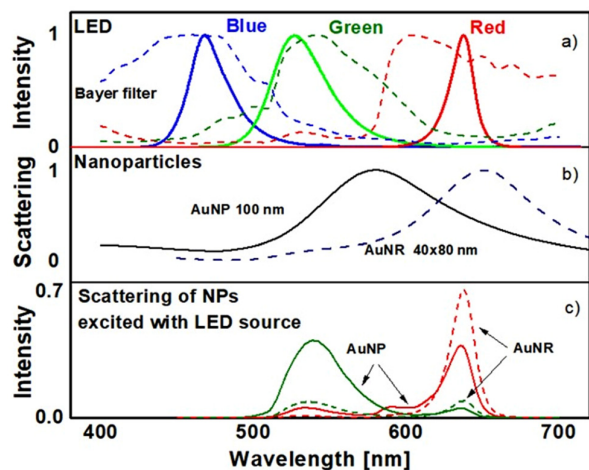


Fig. 3 (a) Spectral specification of the illumination LED (full lines) and colour camera Bayer filter (dashed lines); (b) measured scattering of 100 nm AuNPs (full line) and 40 × 80 nm AuNRs (dashed line); (c) total spectral response detected by the camera for both nanoparticles excited by either the green or red LEDs.

less-steel tube fixed with epoxy glue. A thin spacer (1×5 mm) was laser-cut from a double-sided adhesive tape to place it between the perforated base and a coverslip forming the microfluidic device. To have the optimal volumetric visualization, an adhesive tape of 5 μm in thickness was chosen, which in combination with a 10 \times objective, made possible a volumetric detection without an additional z-scan. As mentioned before, the same microscope slide serves as a waveguide to deliver light coupled with the side-illumination device to the sample.

To demonstrate the NTA method for the tracking spatial movement of plasmonic NPs, a solution of colloidal AuNPs (100 nm in diameter) was introduced into the measuring fluidic cell accompanied by dark-field microscopy (with 60 \times objective) and side-illumination (Fig. 5a, and corresponding Video 3, ESI†). Accordingly, AuNPs with their high scattering intensity are reliable imaging markers that can be used for precise bacteria detection. The integrated image sequences indicate the movement of AuNPs in time (Fig. 5b). By taking advantage of the tracking analysis, the trajectory of individual AuNPs (Fig. 5c) has been obtained and used for calculating the diffusion coefficient and the size of the corresponding tracking object (e.g., individual, arrays, and agglomerates of AuNPs, as well as bacteria decorated with plasmonic probes). As a result,

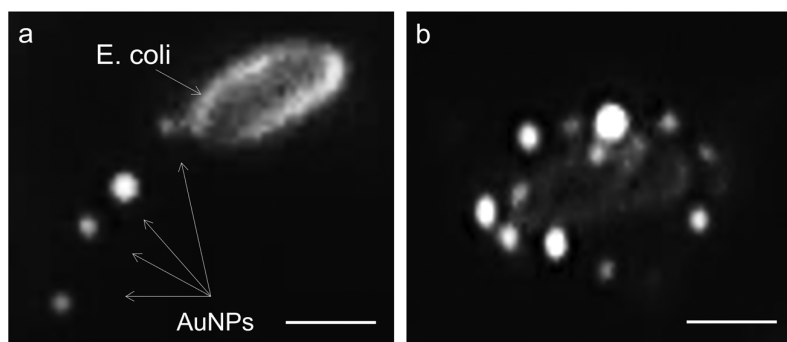


Fig. 4 (a) Dark-field imaging of AuNPs attached to *E. coli* flagella; (b) AuNPs binding the fimbriae of the *E. coli*. The scale bar corresponds to 1 μm .

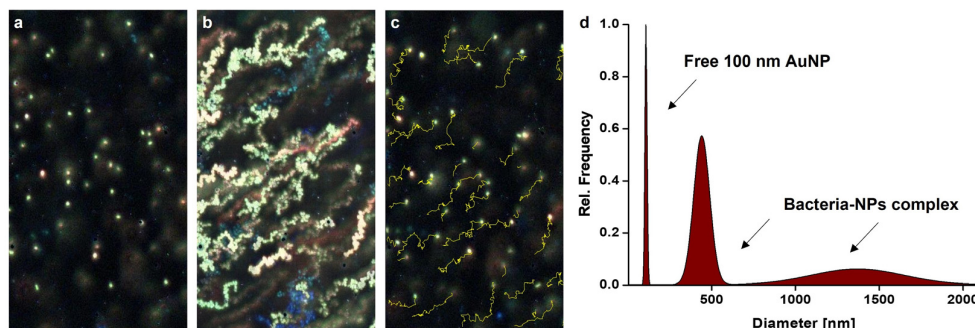


Fig. 5 Dynamic detection of free AuNPs compared to AuNPs-bacteria complex. (a) 100 nm AuNPs visualized with 60 \times objective under dark-field side-illumination device; (b) integrated result of a sequence of NPs in movement; (c) trajectories of single AuNPs performed on ImageJ (plug-in NanoTrackJ¹); (d) relative frequency of occurrence of free AuNPs, and NPs-decorated bacteria.

fast darkfield imaging of dynamic plasmonic NPs, integrated with tracking analysis software, has provided an effective tool for detecting and quantifying not only free AuNPs and bacteria binding AuNPs, but also agglomerations with reduced motility. The relative frequency of occurrence of objects of different sizes with three main dimensional regions is shown in Fig. 5d after examining a mixture of functionalized AuNPs and *E. coli* bacteria. The free AuNPs generate a peak around 100 nm, while two peaks around 500 nm and 1300 nm can be associated with the bacteria, and the obtained distribution follows the accessed bacteria size distribution (microscopy-based analysis) as well as the literature.⁴³ In addition, the developed tracking analysis approach has been able to quantify associated AuNPs with similar dynamics and predict the dynamics of plasmonic NPs bound to the fimbriae and the flagella of the target bacteria. The fimbriae and flagella of static bacteria, settled down on the bottom of the detection surface, can slightly move with the bound plasmonic NPs, and therefore these motions can be dynamically distinguished from free singular and aggregated NPs deposited on the surface.

The high-contrast imaging of NPs obtained by the side-illumination darkfield method also provides adequate microscopy conditions with low phototoxicity for optional long-time observation of bacterial samples. Experimentally, we observed the proliferation of bacteria after continuous LED illumination of the sample. Bacterial cells that were visualized 24 hours after exposure to our lighting system showed no abnormalities in concentration and grew normally.

4. Discussion

Dynamic detection of microorganisms is a well-known diagnostic technique that facilitates numerous biomedical applications. Many high-tech approaches, by taking advantage of high-power miniaturized LED illumination and low noise ratio, fast and portable imaging based on CMOS, and big data processing methods, open new opportunities in the develop-

ment of point-of-care diagnostic devices for a timely response to diseases. Plasmonic NPs with tunable physicochemical properties promise to deliver far more accurate and rapid diagnostics at a personalized level. Moreover, their unique optical properties can work as individual nano-sensors, in which analytical results are obtained by real-time registration of the spectral characteristics of plasmonic properties interacting with thin biofilms. The use of plasmonic NPs in a “yes/no” response, *i.e.*, as immunoplasmonic markers with multiplex and quantitative detection, facilitates the assembly of portable point-of-care devices due to their simple detection principles and analyses. Simplified representative diagrams of the biosensing devices, consisting of a disposable cartridge, are being developed for analyzing a single drop of small volume (Fig. 6a) and continuous detection of bacteria samples (Fig. 6b).⁴⁴ In both proposed systems, the attachment and dynamic detection, *e.g.*, of selectively conjugated plasmonic NPs on *E. coli*, allow rapid and accurate identification of the target bacteria in biofluids. These devices, equipped with high-speed optical, electro-optical focusing and multi-camera systems, can be assembled with an adjustable microfluidic cell to reduce the nonspecific attachment of bacteria. The dynamic detection of pathogens can be performed by using side-illuminated darkfield imaging, where the magnification of the optical setup depends on the required field of view and sample volume. The advantage of the proposed apparatus lies in the excellent portability potential and the significantly lower cost of industrial realization.

The protocol for utilization and calibrating a biosensor device for point-of-care or individual application will depend on the field of use (health care, environment, water quality), the required operational simplicity or accuracy (Yes/No sensor or precise concentration detection) or multiplex capability to differentiate the mix of bacteria. One of the most important parameters, which should be optimal for each type of application, is the concentration of plasmonic biomarkers. From a technical point of view, the maximum concentration of NPs that can be monitored simultaneously will depend on the size and number of pixels of the camera, the field of view of the

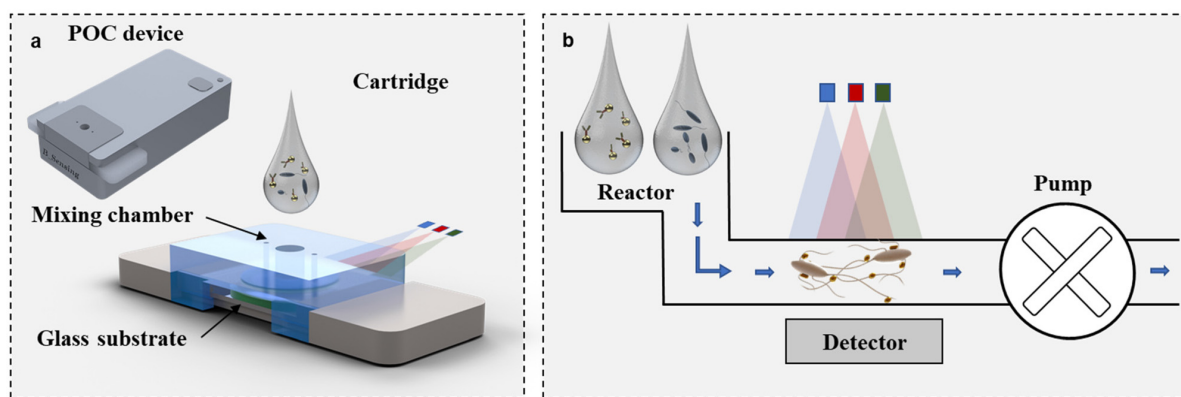


Fig. 6 (a) Schematic representation of a portable optical device with a disposable cartridge for personalized use. (b) Bacteria detection approach for large volume sample using continuous flow.

image, and the volume of the sample. If the detection time is not critical in the micro-volume, the method allows the tracking of even individual NP for the single molecule resolution.⁴⁵ This is why we believe that our proposed method can improve biosensor performance, especially for low bacterial concentrations, compared to existing biosensor methods (*e.g.*, surface plasmon resonance).

5. Conclusions

The growing need for reliable and portable personalized diagnostics is pushing researchers and engineers to explore new approaches and apply the latest technologies. Among various other approaches, employing immunoplasmonic markers as the basis for such diagnostics have great potential since plasmonic NPs can serve as a multiplex and selective bioprobes, as well as effective optical amplifiers that do not require additional efforts for individual NP visualization and detection. We foresee great potential for implementation of the proposed plasmonic-based technology in several fields, taking advantage of the portability that our device offers and the high contrast associated with the plasmonic nanomaterials. Our method also provides flexibility in terms of the volume that can be analyzed with the two different approaches presented in this paper. Dynamic detection removes the ambiguity of conventional static 2D detection and differentiates the bacteria colocalization or aggregation of plasmonic nanoprobe.

The first approach is the detection platform, where the identification of pathogens can be done in small sample volumes (microliters) where the focusing element can be chosen regarding the desired resolution in the field of view. With the second approach, we provide a microscopy platform based on a side-illumination device that can be easily adapted to different needs and be used with large-volume samples (millilitres) having a large field of view without compromising the contrast for optimal detection of the plasmonic markers. With the proposed devices, we are paving the way for the development of a portable technology that has the potential for *in situ* bacterial detection. Moreover, future work regarding disposable cartridges ought to open the possibility of implementing this technology not only in research laboratories but also in hospitals or mobile clinics with limited infrastructure. So far, we have shown that rapid detection of microorganisms can be achieved with a research-degree device that is cost- and time-effective, removing the need for bacteria culturing.

Conflicts of interest

There are no conflicts to declare.

Acknowledgements

The authors acknowledge the support of the Natural Sciences and Engineering Research Council of Canada (NSERC), and

thank Cécile Darvriot for her valuable help in hyperspectral imaging and imaging treatment, as well as Scott G. Harroun for the constructive comments and recommendations.

References

- 1 World Health Organization. *E. coli*, <https://www.who.int/news-room/fact-sheets/detail/e-coli>, (accessed January 19, 2022).
- 2 A. H. Villamagna, S. J. Gore, J. S. Lewis and J. S. Doggett, *Front. Med.*, 2020, 998.
- 3 B. Aslam, W. Wang, M. I. Arshad, M. Khurshid, S. Muzammil, M. H. Rasool, M. A. Nisar, R. F. Alvi, M. A. Aslam, M. U. Qamar, M. K. F. Salamat and Z. Baloch, *Infect. Drug Resist.*, 2018, **11**, 1645–1658.
- 4 S. Hathroubi, M. A. Mekni, P. Domenico, D. Nguyen and M. Jacques, *Microb. Drug Resist.*, 2017, **23**, 147–156.
- 5 C. Manyi-Loh, S. Mamphweli, E. Meyer and A. Okoh, *Molecules*, 2018, **23**, 795.
- 6 M. J. Martin, S. E. Thottathil and T. B. Newman, *Journal*, 2015, **105**, 2409–2410.
- 7 R. M. Meganck and R. S. Baric, *Nat. Med.*, 2021, **27**, 401–410.
- 8 B. Foxman, *Nat. Rev. Urol.*, 2010, **7**, 653–660.
- 9 L. Poirel, J.-Y. Madec, A. Lupo, A.-K. Schink, N. Kieffer, P. Nordmann and S. Schwarz, *Microbiol. Spectrum*, 2018, **6**(4), 14.
- 10 C. L. Ventola, *Pharm. Ther.*, 2015, **40**, 277.
- 11 S. R. Jadhav, R. M. Shah, A. V. Karpe, P. D. Morrison, K. Kouremenos, D. J. Beale and E. A. Palombo, *Front. Microbiol.*, 2018, **9**, 3132.
- 12 S. Notermans and K. Wernars, *Int. J. Food Microbiol.*, 1991, **12**, 91–102.
- 13 F. Bloos, S. Sachse, A. Kortgen, M. W. Pletz, M. Lehmann, E. Straube, N. C. Riedemann, K. Reinhart and M. Bauer, *PLoS One*, 2012, **7**(9), 46003.
- 14 E. Zand, A. Froehling, C. Schoenher, M. Zunabovic-Pichler, O. Schlueter and H. Jaeger, *Foods*, 2021, **10**, 3112.
- 15 F. Le Guern, V. Mussard, A. Gaucher, M. Rottman and D. Prim, *Int. J. Mol. Sci.*, 2020, **21**, 9217.
- 16 C.-S. Ho, N. Jean, C. A. Hogan, L. Blackmon, S. S. Jeffrey, M. Holodniy, N. Banaei, A. A. Saleh, S. Ermon and J. Dionne, *Nat. Commun.*, 2019, **10**, 1–8.
- 17 Q. Wei, G. Acuna, S. Kim, C. Vietz, D. Tseng, J. Chae, D. Shir, W. Luo, P. Tinnefeld and A. Ozcan, *Sci. Rep.*, 2017, **7**, 1–10.
- 18 E. Mohamadi, M. Moghaddasi, A. Farahbakhsh and A. Kazemi, *J. Photochem. Photobiol., B*, 2017, **174**, 291–297.
- 19 G. Gao, Y.-W. Jiang, W. Sun and F.-G. Wu, *Chin. Chem. Lett.*, 2018, **29**, 1475–1485.
- 20 M. A. Hahn, J. S. Tabb and T. D. Krauss, *Anal. Chem.*, 2005, **77**, 4861–4869.
- 21 A. Belushkin, F. Yesilkoy and H. Altug, *ACS Nano*, 2018, **12**, 4453–4461.

- 22 P. Marcoux-Valiquette, C. Darvot, L. Wang, A. A. Grosset, M. Hasanzadeh Kafshgari, M. Birela, S. Patskovsky, D. Trudel and M. Meunier, *Cancers*, 2021, **13**, 3509.
- 23 A. Nsamela Matombi, M. Hasanzadeh Kafshgari, L. Wang, S. Patskovsky, D. Trudel and M. Meunier, *ACS Appl. Nano Mater.*, 2020, **3**, 4171–4177.
- 24 Y.-C. Ou, J. A. Webb, C. M. O'Brien, I. J. Pence, E. C. Lin, E. P. Paul, D. Cole, S.-H. Ou, M. Lapierre-Landry, R. C. DeLapp, E. S. Lippmann, A. Mahadevan-Jansen and R. Bardhan, *Nanoscale*, 2018, **10**, 13092–13105.
- 25 M. Ouyang and D. Di Carlo, *Biosens. Bioelectron.*, 2019, **132**, 162–170.
- 26 M. Soler, C. S. Huertas and L. M. Lechuga, *Expert Rev. Mol. Diagn.*, 2019, **19**, 71–81.
- 27 T. Wagner, H. G. Lipinski and M. Wiemann, *J. Nanopart. Res.*, 2014, **16**, 2419.
- 28 A. S. Dileseigres, Y. Prado and O. Pluchery, *Nanomaterials*, 2022, **12**, 292.
- 29 S. Patskovsky, E. Bergeron, D. Rioux and M. Meunier, *J. Biophotonics*, 2015, **8**, 401–407.
- 30 S. Patskovsky, E. Bergeron, D. Rioux, M. Simard and M. Meunier, *Analyst*, 2014, **139**, 5247–5253.
- 31 S. Patskovsky and M. Meunier, *J. Biomed. Opt.*, 2015, **20**, 097001.
- 32 D. B. Peckys, G. M. Veith, D. C. Joy and N. De Jonge, *PLoS One*, 2009, **4**(12), 8214.
- 33 K. Taute, S. Gude, S. Tans and T. Shimizu, *Nat. Commun.*, 2015, **6**, 1–9.
- 34 W. B. Piekos, *Microsc. Res. Tech.*, 1999, **46**, 334–337.
- 35 K. Thorn, *Mol. Biol. Cell*, 2016, **27**, 219–222.
- 36 M. Qi, C. Darvot, S. Patskovsky and M. Meunier, *Analyst*, 2019, **144**, 1303–1308.
- 37 L. Wang, C. Darvot, J. Zapata-Farfan, S. Patskovsky, D. Trudel and M. Meunier, *J. Biophotonics*, 2019, **12**(11), 166.
- 38 S. K. Brar and M. Verma, *TrAC, Trends Anal. Chem.*, 2011, **30**, 4–17.
- 39 A. M. Loske, E. M. Tello, S. Vargas and R. Rodriguez, *Arch. Microbiol.*, 2014, **196**, 557–563.
- 40 S. Vargas, B. E. Millan-Chiu, S. M. Arvizu-Medrano, A. M. Loske and R. Rodriguez, *J. Microbiol. Methods*, 2017, **137**, 34–39.
- 41 J. Stetefeld, S. A. McKenna and T. R. Patel, *Biophys. Rev.*, 2016, **8**, 409–427.
- 42 K. N. Clayton, J. W. Salameh, S. T. Wereley and T. L. Kinzer-Ursem, *Biomicrofluidics*, 2016, **10**, 054107.
- 43 A. A. Nastulyavichus, S. I. Kudryashov, E. R. Tolordava, L. F. Khaertdinova, Y. K. Yushina, T. N. Borodina, S. A. Gonchukov and A. A. Ionin, *Laser Phys. Lett.*, 2021, **18**(8), 6002.
- 44 N. Pazos-Perez, E. Pazos, C. Catala, B. Mir-Simon, S. Gomez-de Pedro, J. Sagales, C. Villanueva, J. Vila, A. Soriano, F. J. G. de Abajo and R. A. Alvarez-Puebla, *Sci. Rep.*, 2016, **6**(1), 1–10.
- 45 A. D. Buskermolen, Y. T. Lin, L. van Smeden, R. B. van Haaften, J. Yan, K. Sergelen, A. M. de Jong and M. W. J. Prins, *Nat. Commun.*, 2022, **13**, 6052.